University of Alberta

The Role of Turbulence in Pulsation Induced Orifice Plate Flow Metering Error

by

Dallas Dwayne Chapple

A thesis submitted to the Faculty of Graduate Studies and Research in partial fulfillment of the requirements for the degree of Master of Science.

Department of Mechanical Engineering

Edmonton, Alberta
Spring 1998

National Library of Canada

Acquisitions and Bibliographic Services

395 Wellington Street
Ottawa ON K1A 0N4
Canada

Bibliothèque nationale du Canada

Acquisitions et services bibliographiques

395, rue Wellington
Ottawa ON K1A 0N4
Canada

Your file Votre référence

Our file Notre référence

The author has granted a non-exclusive licence allowing the National Library of Canada to reproduce, loan, distribute or sell copies of this thesis in microform, paper or electronic formats.

L'auteur a accordé une licence non exclusive permettant à la Bibliothèque nationale du Canada de reproduire, prêter, distribuer ou vendre des copies de cette thèse sous la forme de microfiche/film, de reproduction sur papier ou sur format électronique.

The author retains ownership of the copyright in this thesis. Neither the thesis nor substantial extracts from it may be printed or otherwise reproduced without the author's permission.

L'auteur conserve la propriété du droit d'auteur qui protège cette thèse. Ni la thèse ni des extraits substantiels de celle-ci ne doivent être imprimés ou autrement reproduits sans son autorisation.

0-612-28925-7

Canada

University of Alberta

Faculty of Graduate Studies and Research

The undersigned certify that they have read, and recommend to the Faculty of Graduate Studies and Research for acceptance, a thesis entitled The Role of Turbulence in Pulsation Induced Orifice Plate Flow Metering Error submitted by Dallas Dwayne Chapple in partial fulfillment of the requirements for the degree of Master of Science .

Dr. L.W. Sigurdson (Supervisor)

Dr. S.M. Kresta

Dr. W.H. Finlay

April 16, 1998

ABSTRACT

The objective of this project was to use flow visualization and turbulent large-scale vortex structure theory to develop a more complete understanding of the flow physics involved in pulsation-induced error of orifice plate flow-rate meters. A test rig was designed and built to include fully turbulent pipe flow, smoke wire flow visualization, independent pulsation level control, and computer control and data acquisition. An over-prediction error of as much as 40% occurs when the highest levels of velocity pulsation are present at the orifice plate. This happens when the non-dimensional frequency of pulsation corresponds to the jet or shedding instabilities previously found in other flows. Analysis of photographs suggests that the error is caused by a modification of the vortices just downstream of the orifice plate. This narrows the vena contracta, reduces the downstream pressure and therefore increases the measured pressure drop for the same flow rate.

ACKNOWLEDGEMENTS

Considerable thanks to Dr. Lorenz Sigurdson who, as my supervisor, put up with me for almost three years. I am grateful for all your assistance both in completing my degree and in helping me develop better work habits.

I would also like to thank all the faculty and staff of the Mechanical Engineering Department; Mr. Blaine Sawchuk, Dr. Kamal Botros, and Mr. Ron Kowch from NOVA Gas Transmission Ltd.; and Andrew, James, Bill, Lance, and Ashok.

Special thanks to Andrew Coward, Bernie Faulkner, Ian Buttar, Mark Ackerman, Terry Nord, and Al Muir who not only helped me time and time again in designing and assembling things, but also went out of your way to help out when problems arose.

This work was funded primarily by NOVA Gas Transmission Ltd. with some support from the Natural Sciences and Engineering Research Council grant OGP 0041747.

CONTENTS

1 Introduction 1
- 1.1 Motivation . . . 1
  - 1.1.1 Background . . . 1
  - 1.1.2 The Problem . . . 3
  - 1.1.3 Summary and Chapter Outline . . . 5
- 1.2 Various Expected Instability Frequency Regimes . . . 6
  - 1.2.1 Coherent Large-Scale Structures in Turbulence . . . 6
  - 1.2.2 Kelvin-Helmholtz Instability (Figure 1.2a) . . . 8
  - 1.2.3 Jet Instability (Figure 1.2b) . . . 10
  - 1.2.4 Shedding Instability of a Reattaching Flow (Figure 1.2c) 11
  - 1.2.5 Application to Orifice Plate Flows . . . 11
- 1.3 Objectives . . . 14
- 1.4 Thesis Outline . . . 15

2 Experimental Setup and Apparatus 17
- 2.1 Introduction . . . 17
- 2.2 Wind Tunnel Tests . . . 17
  - 2.2.1 Smoke Wire . . . 18
  - 2.2.2 Other Equipment . . . 21
- 2.3 Main Test Rig . . . 23
  - 2.3.1 Piping . . . 24
  - 2.3.2 Flow Rate (Q) Measurement Section . . . 32
  - 2.3.3 Test Section . . . 36
  - 2.3.4 Pulsation . . . 40
  - 2.3.5 Air Flow . . . 43
  - 2.3.6 Computer . . . 45
  - 2.3.7 Transducers . . . 49
- 2.4 Experimental Procedures . . . 52

2.5 Summary of Experimental Design 54

3 Results and Discussion 57
3.1 Introduction 57
3.2 Square Wind Tunnel Results 58
3.3 Introduction to Round Pipe Data 66
3.4 A Proposed Mechanism for Pulsation Induced Meter Error . . 67
3.4.1 Vortex Modification 71
3.4.2 Narrowing of Vena Contracta and Reattachment Length 75
3.4.3 Increased Pressure Drop 78
3.5 Reduction of the Discharge Coefficient (C_D) 81
3.5.1 Pulsation Levels 81
3.5.2 Different Instabilities 86
3.5.3 Reynolds Number 96
3.5.4 Flow Rate(Q) and Velocity Profiles 98
3.5.5 Effect of Acoustic Node Position 103
3.5.6 Comparison With $\beta = 0.65$ 104

4 Conclusions and Future Work 106
4.1 Conclusions 106
4.2 Future Work 111

Bibliography 113

A Smoke Wire Development 117

B LabVIEW Programs 121
B.1 Description of *main6-1.vi* 122
B.2 Description of *Data to spreadsheet.vi* 125
B.3 Description of *nnp prep.vi* 127
B.4 Description of *nnp2.vi* 129
B.5 Description of *pipematrix.vi* 130
B.6 Description of *Measure Q (equal areas)(9-13).vi* 131
B.7 Description of *Concentric Cylinder Q.vi* 133
B.8 Description of *traverse return to home.vi* 135
B.9 Description of *traverse control with no encoder.vi* 137

C Relevance to Orifice Plate Meter Design 139
C.1 Determining Dangerous Frequency Regimes 139
C.2 Speculation on Regimes for Other Beta Ratios and a Possible Correction Methodology 142

D Data Sample 145
D.1 970611 146
D.2 970620 147
D.3 970624 174
D.4 970703 175

List of Tables

1.1 Strouhal Variables 12

3.1 Experiment Settings 67
3.2 Pulsation Level Comparison 103

D.1 970611 Run 146
D.2 970620 Run 147
D.3 970624 Run 174
D.4 970703 Run 175

List of Figures

1.1 Exploded Schematic View of an Orifice Plate Flow Meter . . . 2
1.2 Three Turbulent Instabilities 9
1.3 Two Views of Orifice Plate Flow 13

2.1 Smoke Wire Schematic 20
2.2 Main Rig Schematic View 24
2.3 Spread Sheet: Operating Point 26
2.4 Spread Sheet: Maximum Velocity 28
2.5 Q-Section Schematic 34
2.6 Test Section 37
2.7 Orifice Plate Assembly 39
2.8 Different Pulsator Configurations 42
2.9 Configuration Pop-up Menu 47
2.10 Data Page for 970611R3N06 55

3.1 Velocity Measurement $f_p = 60$ Hz 60
3.2 Orifice Flow, No Pulsation 62
3.3 Orifice Flow, Pulsation at 15 Hz 63
3.4 Photograph: No Pulsation 68
3.5 Photograph: High Frequency Pulsation, $St_{sh} = 1.5$, $St_j = 2.1$. 69
3.6 Photograph: Low Frequency Pulsation, $St_{sh} = 0.33$, $St_j = 0.42$ 70
3.7 Photograph: No Pulsation 73
3.8 Photograph: Low Frequency Pulsation, $St_{sh} = 0.16$, $St_j = 0.32$ 74
3.9 Graph Comparing Pressure Drop With and Without Flow . . 80
3.10 Complete Set of ΔC_D vs Non-dimensional Pulsation Frequency (St_j or St_{sh}) at Different Pulsation Levels 82
3.11 Maximum Effect on C_D vs Pulsation Level 83
3.12 Partial Set of ΔC_D vs Non-dimensional Pulsation Frequency (St_j or St_{sh}) at Different Pulsation Levels 84

3.13 Graph Showing Effect on C_D Along With Two Measures of the Pulsation Level 85
3.14 Large Effect Around Expected Jet and Shedding Frequency . . 88
3.15 HWT Turbulence Intensity Versus St_{sh} and St_j for $\frac{u'}{U_\infty} = 9\%$. 89
3.16 Reversed Flow 90
3.17 Intermediate Frequency Effect 92
3.18 Initial Kelvin-Helmholtz Vortex 94
3.19 Typical Corner Separation Bubble 95
3.20 Pipe Turbulence 97
3.21 Typical Velocity Profile 101
3.22 Symmetric Velocity Profile 102
3.23 Photograph With $\beta = 0.65$ 105

A.1 Smoke Wire Reservoir Drawing 120

B.1 Front Panel of *main6-1.vi* 124
B.2 Front Panel of *Data to spreadsheet.vi* 126
B.3 Front Panel of *nnp prep.vi* 128
B.4 Front Panel of *nnp2.vi* 129
B.5 Front Panel of *pipematrix.vi* 130
B.6 Front Panel of *Measure Q (equal areas)(9-13).vi* 132
B.7 Front Panel of *Concentric Cylinder Q.vi* 134
B.8 Front Panel of *traverse return to home.vi* 136
B.9 Front Panel of *traverse control with no encoder.vi* 138

D.1 20R1N07 148
D.2 20R1N15 150
D.3 20R1N21 152
D.4 20R1N22 154
D.5 20R1N27 156
D.6 20R1N32 158
D.7 20R2N04 160
D.8 20R2N08 162
D.9 20R2N16 164
D.10 20R2N19 166
D.11 20R2N25 168
D.12 20R2N27 170
D.13 20R2N35 172

NOMENCLATURE

C_D	discharge coefficient
C_{D_o}	C_D found in the usual way using the AGA Standard
ΔC_D	$\left(\frac{C_{D_{\text{with pulsation}}} - C_{D_{\text{no pulsation}}}}{C_{D_{\text{no pulsation}}}}\right) \times 100\%$
d	orifice diameter, mm
D	pipe inside diameter, mm
D_v	diameter of vena contracta, mm
f	frequency, hertz
H	step height
H_v	height of vena contracta, mm
HW	hot wire
HWQ	hot wire in the Q section
HWT	hot wire in the test section
KH	Kelvin-Helmholtz
NNP	NOVA Node Program used to calculate the acoustic pressure and velocity distribution in the pipe

OP ..... orifice plate

Q ..... volume flow rate, m^3/s

Re ..... Reynolds number = $\frac{UD}{\nu}$

St ..... Strouhal number = $\frac{fD}{U}$

U ..... velocity, m/s

u' ..... velocity pulsation amplitude at the orifice plate measured using the NNP, m/s

U_{pipe} ..... mean velocity in the pipe, m/s

U_v ..... velocity in the vena contracta, m/s

β ..... beta ratio = $\frac{d}{D}$

λ ..... wavelength, mm

ν ..... kinematic viscosity, $length^2/time$

θ ..... momentum thickness, length

subscripts:

c ..... convection

i ..... initial

j ..... jet

p ..... pulsator

pipe ..... pipe

sh ..... shedding

smoke ..... smoke

v ..... vena contracta

CHAPTER 1

INTRODUCTION

1.1 Motivation

1.1.1 Background

The orifice plate flow-meter is used extensively in the natural gas industry and many others. This device measures the flow indirectly by causing a pressure drop and then measuring that pressure. This is done by adding an obstruction, an orifice plate, into the flow, and is therefore called an obstruction flowmeter. Many obstruction flow meters exist but the orifice plate is by far the most commonly used due to it's simplicity and low cost. Figure 1.1 gives a schematic view of an orifice plate flow meter (exploded view). The pipes are held together (with the orifice plate inbetween) using a flange, and pressure taps are used, generally in the flange, to measure the pressure. Through many experiments over many years it has been found that

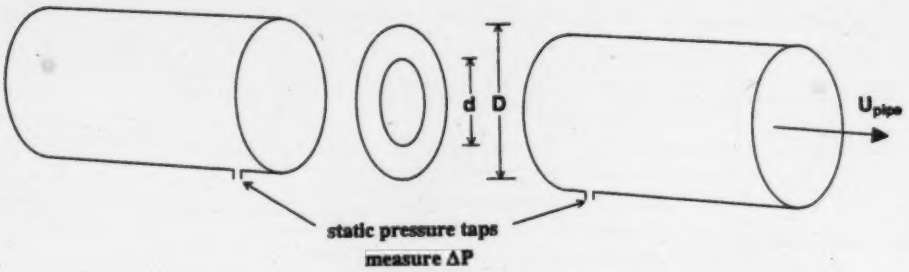

Figure 1.1: Exploded Schematic View of an Orifice Plate Flow Meter

the flow rate can be calculated from the measured pressure using equation 1.1.

$$Q = C_D \beta^2 \sqrt{\frac{2\Delta P}{\rho}} A_{pipe} = U_{pipe} A_{pipe} \tag{1.1}$$

where Q is the flow rate, C_D is the discharge coefficient, $\beta = \frac{d}{D}$, called the beta ratio, ρ is the fluid density, A_{pipe} is the pipe cross-sectional area, and U_{pipe} is the mean velocity in the pipe.

The discharge coefficient is used to take all other effects into consideration and has been carefully measured for a large range of Reynolds numbers and beta ratios. (Both numbers are explained in Section 1.2.) Standards have been developed that provide the appropriate C_D for a given meter setup. These standards were developed for and under steady but turbulent flow conditions.

1.1.2 The Problem

The problem is that a large number of gas metering installations do not have steady flow. Unsteady (pulsating) flow can be caused by reciprocating compressors or turbulence noise caused by flow disturbances like valves, T's, or elbows. Presently, to ensure an accurate reading the pulsation must be removed which is generally a very costly procedure, especially considering there are hundreds of orifice plate metering stations in Alberta alone passing hundreds of millions of cubic meters of gas every day.

An extensive literature search was done at the University of Alberta's libraries which focused on publications related to pulsation, orifice meters and visualization, as well as important authors in the field. Many experimental studies in turbulent flow have been done that look at pulsating flow through orifice plate meters. From this search, only one paper was found that includes visualization of pulsating flow through an orifice plate flow meter (Hebrard et al., 1985). This paper reports on some characteristics of the flow and vortices in the flow, but "the research which is presented in this paper was not especially focused on determining flow measurement errors . . ." (Hebrard et al., 1985). No correlation between the observed vortices and meter error is given or when meter error would occur. This was investigated in this thesis and is reported on in Chapter 3. Other papers measured parameters like pressure levels, velocity profiles, and pulsation levels, among other things. Some of these studies occurred at very low Strouhal numbers and saw little correlation between meter error and frequency (Jungowski et al., 1990;

Mottram, 1992, 1981). Other studies had Strouhal numbers near where the large-scale structures in turbulence are expected to effect the flow (Gajan et al., 1992; Grimson and Hay, 1971; Mottram, 1974). These studies showed increasing error in the flow rate as the Strouhal number increased, but correlating this error to the Strouhal number was not accomplished. This is likely because the pulsation level was characterized by the measurement of pressure pulsations across the orifice plate, and not the velocity fluctuations just downstream of the orifice plate as we did. Therefore the tests at different frequencies would all have different velocity pulsation levels. This happens because the acoustic nodal positions vary with frequency, giving varying levels of effect on the discharge coefficient. This would make it impossible to discover any trend due to frequency.

Some visualization studies have been done for a vortex flow meter (Hebrard et al., 1992), and for different flow types like the flow over a cylinder (Sigurdson, 1995). Both these studies found that pulsation at a particular frequency range had a significant effect on the shedding vortices and the resulting flow behaviour. The same result was expected and has been shown to occur in orifice plates and is discussed in Chapter 3.

Freitas (1995) did a numerical calculation of the flow through an orifice plate with no pulsation. The calculation indicated the presence of large vortical structures but there was no mention of them.

Some numerical studies in pulsating laminar flows found that the Strouhal number is important in predicting the flow behaviour (Shi et al., 1994;

E.H. Jones Jr, 1991). There was, however, no discussion of large-scale vortical structures.

At least one visualization study has been done on flow through an orifice plate flowmeter in turbulent, steady flow (Gajan et al., 1989).

At least one study was done that looked at the effect of turbulence on the orifice plate, but this did not include pulsation, visualization, or look at the large-scale structures, just the averaged turbulence characteristics (Karnik et al., 1994).

The conclusion made in most of the papers is that more study is necessary, as a fundamental knowledge of the physics in pulsating flow through orifice plate flow meters is still lacking. This thesis is part of further study and it develops a relationship between the large-scale structures in turbulence and the resulting meter error. The frequencies at which this occurs is covered as well as a proposed methodology for explaining the role that turbulence has in pulsation induced orifice plate flow metering error.

1.1.3 Summary and Chapter Outline

To summarize the motivation for this study, pulsating flow can cause flow metering error, it is expensive to remove the pulsation, and previous research included very little flow visualization and did not consider seriously the effect of turbulence. Hence, it was our goal to learn more about the fundamental physics of the problem using flow visualization to determine the role that large-scale structures in the turbulence have.

This chapter continues with a short review of relevant concepts from turbulent fluid dynamics research in Section 1.2 including how these concepts were expected to apply to pulsation induced orifice plate flow meter error. The objectives that were met by this project are discussed in Section 1.3. The last section in this chapter, Section 1.4, outlines the layout of the rest of the thesis.

1.2 Various Expected Instability Frequency Regimes

1.2.1 Coherent Large-Scale Structures in Turbulence

Within the last two decades, there has been a revolutionary change in how turbulence is viewed. Previously, turbulence was considered to be entirely random, but now it has been found to contain identifiable large-scale structures. Since this discovery, a tremendous amount of flow visualization has been done to observe large-scale turbulent structures in external flows (one consequence of this was to confirm their existence even at high Reynolds numbers (Roshko, 1976; Brown and Roshko, 1974)).

This section will cover how large-scale structures are expected to influence pulsating flow through orifice plates. Some definitions follow which are needed for this discussion to make sense.

It is useful to group important parameters into non-dimensional groups that can be used to compare flows with different velocities and dimensions. A common non-dimensional number used when discussing orifice plates is

the beta ratio (β), which is $\frac{d}{D}$ where d is the orifice diameter and D is the pipe inside diameter. Two other important non-dimensional numbers are the Reynolds number (Re) and the Strouhal number (St). Re = $\frac{UD}{\nu}$ where U is the velocity, D is the characteristic length scale and ν is the kinematic viscosity. The Reynolds number represents the ratio between dynamic forces and viscous forces. The convention for flow in pipes and through orifice plates is to use the mean pipe velocity and the pipe diameter. St = $\frac{fD}{U}$, where f is the frequency, D is the characteristic length scale and U is the velocity. The Strouhal number is a scaling for periodic flow structures. The presence of large structures in turbulent pipe flow through orifice plates is a relatively new concept, therefore there is no convention for what to use for the velocity or the characteristic length scale. This section will develop three different sets of Strouhal numbers corresponding to three different types of instabilities.

For free shear flows, turbulent structures, at a sufficiently large Reynolds number, exist independently of Reynolds number. They are apparently present no matter how high the Re becomes. The existence and importance of large-scale structures was discovered collectively (Brown and Roshko, 1974; Crow and Champagne, 1971; Winant and Browand, 1974). As they were doing tests on the growth of a turbulent shear layer, Brown and Roshko found that the large-scale turbulent structures exist even when the Reynolds number is increased (Brown and Roshko, 1974). The range of scales increases however, with more smaller scale turbulence appearing as Re increases. This

independence on Re has been further demonstrated in several cases. One demonstrated that the turbulent structure of a water drop penetrating the free surface of a tank of water appears to be remarkably similar to that of an above ground nuclear blast (Sigurdson, 1987, 1991, 1997). The Reynolds numbers in these two cases are many orders of magnitude different.

With the discovery that large-scale structures exist for a large range of Reynolds numbers, much more research has been undertaken to understand the various types of instabilities that can be characterized. The following instabilities have been identified in external flows, and in jets. They are conjectured by us to exist in the flow downstream of an orifice plate, and in Chapter 3, evidence will be provided to show that they or some related forms of them are actually present. These are the

- Kelvin-Helmholtz (shear layer) instability,
- Jet instability, and
- Shedding instability of a reattaching flow

and are sketched in Figure 1.2.

1.2.2 Kelvin-Helmholtz Instability (Figure 1.2a)

This is the instability of the shear layer and thus depends on the thickness of the shear layer, (one measure of which is the momentum thickness). It occurs at the interface between two flows of different velocity, initially separated by a splitter plate which then ends to allow mixing between the two streams. The initial appearance of this instability has been found theoret-

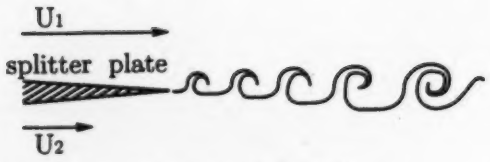

a) Kelvin-Helmholtz Instability

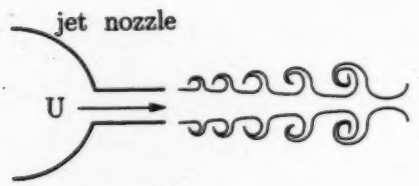

b) Jet Instability

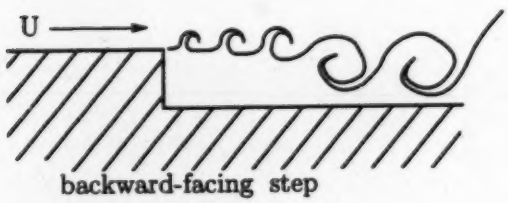

c) Shedding Instability

Figure 1.2: Three Turbulent Instabilities

ically and experimentally to occur at a constant Strouhal number ranging around 0.032 (Michalke, 1964). In this case St = $\frac{f\theta}{U_c}$ where f is the frequency of the instability in Hz, θ is the initial momentum thickness of the shear layer (immediately after separation), and U_c is the average velocity of the two flows. (Michalke's experiment was on the shear layer in a jet, not a splitter plate, and so he uses the jet centerline velocity to scale with (Michalke, 1964). Here we extend the idea by using U_c, the average of the jet velocity and zero.) The initial momentum thickness depends on Re, and so the initial instability is Re dependent. As the structures from the Kelvin- Helmholtz (KH) instability are convected downstream they have a tendency to pair up with the neighboring structures and therefore double in size (Brown and Roshko, 1974). Thus, the instability takes on a range of continuously lowering actual frequencies (St = const). This is the means by which the shear layer grows.

1.2.3 Jet Instability (Figure 1.2b)

The edges of a jet initially contain shear layer structures. As they go downstream, the shear layer structures grow to the point where they begin to interact with the structures from the opposite side of the jet. This causes the jet instability and it occurs at St = $\frac{fD}{U} \doteq 0.3$ where f is the frequency of the instability in Hz, D is the diameter of the jet and U is the jet velocity (Crow and Champagne, 1971). If the Re is high enough, this instability is approximately Re independent.

1.2.4 Shedding Instability of a Reattaching Flow (Figure 1.2c)

For the flow over a backward facing step, (a simple example of a reattaching flow), as the initial shear layer structures grow and pair up, they become large enough that they start to interact with the wall (this is actually an interaction with their mirror image vortices, the fictitious vortices used in potential flow theory to model the presence of a wall).

This interaction causes the shedding instability and occurs around St = 0.08 for a variety of reattaching flows (Sigurdson, 1995). In this case $St = \frac{fH}{U}$, where H is the height of the step, and U is the velocity in the free stream about the reattaching zone. As usual, f is the frequency in Hz of the instability. Above a minimum Re, this instability is approximately Re independent.

1.2.5 Application to Orifice Plate Flows

At the outset of this project, it was expected that the above three turbulent instabilities should be present in orifice plate flows. From the experiments explained below it has been shown that these instabilities do appear to exist in orifice plate flows. Figure 1.3a is a schematic of what they look like.

It is important to note at this point the difference between instantaneous and time-averaged views of the flow. A usual view of the flow through an orifice plate is the time averaged view of the streamlines as shown in Figure 1.3b. If you take a picture of the flow at one instant, individual structures are seen as indicated in Figure 1.3a. Taking a high-speed movie, then slowing the film down would show these structures in each frame convected a

little farther down stream than the previous frame. As the film is sped up they blur together giving the appearance of steady flow. This is similar to marking a shaft with a few dots, then when the shaft is turned at a high rotational velocity, the dots appear as a streak.

Table 1.1 gives the variables used for the St as seen on Figure 1.3.

Table 1.1: Strouhal Variables

Instability type	frequency	velocity	length
Kelvin-Helmholtz	f_{KH}	$U_c = \frac{U_v}{2}$	θ
jet	f_j	U_v	D_v
shedding	f_{sh}	U_v	H_v

For the results reported here, the diameter and step height of the vena contracta, D_v and H_v, were approximated as d and $\frac{(D-d)}{2}$ respectively for simplicity's sake. In actuality, they are different than this since the flow narrows downstream of the orifice plate as shown in Figure 1.3b. The minimum diameter is defined as the vena contracta (White, 1986) and is seen here to vary slightly under the influence of pulsation.

There are at least two other types of instabilities present: the pipe flow turbulence instabilities, and an instability associated with the smaller upstream corner separation bubble. Both structures are clearly seen to exist, but we are at present unsure what role they play in this flow's response to pulsation.

Although all five of these instabilities fall into the category of shear instabilities, it is useful, when possible, to divide the flow into areas where these different instabilities dominate. Each of these instabilities has a characteristic

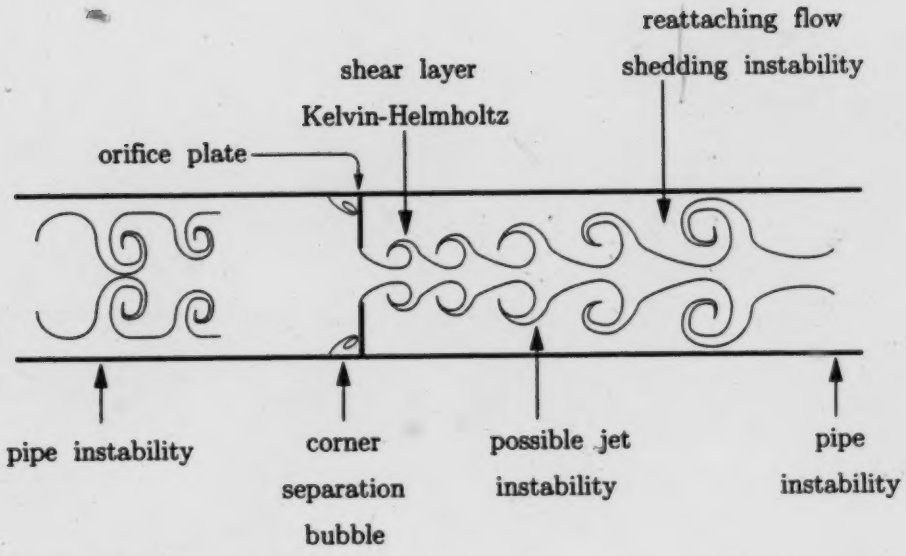

a) Instantaneous View:

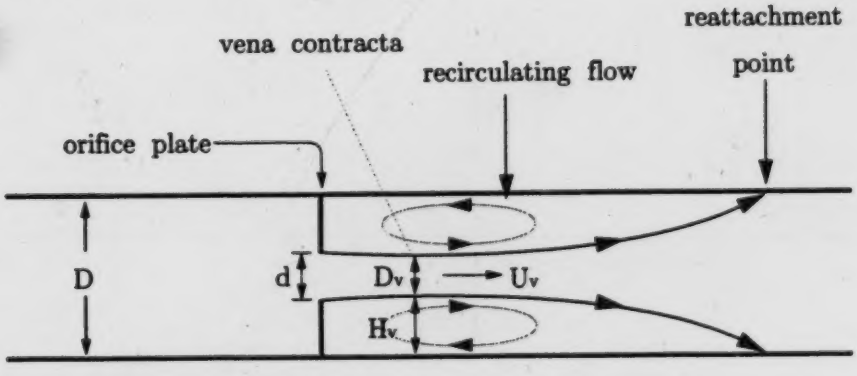

b) Time-Averaged View:

Figure 1.3: Two Views of Orifice Plate Flow

frequency band associated with it where the large-scale structures can amplify pulsation or other disturbances in the flow. Therefore, the frequencies which will be amplified can be estimated in advance, to some extent.

An important consideration for the orifice plate is which of the two instabilities, jet or shedding, would amplify first. This would be expected to depend on the beta ratio. For large beta ratios, the reattachment with the wall would occur before the jet instability, and the jet instability might not appear at all. For the primary beta ratio chosen in the experiments discussed below (β=0.5), both instabilities are present.

1.3 Objectives

Inaccuracies in flow metering can be caused by the unsteady response of orifice plate flow meters to a pulsating flow. The overall objective here was to use flow visualization to develop a more complete understanding of the physics responsible, leading to a correction methodology if that was possible. It was initially intended to perform similar experiments as those done by Jungowski et al. (1990), but to understand the turbulence physics by adding flow visualization. It was found that the frequencies at which these previous experiments were performed were far below what would interact with the turbulence instabilities mentioned above. Therefore the experiments were designed around the frequencies expected to influence the turbulence instabilities, a new frequency range that Jungowski et al. have not previously investigated. It was also necessary to use a lower velocity at which flow

visualization was possible. This ground breaking work looking at the turbulence in the flow is a big step toward eventually developing a correction methodology, but developing this methodology was more than was possible to complete in the duration of this project.

We have developed a theory for the expected frequency regimes where the coherent large-scale structures in the turbulence will be affected, therefore producing metering error. These regimes can then be avoided in metering installations (by removing flow disturbances, adjusting pumping parameters, or changing the pipe diameter or beta ratio) to help ensure accurate metering. When considering some typical natural gas orifice plate installations, it was found that sometimes the pulsation frequency does fall into these regimes. We have also verified some of the theory experimentally and shown with flow visualization and measurements how the large-scale structures are affecting the flow and how much of an error results.

1.4 Thesis Outline

The next chapter in this thesis, Chapter 2, will discuss the experimental apparatus and procedures used to complete the above mentioned objectives. Chapter 3 will then go through all the results obtained and interpret them. This chapter also proposes a mechanism for pulsation induced meter error. Finally, the main conclusions of this study are covered in Chapter 4, where possible future work to further the understanding of pulsation induced orifice plate flow metering error is discussed.

Appendix A provides additional information on the development of the smoke wire reservoir. Appendix B provides a brief description of some of the most important LabVIEW® programs used to run the experiments and process the data. Appendix C provides an explanation of how to apply the results to the design or modification of orifice plate installations. This appendix also includes a proposition for a possible correction methodology. Appendix C is for those who want to apply the results of this thesis without having to read or understand the entire thesis. Finally, Appendix D provides a sample of the data.

Chapter 2

Experimental Setup and Apparatus

2.1 Introduction

This chapter discusses all of the pieces that make up the experimental apparatus, why they were chosen and what they were used for. Section 2.3 discusses the parts that make up the main test rig. A lot of the design for this rig was influenced by what was learned from preliminary tests done in a wind tunnel, and so the setup for these tests is explained in Section 2.2.

2.2 Wind Tunnel Tests

Some preliminary experiments were undertaken using existing equipment at the University of Alberta to determine if the instabilities mentioned in the first chapter are in fact present in orifice plate flows and if they behave in a similar manner (respond to the same frequencies of excitation [pulsation]) as in other types of flows. It was also to gain insights into the design and implementation of more in depth experiments. Some insights we hoped to

gain included: the adaptation of the smoke wire visualization technique to this application to ensure good quality photographs are taken, and some initial evidence as to the influence of pulsation introduced by a loudspeaker.

There are several methods that can be used to visualize turbulent instabilities. These include the smokewire, laser induced fluorescence, the schlieren technique, shadowgraph, hydrogen bubbles, and dye injections. Dr. L.W. Sigurdson has written a chapter in the *Atlas of Visualization* which discusses some of these techniques (Sigurdson, 1997). Visualization techniques requiring a water facility, such as dye injection and laser induced fluorescence were not used. In the present case, acoustic compressibility effects are deemed to be an important part of the problem, and these would not appear if water (an incompressible fluid) was used as the flow medium. The much greater density of water over air would also make it more difficult to produce large levels of pulsation. The schlieren technique and the shadowgraph make visible variations of density in the flow medium. These methods are therefore often used at higher velocities where shock waves and large density gradients are present in the flow. Otherwise, fluids of different densities must be used in the test rig. To best model the conditions present in the transportation of natural gas, the smoke wire visualization technique was used.

2.2.1 Smoke Wire

T.C. Corke et al. developed the smoke wire technigue for flow visualization in a wind tunnel (Corke et al., 1977). This method introduces a sheet of

smoke streaklines into the flow. [*A streakline - as defined by Frank M. White is ". . . the locus of particles which have earlier passed through a prescribed point." A streamline, on the other hand is ". . . a line everywhere tangent to the velocity vector at a given instant." (White, 1986) Streamlines and streaklines coincide in steady flow but NOT in unsteady or pulsating flow.*] The production of these smoke streaklines is accomplished by causing a drop of oil to run down a thin wire that vertically spans the wind tunnel. The oil type and wire diameter are chosen such that the oil beads up into many tiny, approximately evenly spaced, droplets. An electric current is then passed through the wire slowly vaporizing the droplets of oil. This produces a trail of smoke coming from each droplet that is carried along with the flow of air thus producing a complete set of streaklines.

We took the ideas presented by T.C. Corke et al. and, applying them to our own situation, designed and built our own smoke wire. This design work was assisted by Mr. Ashok Mohanty, a third year undergraduate student who is the recipient of a Dean's Research Award. (The Dean's Research Award program is offered to students with a Grade Point Average of greater than 7.0 (out of a possible 9.0). They receive a monetary award from the Dean of Engineering upon completion.) A schematic drawing of the overall system is shown in Figure 2.1. A detailed design drawing and description of the smoke wire reservoir is given in Appendix A. This design, with some modifications to the standoff, was also used in the main experiments. The preliminary experiments were done using a similar setup, the only significant differences

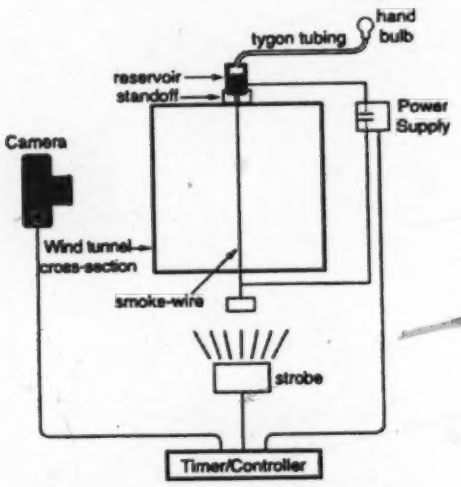

Figure 2.1: Smoke Wire Schematic

are that the reservoir was a syringe held in place by the snugness of the hole for the needle going through the wall of the square wind tunnel. Mr. Bill Peck, a current Ph.D. student, also contributed by building a preliminary version of the reservoir.

The smoke wire was supplied a current using a W5MT3A Metered Variac Auto Transformer (AC power supply). The voltage and current were approximately 10 V and 1 A. Since this was AC power, the current was alternating at 60 Hz, but since resistive heating works whether the current is positive or negative, the heating frequency was 120 Hz. Since more heat produces more smoke, the result of this was a slight oscillation at 120 Hz in the amount of smoke, producing streaklines that appear to be corrugated. This 120 Hz effect was overpowered by high level pulsation from the subwoofer when forcing

at 60 Hz, resulting in a varying density of 60 Hz in the streaklines.

2.2.2 Other Equipment

The rest of the equipment used for the preliminary tests was chosen because it was available in the Mechanical Engineering Department at the University of Alberta. A low speed wind tunnel that has a 2.7 m (9') long test-section with a 305 mm (12") square cross-section was used. The air was sucked through at speeds of about 0.03 m/s to a maximum speed of 3 m/s with the orifice plate installed (max. Re = 66,000). The orifice plate was 172 mm (6.77") in diameter giving the same ratio of orifice area to tunnel test section area (0.25) as a circular pipe with circular orifice with a beta ratio of 0.5. This value of beta ratio was chosen because it is a common size used in the natural gas industry. The wind tunnel speed used was chosen to provide the best picture. At too high a velocity, not only does the smoke disperse quickly due to the turbulence and greater dilution results due to the speed alone, but Von Karman shedding from the wire can become a problem. At too low a velocity, the buoyancy of the heated streaklines overcomes their momentum, and they no longer flow straight downstream but start to rise therefore influencing the flow. The upstream average velocity chosen was measured to be 0.64 m/s in the results section below. There is an influence of buoyancy in the low speed upstream, but not in the higher speed downstream.

Pulsation was generated using a 457 mm (18"), 400 watt subwoofer audio speaker (25 watt max. acoustic output) placed at the upstream end of the

tunnel. It was driven by a 800 watt Crest Audio 2-channel professional power amplifier being given a pure sine wave produced by a sine wave generator. Pictures were taken using a single lens reflex camera with 400 or 1600 ASA black and white print film (TMAX). Illumination was provided by a General Radio Type 1540 Strobolume capable of producing a very short burst of light ($\sim$15μsec.). Black paper was securely fixed to the inside of the test section to reduce the reflection of the strobe off the back and top sides of the clear test section. The effects of this paper would be minimal, at the worst only slightly increasing the thickness of the already very thin boundary layer.

Timing for the pictures was done manually or using an electronic delay timer. The timing was required since it takes time for the smoke to travel downstream once the smoke wire has been activated. Generally the procedure used was; turn on smoke wire, count the delay, open the camera shutter, fire strobe, close shutter, then turn off smoke wire. A sophisticated electronic timer that can activate 10 different instruments to completely automate this has been designed and constructed by Mr. Bernie Faulkner, a technician associated with the project. The cost of this device was divided three ways with other projects which also made use of the device.

Some pressure measurements were taken across the orifice plate, and the velocity was measured using a pitot tube. These were measured using a Setra transducer with 2.5 mm (0.1") water column (wc) range, as well as two Validyne transducers with 6.4 mm (0.25") and 25 mm (1") wc ranges.

2.3 Main Test Rig

Figure 2.2 shows an overall schematic diagram of the main test rig with most of the main aspects grouped in one of the six main sections: piping, Q section, test section, pulsation, air flow, and computer. What we needed to do was reproduce in a controlled way the conditions that an orifice plate meter would experience in the field. Therefore we needed to use a pipe with fully turbulent pipe flow with a Re greater than 4000, as is further explained in Section 2.3.1.

Another important aspect is the pulsation. We wanted to be able to make measurements and take photographs both with and without pulsation. We also wanted to vary the pulsation amplitude independently of the flow velocity to provide more latitude in the type of experiments we could perform. For example, we wanted to be able to use the same pulsation amplitude at two different velocities, with no flow at all, or different amplitudes at the same velocity. Previous experimenters could not do this and it has led to some interesting discoveries. These design requirements meant that the pulsation had to be added separate from the flow.

How this was done is discussed in sections 2.3.4 and 2.3.5. To determine the effect of the pulsation on the discharge coefficient, a measurement of the flow rate with and without pulsation was necessary. This aspect is addressed in Section 2.3.2, Q section. The ability to open up the test section and replace the orifice plate, access to all the measurements taken there, and the flow

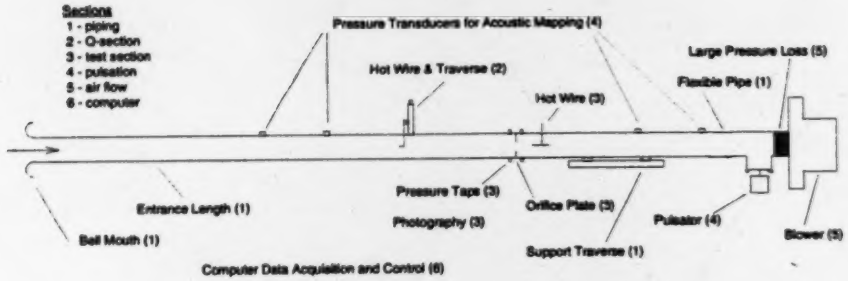

Figure 2.2: Main Rig Schematic View

visualization method used are discussed in Section 2.3.3. Finally, details of each of the transducers used in many of the different areas are discussed in Section 2.3.7. How all of this was made possible using a computer for control and to acquire and analyze the data is discussed in Section 2.3.6.

2.3.1 Piping

The main experiments were conducted in a 146 mm (nominal 6") diameter (ID) round pipe test rig. The operating point this rig was designed for was chosen to be 2.2 m/s. (Experiments were however also performed at velocities as low as approximately 0.9 m/s and as high as 4.8 m/s.) This placed the shedding instability frequency at the center of the expected region of acoustic resonance of the pipe. A number of parameters were taken into consideration while designing this test apparatus. These included, in order of importance:

- enough pipe length to ensure fully developed turbulent pipe flow
- a minimum Reynolds number for validity of the American Gas Association (AGA) equation for the C_D

- appropriate velocity range for smoke wire
- produceable pulsation frequency
- pipe resonance
- minimal optical distortion
- minimal flow disturbance from pulsator
- power requirements to pump the air through

A spreadsheet shown in Figure 2.3 was used to look at most of these concerns at a range of pipe diameters in order to determine the optimum combination of all the variables.

It was decided to use acoustic resonance of the pipe to increase the amplitude of pulsation, so the predicted frequency of the instability needed to be near the resonant frequency of the piping system. This resonant frequency was expected to have an acoustic wavelength somewhere between twice and four times the distance between the entrance and the orifice plate. This is because it was expected that the orifice plate would act as something between a closed end and an open end. It turned out that the resonances were most closely linked to an acoustic wavelength of twice the entire lenth of the pipe. The orifice plate at this beta ratio did not seem to affect the resonance frequency much at all.

From the graph "Pipe Frequencies" of Figure 2.3, it can be seen that the smaller the diameter, the higher the frequency, both for forcing the vortices and acoustic resonance. All three frequencies follow the same curve family, and so there is no obvious choice of diameter from them except that the

Experimental Setup Considerations

Known info:

U_m (m/s) = 2.2	(upstrm pipe vel.)	
Re >= 4000	(UD/v)	
St = 0.08	(f_{shed}*D/U)	
or St = 0.3	(f_{jet}*D/U)	
c (m/s) = 340		
v (m^2/s)= 1.56E-05		
β = 0.5	(d/D)	
X_t = 5		
X_p = 5		
ρ = 0.97	(density of air)	
η = 0.5	(fan efficiency)	
α = 20	(diffuser angle degrees)	
D_f (m) = 0.4572	(fan dia, inches => 18	

Assumptions:

Hv=(D-d)/2	(height of recirc. region)
Dv = d	(vena contract dia.)
L_e=4.4*D*$Re_D^{1/6}$	(entrance length, White) or just use 44D
L_p=D*X_p	(extra length for pulsator and fan)
L_t=D*X_t	(extra length for test section)
L_d=(D_f-D)/(2*TAN(α/2))	(diffuser length)
L=L_e+L_t+L_p	(total length)
c/4L_e < f_{res} < c/2L_e	(resonance of pipe from entrance to plate)
ΔP=k_tρU_m^2/2	(pressure loss)
W=q*ΔP/η	(motor work required)
ΔP_o=ρ(U_o/β)^2C_D^2/2	(orifice pressure loss)

-for sample calculations, see research notes dated 95/6/17

44 44D

loss coefficients

k_t = (see table) friction k_t=fL/D f= 0.03
k_e = 0.03 entrance
k_b = 0.8 branch
C_D = 0.607 orifice discharge coefficient

Variation in C_D from C_D with $Re = 10^{\infty}$

Re	β = 0.5
4E+3	4.7%
1E+4	2.8%
1E+5	0.8%
1E+6	0.3%

-insensitive to variation in diameter

D (in)	D (m)	L_e (m)	L_t (m)	L_p (m)	L_d (m)	L (m)	L (ft)	U_m (m/s)	ρU_m^2/2	Re_D	q (m^3/s)	d (m)	U_t (m/s)	frequencies c/4L (Hz)	f_{shed} (Hz)	c/2L (Hz)	f_{jet} (Hz)	$/(4 ft sec)
1.1	0.03	1.2	0.1	0.1	1.2	2.7	9	2.2	2.347	4.0E+3	0.0014	0.01	8.80	68	99	136	198	****min. D****
4	0.10	4.5	0.5	0.5	1.0	6.5	21	2.2	2.347	1.4E+4	0.0178	0.05	8.80	19	28	38	52	$81.30
6	0.15	6.7	0.8	0.8	0.9	9.1	30	2.2	2.347	2.1E+4	0.0401	0.08	8.80	13	18	25	35	$72.24
8	0.20	8.9	1.0	1.0	0.7	11.7	38	2.2	2.347	2.9E+4	0.0713	0.10	8.80	10	14	19	26	$173.26
10	0.25	11.2	1.3	1.3	0.6	14.3	47	2.2	2.347	3.6E+4	0.1115	0.13	8.80	8	11	15	21	$244.04
12	0.30	13.4	1.5	1.5	0.4	16.9	55	2.2	2.347	4.3E+4	0.1605	0.15	8.80	6	9	13	17	$309.66

ΔP = pressure losses (Pa) 85%

D (in)	D^2/D_f^2	k_d	diffuser	k_t	friction	orifice	recovery	entrance	branch	total ΔP	W (HP)
4	0.06	0.38	0.89	1.92	4.50	102	-51	0.07	1.88	58.3	0.00
6	0.11	0.38	0.89	1.79	4.20	102	-51	0.07	1.88	58.0	0.01
8	0.20	0.32	0.75	1.73	4.06	102	-51	0.07	1.88	57.7	0.01
10	0.31	0.26	0.66	1.69	3.96	102	-51	0.07	1.88	57.5	0.02
12	0.44	0.22	0.52	1.66	3.90	102	-51	0.07	1.88	57.3	0.02

pg 32,33 ******** UPDATED MANUALLY

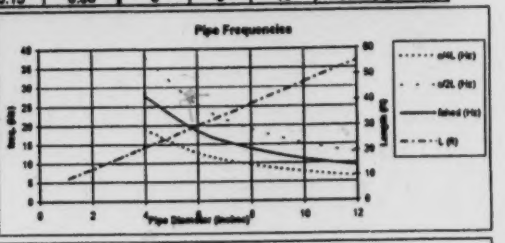

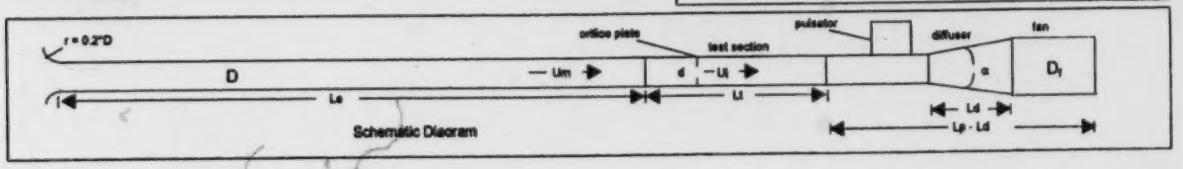

Figure 2.3: Spread Sheet: Operating Point

higher frequencies are easier to produce (from the point of view of maximum pipe length not being a limiting factor), so the smaller diameter the better. The shedding instability frequency was used here since it is the lowest. The other two instabilities occur at higher frequencies and can then easily be forced at harmonics of the resonance frequency.

Another consideration was optical distortion. With optical distortion, the larger the diameter the less the distortion. Also the smaller the wall thickness the better. The top row of numbers on the main table calculates the diameter at which the Re is 4000. This gives the minimum diameter at a given speed. At speeds below 0.6 m/s the minimum diameter was just above 102 mm (4"), but that speed is below the range of speeds appropriate for the smoke wire. The maximum speed for the smoke wire is around 6 m/s, so to include a factor of safety, 7 m/s was taken as the maximum speed, and the power required at that speed was calculated using a very similar spreadsheet shown in Figure 2.4. This was less than 750 watts (1 HP) for all of them, so the power requirement did not restrict which diameters could be used. The power calculations were done taking into consideration the flow losses associated with attaching an axial 457 mm (18") fan.

The main restrictive element in the design was the length. A certain length was needed for the test section, diffuser, the pulsator and fan, and of course the entrance length. The minimum entrance length is $4.4Re^{\frac{1}{6}}$ diameters (White, 1986). This results in the shortest possible pipe, and gives fairly reproducible frequencies, but to get the right flow conditions for the

Experimental Setup Considerations

Known Info:

U_m (m/s) = 7	(upstrm pipe vel.)	
Re >= 4000	(UD/ν)	
St = 0.08	(f_{shed}*Hv/U)	
or St = 0.3	(f_{pul}*Dv/U)	
c (m/s) = 340		
ν (m^2/s)= 1.56E-05		
β = 0.5	(d/D)	
X_t = 5		
X_p = 5		
ρ = 0.97	(density of air)	
η = 0.5	(fan efficiency)	
α = 20	(diffuser angle degrees)	
D_f (m) = 0.4572	(fan dia, inches == 18	

Assumptions:

Hv=(D-d)/2	(height of recirc. region)
Dv = d	(vena contract dia.)
L_e=4.4*D*$Re_D^{1/6}$	(entrance length, White) or just use 44D
L_p=D*X_p	(extra length for pulsator and fan)
L_t=D*X_t	(extra length for test section)
L_d=(D_f-D)/(2*TAN(α/2))	(diffuser length)
L=L_e+L_t+L_p	(total length)
c/4L_e < f_{res} < c/2L_e	(resonance of pipe from entrance to plate)
ΔP=k_fρU_m^2/2	(pressure loss)
W=q*ΔP/η	(motor work required)
$ΔP_o$=ρ(U_o/β)^2/2	(orifice pressure loss)

loss coefficients

k_f = (see table)	friction	k_f=fL/D f= 0.03
k_c = 0.03	entrance	
k_b = 0.8	branch	
C_D = 0.607	orifice discharge coefficient	

44

Variation in C_D from C_D with Re = 10^{∞}

Re	β = 0.5
4E+3	4.7%
1E+4	2.6%
1E+5	0.8%
1E+6	0.3%

-insensitive to variation in diameter

-for sample calculations, see research notes dated 95/8/17

		44D											frequencies				
D (in)	D (m)	L_e (m)	L_t (m)	L_p (m)	L_d (m)	L (m)	L (ft)	U_m (m/s)	ρU_m^2/2	Re_D	q (m^3/s)	d (m)	U_t (m/s)	c/4L (Hz)	f_{shed} (Hz)	c/2L (Hz)	f_{pul} (Hz)	$/(4 ft sec)
0.4	0.01	0.4	0.0	0.0	1.3	1.8	6	7	23.77	4.0E+3	0.0004	0.00	28.00	217	1006	433	1885	*****min. 0*****
4	0.10	4.5	0.5	0.5	1.0	6.5	21	7	23.77	4.6E+4	0.0568	0.06	28.00	19	88	38	165	$61.30
6	0.15	6.7	0.8	0.8	0.9	9.1	30	7	23.77	6.8E+4	0.1277	0.08	28.00	13	59	25	110	$72.24
8	0.20	8.9	1.0	1.0	0.7	11.7	38	7	23.77	9.1E+4	0.2270	0.10	28.00	10	44	19	83	$173.26
10	0.25	11.2	1.3	1.3	0.6	14.3	47	7	23.77	1.1E+5	0.3547	0.13	28.00	8	35	15	66	$244.04
12	0.30	13.4	1.5	1.5	0.4	16.9	55	7	23.77	1.4E+5	0.5108	0.15	28.00	6	29	13	55	$309.68

					ΔP = pressure losses (Pa)						50%	
D (in)	D^2/D_o^2	k_d	diffuser	k_f	friction	orifice	recovery	entrance	branch	total ΔP		W (HP)
4	0.06	0.38	9.03	1.92	46.58	1032	-516	0.71	19.01	590.3		0.09
6	0.11	0.36	8.63	1.79	42.54	1032	-516	0.71	19.01	587.3		0.20
8	0.20	0.32	7.60	1.73	41.03	1032	-516	0.71	19.01	584.4		0.38
10	0.31	0.28	6.65	1.60	40.12	1032	-516	0.71	19.01	582.5		0.55
12	0.44	0.22	5.23	1.56	39.51	1032	-516	0.71	19.01	580.5		0.79

Pg 32.29 ********

UPDATED MANUALLY

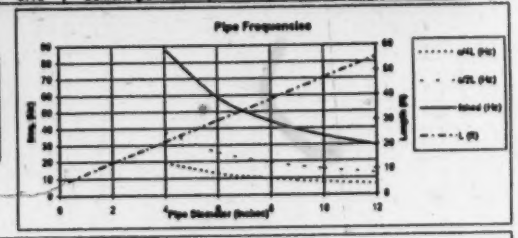

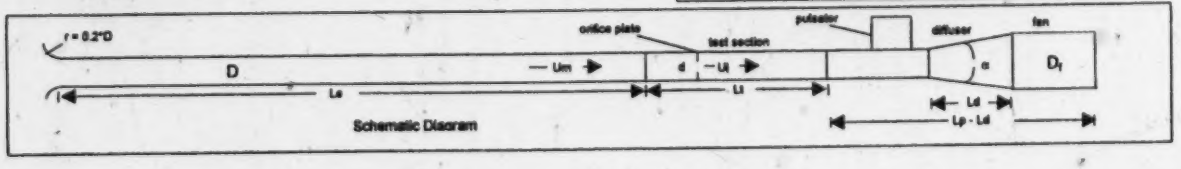

Figure 2.4: Spread Sheet: Maximum Velocity

vortices to be unstable at the resonant frequency of the pipe, the velocity is too close to the maximum velocity for the smoke wire. A longer pipe was chosen (44D), one corresponding to an entrance length with Re = 1,000,000 even though the Re is much lower than that. This lowers the frequencies, and also lowers the velocity necessary to meet the resonant frequency. The pipe was lengthened to lower the velocity required, so to still get a frequency range that is reproducible, the smaller diameter pipes have higher frequencies, therefore a smaller diameter is better. This longer entrance length also allows for higher velocity tests without flow visualization still ensuring a fully developed turbulent flow.

With the above considerations, plus meeting available space requirements, it was necessary to choose a 152 mm (6") diameter pipe which ended up being less than 11 m long. Once an extra section to accomodate measuring the acoustic node position was added, the final length was 13 m. Since the wall thickness of the test section is only 3.2 mm (1/8"), there is still minimal optical distortion.

Other minor considerations that were looked at and are on the spreadsheet are the variation of C_D with Reynolds number. It would be nice to be in the region where C_D is constant with Reynolds number, but that was not possible. There is a small table that shows the percent difference between the C_D at the given Reynolds number, and the C_D at the point where it has leveled out. At the chosen operating point this difference is less than 2%.

All the loss coefficients for the different sections of the pipe are also given.

Some are constant, others rely on the diameter and or the length.

The schematic diagram at the bottom of the spreadsheet is used to give a rough idea of what the rig looked like and what the variables refer to. This is not drawn to scale, and does not include the downstream extension that was required to place the acoustic sensors for their proper functioning.

The rest of this section gives further details on the pipe chosen, and the next sections discuss the details of other aspects of the final test rig that was constructed.

The pipe was chosen with a 152 mm (6") nominal diameter. The thinnest clear pipe available is 3.2 mm (1/8") wall thickness with 152 mm (6") OD cast acrylic tube. Since it only comes in 1.2 or 1.8 m (4 or 6') sections, this would make for a lot of connections if used for the whole piping system. Therefore, the acrylic pipe was used for the test section and a few other portions, and 152 mm (6") schedule 80 PVC (polyvinyl chloride) pipe was used for the rest. This PVC pipe has a the same ID but a larger OD. To accommodate the outside diameter difference of the two pipes, the PVC flanges were used with a PVC pipe that had been bored out so the acrylic could be pressed into it. This allowed the PVC sections to be easily connected to the acrylic sections.

From Figure 6.20 in *Fluid Mechanics* (White, 1986), it was found that the pressure loss of the bellmouth becomes insignificant when the radius of curvature is greater than one fifth the pipe diameter. The bellmouth made has a curvature of one third the pipe diameter. 102 mm (4") diameter

ABS (acrylonitrile butadiene styrene) pipe was cut into segments and glued onto a piece of PVC pipe. This was tested for separation at a range of velocities including the design speed and no separation was observed using a tuft (cotton thread).

The test rig was supported by a variety of means to place it at waist height to make for easy accessability and use. A few spots were supported by wood boxes with a half circle cut out of them and placed on tables, or in one case, a telescopic stand. Two other supports were telescopic stands with sand bags on top to conform to the pipe and hold it down. Another support was the traverse that holds one end of the test section. Some PVC was used to make a rigid connection between a flange and the traverse. This allowed the pipe from the orifice plate to the pulsator to be moved back opening up a space between the two pieces of the test section. This was so we could get inside to adjust things and replace the orifice plate. A piece of flexible dryer duct was used to take up this motion. It would compress when the test section was opened up, and then stretch out again with the test section was closed up. One more support was a block with a "v" notch in it, on top of a telescopic stand. This was designed to hold the pipe in place laterally, yet allow it to traverse back and forth along the pipe direction. The last support was a flange attachement to the blower. No expansion section was used; the pipe was directly mounted to the inlet of the blower.

2.3.2 Flow Rate (Q) Measurement Section

A number of possibilities for determining the reference flow rate were considered. The one chosen was the integration of a velocity profile. This is acceptable according to Fox and McDonald. "To make a flow rate measurement by traverse, the duct cross section is subdivided into segments..." (Fox and McDonald, 1992). In our case, these are annular segments. The velocity in each segment was measured using a hot-wire anemometer. "The volume flow rate for each segment is approximated by the product of the measured velocity and segment area. The flow rate through the entire duct is the sum of these segmental flow rates" (Fox and McDonald, 1992). An additional benefit of this approach is that we could have velocity profile information for each experimental condition. One problem with using a hot-wire anemometer with pulsation present is that it will give erroneous output if there is ever reversed flow. This was a problem and is discussed in Section 3.5.4.

To implement this, a motorized traverse was obtained and attached to a 250 mm section of clear acrylic pipe with flanges on both ends. From now on this section will be referred to as the "Q section", and a schematic diagram of it is given in Figure 2.5. The clear pipe was used so we could see where the probe was as it was working. The clear pipe was also rounder than the PVC, since the manufacturing process of the PVC pipe left a flat spot that runs the full length of the pipe. Therefore an extra 1.2 m (4') long acrylic section was placed upstream of the Q section so that the profile had time to adjust to the slight change in the shape of the cross-section. If

this upstream section was not very carefully aligned, the profile was skewed, or non-symmetric. For a few tests, it was found that the profile was more skewed than normal, and it was found that the probe had bumped into the side of the pipe, affecting the registration point relative to the side of the pipe. It had moved 2 mm, but the calculated effect on the flow rate after correcting the registration was less than 0.4%. A TSI (Thermo-Systems Inc. model 1051) hot-wire (HW) anemometer system was used with probes from Dantec Measurement Technology.

An L shaped probe holder was fashioned out of 4.8 mm (3/16") stainless steel tubing. The probe holder slid through a nylon-sealed swagelock fitting in the top of the pipe and was attached snuggly to the traverse block. This fit was loose enough so that if something went wrong and the probe hit the wall, nothing would break, rather this connection to the traverse would just slip. The computer was used to generate a pulse train that caused the traverse's stepper motor to turn a preset number of steps. This turned the power screw, and moved the traverse block a set distance with an accuracy of ± 0.3 mm. A carefully designed continuity switch had one part connected to the traverse block and the other attached to the framework. When the two came into contact with each other, electrical continuity was made thus communicating to the computer that the probe had reached the registration point. This was used as a repeatable way of starting from the same place every time. A digital caliper was attached on the side and was used as a check of positioning and accuracy. According to the calipers, the registration point was returned to

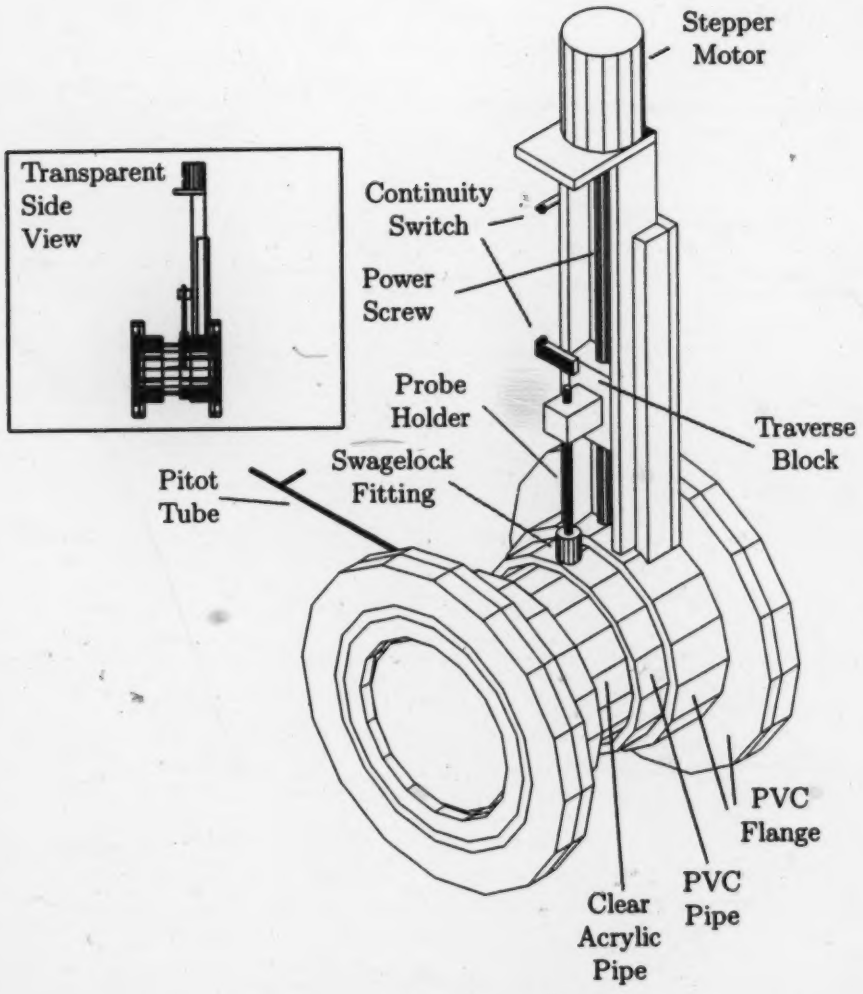

Figure 2.5: Q-Section Schematic

each time to within ±0.02 mm. Original positioning with respect to the wall (the registration point) was done using a cathetometer with an accuracy of ~ ±0.2 mm. Most of these parts are shown in Figure 2.5.

A pitot tube was placed at right angles to the HW (both were 15 mm from the center of the pipe), and slightly further downstream, and was used both as a check and to calibrate the HW. For calibration, the bellmouth section from the entrance of the main rig pipe, was removed and attached just upstream of the Q section. A variable speed blower was connected instead of the normal blower, and the HW could then be calibrated using the pitot tube as this flow was uniform and steady.

To measure the flow rate, the HW probe was moved to its known position from the wall, where a 15 second velocity average was taken. Then it was moved to the twenty-two other positions across the pipe with roughly equal area sections. Once it had taken a measurement at all positions it was moved back to roughly center (58 mm from top) where it monitored the pipe velocity during other phases of the experiment. The velocity profile was integrated numerically to give Q. This entire process took about five minutes.

This control and measurement was done by a LabVIEW® program using the National Instruments DAQ board in a Pentium™ computer. Further explanation of this equipment is given in Section 2.3.7, along with further details of computer control given in Section 2.3.6. This device was designed and constructed with considerable assistance from a third year undergraduate student, Mr. Andrew Coward. In particular, he was responsible for the

physical design and construction of the traverse and the Q section.

Section 2.3.7 covers the specifics and accuracies of the transducers used, and the resulting accuracy of flow rate measurement. Sometimes the pulsation was large enough that for part of the cycle it would reverse the flow. This sometimes caused further error in the flow rate measurement. The accuracy in flow rate ended up not mattering to the calculation of ΔC_D since the flow rate was essentially constant at any given operating velocity. It therefore drops out of the equation. These aspects are further discussed in Section 3.5.4.

2.3.3 Test Section

The test section consists of two (1.2 m (4')) acrylic pipes with one PVC flange at the end of each. They were supported solely near these flanges which were at opposite ends of the test section. This allowed minimal obstruction by unnecessary support structure to photographic line of sight and strobe light illumination, as well as easy access to the outside and inside of the test section. This also allowed for visualization of the flow up to seven diameters upstream and seven diameters downstream of the orifice plate. The two pieces met at the middle of the test section and butted up against each other with the orifice plate in between. Figure 2.6 shows how this fits together. The pressure taps and HWT can also be seen here with the smoke wire 76 mm upstream of the orifice plate. The measured alignment of the two pieces of the test section was within 0.1 to 0.2 degrees of perfectly straight.

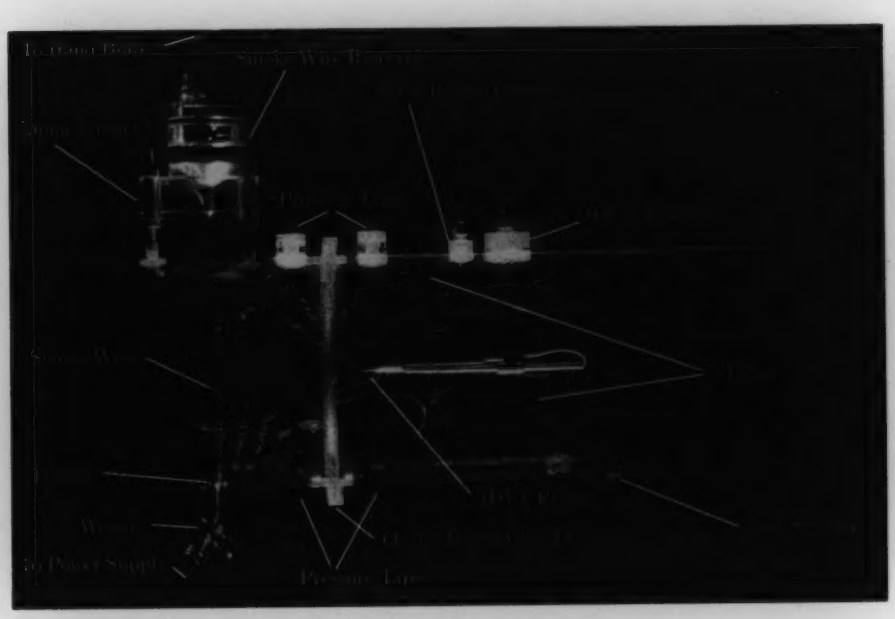

Figure 2.6: Test Section

The faces of these two sections were flush and square to within 0.2 mm. This 0.2 mm gap was sealed by the compression of two 1.6 mm (1/16") O-rings positioned on either side of the orifice plate. The compression of the O-rings was achieved by pushing the two sections together using the traverse mentioned in Section 2.3.1. These O-rings fit snugly between the ends of the test section pieces and the orifice plate assembly which aligned and sealed the pieces together. This orifice plate assembly is shown in Figure 2.7.

2.3.3.1 Smoke Wire

The smoke wire is discussed in the wind tunnel section, Section 2.2. It was used with a more elaborate standoff which was a three legged acrylic cup with suction cups on the feet. It was referred to as the "lunar lander" due to its appearance. Holes were drilled in the test section so that the smoke wire could be put in a number of different locations.

2.3.3.2 Orifice Plate

The orifice plate assembly as seen in Figure 2.7 was made with 1.6 mm (1/16") O-rings in it and two 3.2 mm thick (1/8") alignment rings glued to the orifice plate that sealed and aligned the two pieces of the test section when pushed together using the traverse mentioned in Section 2.3.1. A sharp edge and 45° bevel were used to follow the AGA standards. The only deviation from the standards was that the plate was made out of clear acrylic for visualization purposes.

2.3.3.3 Photography

Photographs of the smoke were taken using a Nikon F2 35 mm camera with a 55 mm Micro Nikkor lens using Kodak TMax 3200 film developed at 3200 ASA. The rest of the equipment is also the same as mentioned in Section 2.2. Some black tape was used in addition to the tape holding the tufts in place (Section 2.3.3.5) to reduce reflections.

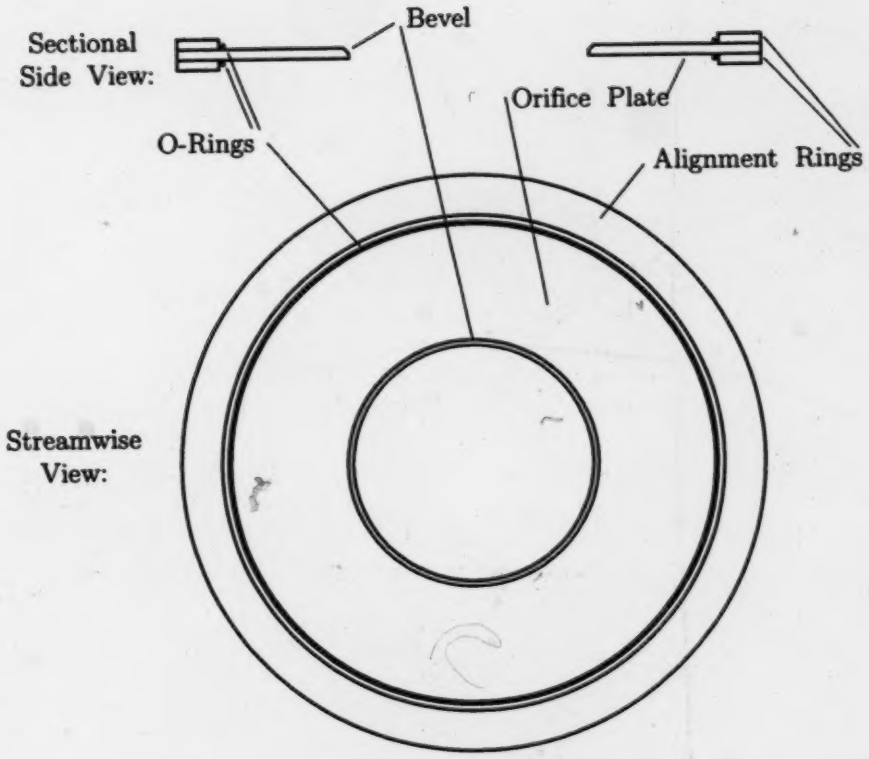

Figure 2.7: Orifice Plate Assembly

2.3.3.4 Timing

Timing for the photography and the following events was controlled using a timing box. It allowed repeatable setting of the time between when the smoke wire was turned on and when the camera was triggered. The camera was set at an exposure of 1/60th of a second and it triggered the strobe after the shutter opened. After this, the smoke wire was turned off. A desk light was turned off and on so that it was dark while the photo was taken, but otherwise there was enough light in the room to keep from running into things. The start of the photograph timing sequence was controlled by the computer.

2.3.3.5 Tufts

Tufts were attached to the inside of the pipe using Scotch Removable Magic™ tape spray painted black. These were made from 100% cotton thread and placed at different distances and lengths for the two different speed tuft strips. These could be watched to determine the reattachment length.

2.3.4 Pulsation

This section is divided into discussing how the pulsation was produced, Section 2.3.4.1, and how it was measured, Section 2.3.4.2.

2.3.4.1 Pulsator

To fully understand the physics it was necessary to visualize and measure things both with the pulsation and without it, so the pulsation needed to be produced separately from the flow. A number of different configurations of speaker mountings and placement as part of adding acoustic pulsation to the flow were considered. These are shown in Figure 2.8. The first was to put a speaker like pulsator at the entrance to the pipe. Secondly this pulsator was placed with a small tolerance inside a T. The final design used was a 2.4 mm (3/32") acrylic plate attached flexibly with a speaker surround to the base of a 152 mm (6") "T" mounted on the pipe. The plate was forced using a B&K Vibration Exciter Type 4809, powered by an in-house built amplifier. The amplifier was given a sine wave from a B&K precision 3030 Sweep/Function Generator from Dynascan Corporation. This T was placed just upstream of the blower so that any flow disturbance caused by the T would not convect past the orifice plate. Forcing was done at pipe resonances to aid in producing higher pulsation levels and achieving a pure tone. The amplitude of the 1st harmonic was generally less than 3% of the fundamental frequency being forced.

Comparison of this test rig to the experiments reported in Jungowski et al. (1990) shows that our frequency range was from a St_j of 0.06 to 8.9, where their frequency range was from a St_j of 0.01 to 0.04. Using St_{sh}, our frequency range was from 0.03 to 2.4, and theirs was from 0.002 to 0.029.

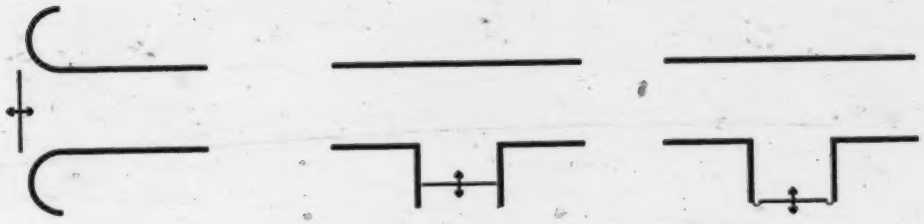

a) At pipe entrance b) Unsealed 'T' c) Sealed 'T'

Figure 2.8: Different Pulsator Configurations

2.3.4.2 NNP (NOVA Node Program)

It was necessary to know the magnitude of the pulsation at the orifice plate, in terms of velocity and pressure, as well as where the nodes were. Four Endevco transducers were offered by Dr. Botros of NRTC (NOVA Research and Technology Center) to be used for this but it was found that the pressure range did not fit our application, and so four Validyne DP15 transducers were found in the Mechanical Engineering department and placed in two pairs. Each transducer was two meters from its partner, with one of the pairs upstream of the orifice plate, and one downstream near the blower as can be seen in Figure 2.2. Each pair of transducers was used to determine the transfer matrix that could then be used to calculate the pressure and velocity distribution from each pair (Kathuriya and Munjal, 1979; Botros et al., 1986). This calculation was done using a modified code in LabVIEW® that was obtained in FORTRAN from Dr. Botros of NRTC which we refer to as the NNP (NOVA Node Program). Dr. Botros also generously ex-

plained how to set it up for our particular rig geometry. A sample of the acoustic velocity and pressure distribution can be seen in the data summary sheet shown in Figure 2.10. Further explanation of the transducers can be found in Section 2.3.7, with details of the computer's involvement given in Section 2.3.6.

2.3.5 Air Flow

To simply have a blower capable of moving the air throught the 146 mm pipe at 2 m/s would have been very simple, but there was a correct concern that the pulsation would change the ΔP across the orifice and therefore the resulting volume flow rate (Q) in the test rig. A significant change in Re would change the frequency at which the vortices would respond, plus the discharge coefficient varies slightly with Re.

Two possible methods to control the flow rate directly affected the selection of a fan and motor. Either feedback control on the blower, or extra pressure losses placed in the system could be used to reduce the effect of the change in ΔP on Q.

The amount that the ΔP would change under pulsating conditions was unknown. Therefore, the design strategy we used was as follows. We used the largest amount of additional pressure losses that could be supported by a centrifugal (low pulsation) blower that was already available in the Mechanical Engineering Department. If it was found through experimentation that there was still a significant change in the Q, the speed of another spe-

cially purchased blower could have been manually or automatically feedback controlled to maintain a constant Q.

It was found that the flow rate changed insignificantly even under maximum pulsation levels. Therefore, the centrifugal Chicago blower that was available in the department was acceptable. This was a turbo type of size 2T-10-28, SWSI, running at 3460 RPM with a 10 HP, 3 phase electric motor.

The speed was controlled by changing the amount of extra pressure loss just upstream of the blower. This was initially done by using multiple pieces of foam, but this was found to have poor repeatability in the resulting speed. A more rigid, repeatable system was developed using porous metal plates. The low velocity plate has sixty-one 2.4 mm (3/32") diameter holes in it and the high velocity plate has twenty 12.7 mm (1/2") holes in it, all but five of which were plugged to get the medium velocity.

The entrance to the blower was about 178 mm, so the 146 mm diameter pipe was bolted directly onto the blower using a flange, with a steel mesh between them to keep large debris from getting into the blower. Inside this flange, a steel collar with an O-ring was glued in place so that the porous plate would press up against this O-ring. This formed a seal so that all the air had to go through the holes in the plate, and none could get around the outside, producing a repeatable speed. The plate was in danger of being significantly shaken when pulsation was present, and so it was held tightly against the o- ring with another steel collar that was thumbscrewed against the inside of the pipe at three points. Each of these pieces was marked so

they could be replaced in the same position to aid in ensuring repeatability of speed.

2.3.6 Computer

The main uses of the computer were to acquire voltage signals from 11 inputs, to control and measure the traverse method of measuring the flow rate, analyzing the pressure data using the NNP to provide the pulsation level at the orifice plate, plus initiate the photographic timing so that the photograph would occur during the acquired data and we would be able to determine at what phase of the pulsation the photo was taken. The computer was also needed to record this data and to output it in useable means.

The computer chosen was a Pentium™ 166 with 64 Meg RAM running Windows® 95, a 2 GIG hard drive, and a 432 mm (17") DAYTEK monitor with a Matrox Millenium Video Card with 2 Meg WRAM. Also installed in the computer was a National Instruments AT-MIO-16E-10 Data Acquisition board. National Instrument's software LabVIEW® was used for control and acquisition.

2.3.6.1 Data Acquisition

There were 11 data lines that voltage data was acquired from. Figure 2.9 shows all the channels, the voltage limits that they had, plus how they were connected (differential or referenced single ended). This figure is from the setup panel for the experiment program and so also covers some of the other

information needed to operate the experiment. These relate to control and will be discussed in Section 2.3.6.3. Before that, the column labelled calibrations needs to be discussed in Section 2.3.6.2. But first, the transducer labels need to be explained. In the figure, P2, P3, P6, P7, are the transducers used for acoustic node mapping, pulsator is a monitor of the sine wave going to the amplifier for the pulsator. HWQ and HWT are the hot-wire anemometers in the Q section and test section respectively.

Pitot is the pitot probe, DPOP1 and DPOP2 are the two measurements of the pressure drop accross the orifice plate, and strobe monitors the signal going to the strobe and produces a spike when the photograph is taken.

2.3.6.2 Conversions

The pressure transducers have a simple conversion from voltage to pressure which was found during calibration using a micropoint manometer as the pressure standard, and this LabVIEW® program measuring the voltage. The magnitudes of the strobe and pulsator signals were not meaningful and so were left as voltage values. The pitot probe transducer had a non-zero zero voltage and so this had to be subtracted from the measured voltage before the conversion could be applied. This value is in the bottom right hand corner of Figure 2.9. The hot-wire anemometer voltages were converted using equation 2.1.

$$E^2 = A + B\sqrt{U} \tag{2.1}$$

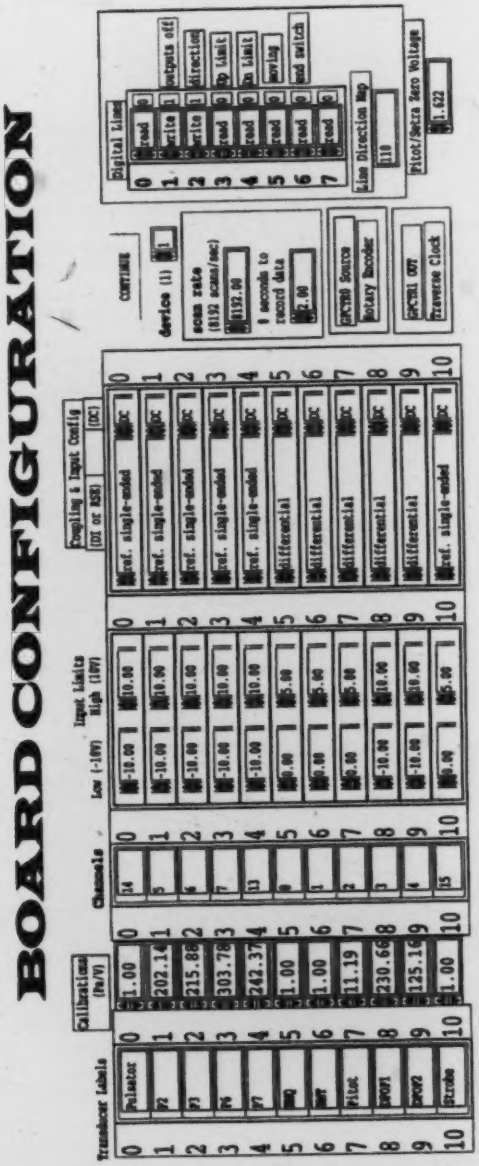

Figure 2.9: Configuration Pop-up Menu

where E is the measured voltage, U is the velocity, and A and B, are calibration coefficients.

2.3.6.3 Control

Two general purpose counters (GPCTR0,1) were used to send a finite length pulse train to the traverse which determined how many steps the motor turned, and how far the traverse moved. Two Digital outputs were used to turn on the motor and to set the direction as seen in Figure 2.9. The remaining channels seen there are inputs and were used to know when the traverse was moving, and if either of the limit safety switches or the end switch that sets zeroing were hit.

Two main programs, including many sub programs were written in LabVIEW®. One of the main programs, titled "main6-1.vi", was used to control the experiment and record the data. This included initializing the hardware, calibrating the HW's, controlling the traverse in the Q section, integrating the velocity profile data to get the flow rate, running the NNP to calculate the acoustic amplitudes in the pipe, as well as recording velocity and pressure data. The other main program, titled "Data to spreadsheat.vi", presented the data in a usable fashion, providing a summary data sheet for each record as well as adding some information to a spreadsheet file for overall run summaries. A brief explanation of some of the programs is included in Appendix B.

2.3.7 Transducers

Nine transducers were used in this experiment:

- 5 Validyne model DP15 pressure transducers,
- 1 Validyne model DP45 pressure transducer,
- 1 Setra model 264 pressure transducer,
- 1 TSI model 1051 2-channel hot-wire anemometer.

The pressure transducers were all calibrated using a Dwyer Microtector® Portable Electronic Point Gage Model No. 1430 as the standard. The accuracy of this device is ±0.06 Pa. From the calibration, the four DP15's used for the NNP (P2, P3, P6, P7) were calculated to have an uncertainty in static pressure of less than ±2 Pa. This was the same for the DP15 (DPOP1) and the DP45 (DPOP2) used to measure the pressure drop across the orifice plate. Using this value, combined with the uncertainty of at worst 3% in the constancy of the flow rate (see Section 3.5.4), the uncertainty in ΔC_D was:

- ±5% at ~1 m/s,
- ±1.5% at ~2 m/s,
- ±0.2% at ~5 m/s.

Most of the measured effects on C_D for all runs were greater than these uncertainties.

These six pressure transducers were compared against each other for dynamic uncertainty since no suitable standard was available. Amplitudes for the four transducers used for the NNP were within 2% of each other, and the phase was generally within 1°. Above 150 Hz, this could get as bad as

10°. The two transducers used to measure the average pressure drop across the orifice plate were also checked for dynamic response, but these were not as good as the other four. Since they were only being used for an average value, this was not considered to be a problem.

The Setra transducer was used with a pitot tube to calibrate the hot wire anemometers. The uncertainty in the velocity measured using the pitot tube and Setra was:

- ±65% at ~1 m/s,
- ±15% at ~2 m/s,
- ±3% at ~5 m/s,

given a Setra uncertainty from calibration of ±0.6 Pa. The range of this transducer was 24 Pa giving the maximum velocity measurable by the pitot tube as 7 m/s. This was not a very good standard to calibrate the hot-wires, but was the best available. It is a very difficult thing to accurately measure velocities lower than 2 m/s. The calibration of the HWT was generally done over a range of velocities from ~1.5 m/s to ~7 m/s and did not deviate from a straight line fit (in appropriate coordinates) at the lower velocities. The pitot tube accuracy was ~1% at 7 m/s. The deviation from the calibrated curve was at worst 6% at the low velocities and ~2% over the rest of the range. The HWT was in the faster flow downstream of the orifice plate where the mean velocity was at lowest 5 m/s. Only under the highest levels of pulsation did the instantaneous flow ever near 1 m/s. Therefore the effective accuracy of the HWT was ~2%. The HWQ on the other hand was calibrated over

a smaller range from ~0.5 m/s to ~1.5 m/s for the 1 m/s runs where the velocity in the pipe was within this range. For the faster runs, this accuracy is much better. The deviation from this calibration was at worst ~8% at the lowest velocity and ~3% over the rest of the range. The accuracy of the pitot tube at 1.5 m/s is ~30%, but the calibration is obviously more accurate than this, and the large calculated uncertainty is extrapolated from the greatest deviation in the Setra calibration giving a worst case value.

The conclusion from these calibrations and subsequent measurements is that the variation in the velocity measurements are generally in the 1 to 5% range. Also, rough verification was obtained from a few photographs where the fluctuations in smoke density could be used to estimate the velocity. These were within about 10% of that measured by both the HWT and the HWQ.

This uncertainty in HW velocity measurement does not adversely affect the end result, since the flow rate was constant, and therefore does not influence the ΔC_D. It does however affect the value of C_D calculated from the measured Q and ΔP. This was as low as 0.51 for the low velocity runs (with no pulsation) where the AGA standard predicted 0.62. For the 5 m/s run, the comparison was much better as expected. The measured C_D was 0.60 compared to 0.61 predicted by the AGA standard.

Since all of these are measured voltages, the data acquisition board's voltage accuracy is important and was found to be very repeatable and within 5 mV of a Fluke 8060A multimeter. The phases and amplitudes measured

by LabVIEW® were within 0.3% of a Fluke multimeter output which was used as a check. A flat- top signal filtering window was used in LabVIEW® with 16384 scans per record.

2.4 Experimental Procedures

The actual rig construction and testing took place in stages. With the blower, the test section and the entrance section with bell-mouth, some preliminary tests were done with the orifice plate in place. Then gradually more of the transducers were added, and tested as they were added. Once the smoke wire was in place some photographs were taken to make sure that things were still working now that we had turbulent pipe flow as opposed to uniform flow in a windtunnel. Pulsation was provided at the entrance of the pipe for these tests. Then the complete rig was put together and testing of the NNP and Q sections took place to ensure their accuracy.

Once all these pieces were working, and the associated control and acquisition software was written, the main experiments were done. These included tests with a 0.5 beta ratio orifice plate at roughly 1, 2, and 5 m/s flow with 3, 2, and 1 levels of pulsation at each velocity respectively.

Multiple photographs were taken at a number of frequencies for each pulsation level. These frequencies were found doing a frequency sweep and for the first 3 runs were calibrated using the NNP at a specific level. Later experiments used the "calibration on the fly" technique. This was a method developed by us that sets the level of pulsation at the desired level using the

NNP in real time.

Some tests with no orifice plate and with no flow were also done so the data can be used to evaluate the effects other than those caused by the flow around the orifice plate. Also, a test was done with a 0.65 beta ratio. The varied Re number tests were to show whether the effect of pulsation is Re independant. The no orifice run was to see what effect the pulsation has on the pipe itself.

Most tests included:

- flow visualization to see the flow instabilities,
- pressure measurements of the pressure drop accross the orifice plate,
- the acoustic node distribution,
- the velocity near the vena contracta,
- the velocity in the Q section, and
- measurements of the flow rate (except where erroneous due to reversed flow).

Thus, knowing the flow rate, and the pressure drop, the C_D and ΔC_D could be calculated and thus the effect of the pulsation on the orifice plate at different frequencies, Reynolds numbers and beta ratios were determined. The results of these tests are discussed in Chapter 3.

Some of these values were summarized and printed for each photograph on what we call the data summary sheet. A sample is given in Figure 2.10. Other values were calculated separately in a spreadsheet and tabulated there. The data summary sheet contains the velocity and pressure distribution predicted

by the NNP, the photo phase finder graph, pulsation settings, and a number of pressure and velocity measurements. The photo phase finder graph gives the normalized curves of the pulsator signal and the HWT along with the signal that sets off the single strobe flash for the photograph. The rising edge of the strobe signal is when the photograph was taken. From this we can see that the photo in this example took place roughly at a velocity minimum measured by the HWT. (Note: In most cases, the HWT values are slightly off since the transducer was just downstream of the smoke wire which slightly heated the air and affected the measured velocity. One measurement was taken at each frequency without a photograph being taken to avoid this problem.)

2.5 Summary of Experimental Design

A complex apparatus was designed and built that is capable of measuring the effect of pulsation on the C_D of an orifice plate flow meter. It used a computer to control the flow rate measurement, taking of photographs, and acquisition of: acoustic data, the pressure drop across the orifice plate, and other velocity and pressure data. It is the first instrument to combine these measurements with flow visualization. This rig worked at a range of velocities from 1 to 5 m/s and a pulsation frequency range of 8 to 300 Hz. Control of the amplitude of pulsation was possible, independent of flow rate. This allowed pulsation with zero flow rate. Two different beta ratios were tested, and experiments could also be done with no orifice plate.

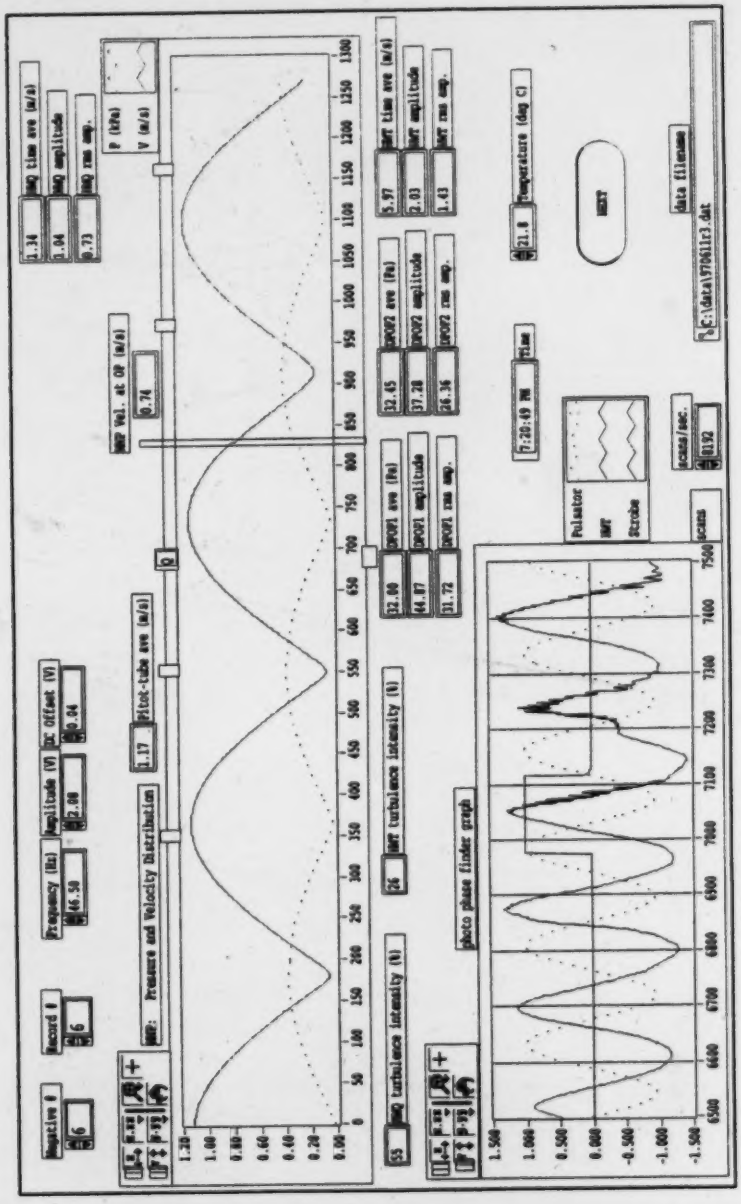

Figure 2.10: Data Page for 970611R3N06

Preliminary tests in a wind tunnel were used to test and refine experimental techniques. These were then applied to the design of a test rig which was built exclusively to study the role that large scale vortex structures have in pulsation induced orifice plate flow metering error. Experiments were done by measuring the flow rate with a hot-wire anemometer traverse, and by measuring the pressure drop across the orifice plate both with and without pulsation. The resulting effect on the C_D could then be calculated and compared with the photographs. This is discussed in length in the next chapter.

CHAPTER 3

RESULTS AND DISCUSSION

3.1 Introduction

Experiments were performed using the procedures and apparatus discussed in the previous chapter. The results from the experiments done in the square wind tunnel are provided in Section 3.2. This discussion provides some of the necessary concepts we will use later. Results from the round pipe begin in Section 3.3. For the round pipe it was found that under the influence of pulsation there can be a large error in the indicated flow rate when it is measured by an orifice plate flow meter. We will propose here a logical chain of independent concepts to explain why this happens. Each link will be discussed briefly. This chain of logic is not to be confused with a causal chain of events, for in actuality it is all happening at once and it is erroneous to think that one causes the other. This proposed mechanism for pulsation induced error due to influencing the large-scale vortex structures in the turbulence is discussed in Section 3.4. (Note that there are other ways pulsation can

induce meter error. For example the hypothesized acoustic streaming discussed in Section 3.4.3.1, or the high pressure amplitude but low Strouhal number pulsation discussed in (Jungowski et al., 1990).)

The first concept concerns the modification of the vortices, causing larger ones to occur closer to the orifice plate than they normally would. This is discussed in Section 3.4.1. The vortex modification is usually accompanied by a narrowing of the vena contracta (Section 3.4.2), a decrease in the reattachment length (Section 3.4.2), and an increase in the pressure drop across the orifice plate (Section 3.4.3), while the flow rate remains constant (Section 3.5.4). A larger pressure drop across the orifice plate for the same flow rate means that the discharge coefficient has decreased. (In a few cases, the opposite effects were observed.) This change in the discharge coefficient is discussed in Section 3.5, and included in the discussion are the effects of varying:

- amplitude of pulsation (Section 3.5.1),
- frequency of pulsation (Section 3.5.2),
- Reynolds number (Section 3.5.3),
- acoustic node position (Section 3.5.5), and
- beta ratio (Section 3.5.6).

3.2 Square Wind Tunnel Results

Several rolls of film were taken using the previously mentioned experimental setup in Section 2.2. This was a preliminary experiment to test some of

the flow and apparatus concepts. The twelve best photographs were printed and analysed. Three have been selected for discussion here to elucidate the concepts discussed earlier in the introduction, Section 1.2.

It was possible to measure the speed of the flow from the 12 photographs, since the frequency of the streakline density oscillations (f_{smoke}) is known. The calculation of the velocity is from the wavelengths in the smoke measured on the photographs. Figure 3.1 is an example. The smoke wire is located upstream of the orifice plate. This gives a good indication of the upstream velocities. The velocity was calculated using the formula: $U = f_{smoke}\lambda_{smoke}$, where λ_{smoke} is the wavelength. The wavelengths of the varying smoke densities were measured on the pictures, and averaged to get 0.64 m/s upstream and approximately 3.0 m/s downstream of the orifice plate (U_v). This is an increase in velocity of 4.69 times. From conservation of mass, the velocity is inversely proportional to the cross-sectional area, assuming constant density (which is a good assumption at this velocity (Mach number=0.01)). Assuming this is the uniform velocity inside the vena contract, it means that the vena contracta causes a 17% decrease in the area of the orifice since the orifice area is one quarter of the test section diameter ($\beta = 0.5$). This predicts a vena contracta of 0.16 m in diameter which is $0.93d$. These calculations are only included as an example of what can be done when there is a non-turbulent upstream flow; these numbers are approximate.

The velocity was then used in calculating the length of the expected wavelengths of turbulent structures that would be forced given the frequency of

Figure 3.1: Velocity Measurement $f_p = 60$ Hz

pulsation, using $\lambda_p = \frac{U_c}{f_p}$. In this case, the frequency f_p is the pulsation frequency coming from the subwoofer, the velocity U_c is the expected convection velocity of the turbulent structure, and the wavelength λ_p is that predicted for the large scale structure corresponding to the instability. The convection velocity was considered as roughly half U_v, so 1.45 m/s was used as the convection velocity since the original calculations for U_v resulted in 2.90 m/s. For Figures 3.2 and 3.3, the estimated λ's are 23 mm for 60 Hz, 46 for 30, 92 for 15, 184 for 7.5 and 368 for 3.75. (The three photographs are included here at a scale of 1:5.) Some λ's are indicated on Figure 3.3.

Figure 3.2 and 3.3 are photographs with the smoke wire located directly downstream of the orifice plate to give a good visualization of the turbulence in the flow. The edges of the photograph are approximately the tunnel walls. Figure 3.2 has no pulsation and Figure 3.3 has $f_p = 15$ Hz, a frequency estimated to be four times the expected shedding frequency. The preliminary pulsation system used in the wind tunnel could not reach as low as the shedding frequency. (The circular pipe test rig discussed in the next sections was better able to do this.) Even with the relatively low levels of pulsation available, note the qualitative difference between the two photographs. In Figure 3.2, some turbulent structures can be seen at the edge of the approximately uniform streaklines along the centerline of the photograph. In Figure 3.3, the 15 Hz excitation is organizing the structures (the estimated λ_p corresponding to 15 Hz is shown) and creating much stronger fluctuation in the uniform streaklines near the centerline. This uniform potential flow

Figure 3.2: Orifice Flow, No Pulsation

Figure 3.3: Orifice Flow, Pulsation at 15 Hz

region is apparently destroyed more quickly with downstream distance with pulsation than without.

The most important thing about Figure 3.3 is that other wavelengths of structures are apparent as well. Estimated wavelengths for vortex structures occurring at 60 Hz and 30 Hz (higher harmonics of the 15 Hz pulsation) are indicated on the figure. By comparing the wavelengths observed on the photograph it can be seen that the first vortices occur at about 60 Hz. As they convect downstream, they pair (two vortices combining to form one) and vortices occurring at 30 Hz can be identified. These then pair to make the clearly visible 15 Hz vortices corresponding to the pulsation frequency. No vortex structures corresponding to a 7.5 Hz wavelength can clearly be seen, but may be apparent at other instants in time. A large structure on the lower right (when looking with flow from left to right) with wavelength near that expected for 3.75 Hz can be seen. This frequency is very close to the predicted value of 3 Hz estimated for the shedding instability. Note that a sinuous instability appears in the flow; the structures near reattachment appear staggered from one side of the tunnel to the other. (Using the above information, the frequencies of the jet and shedding instabilities can be calculated:

$$f_j = \frac{St_j U_v}{D_v} = \frac{0.3 \times 300}{17} = 5.31 Hz \tag{3.1}$$

$$f_{sh} = \frac{St_{sh} U_v}{H_v} = \frac{0.08 \times 300}{8} = 3 Hz.) \tag{3.2}$$

This is very convincing evidence that the shear layer and shedding insta-

bilities are present in this flow. The jet instability is expected to occur at a slightly higher frequency than the shedding, but it is difficult in this geometry to separate the two instabilities. It is most likely that both instabilities play a role. The structures at this point are interacting both with the wall and their partners from the opposite side of the flow. It is expected that strong pulsation near the shedding frequency could cause the corresponding large structures to move nearer the orifice plate causing the maximum measurement error. This is shown to be true in the circular pipe results discussed later in this chapter.

From the equations, $\lambda = \frac{U_c}{f}$, $U_v = 2U_c$, $St_{sh} = \frac{fH_v}{U_v} = 0.08$, and $St_j = \frac{fD_v}{U_v} = 0.3$, the following relations can be derived, and used for "rule of thumb" estimates:

$$\lambda_{sh} = \frac{H_v}{2St_{sh}} = 6.25H_v \tag{3.3}$$

and

$$\lambda_j = \frac{D_v}{2St_j} = 1.7D_v. \tag{3.4}$$

In summary, the square wind tunnel results have confirmed the value of using the smoke wire technique for this flow. They have also shown that three turbulent instabilities seen in other flows appear to occur in orifice plate flow. These are the Kelvin-Helmholtz instability, the jet instability, and the shedding instability. Depending on the beta ratio, not all three instabilities will necessarily be present. It was found with $\beta = 0.5$, that all three instabilities are present, and occur at roughly the same Strouhal

numbers as expected from the other flows they appear in. These instabilities could be influenced by pulsation, changing the nature of the flow. It was anticipated that stronger pulsation could move the large vortices nearer the orifice plate which would more strongly influence the vena contracta and create an erroneous flow measurement. Therefore it was decided to go ahead with more in-depth experiments in a fully turbulent round pipe.

3.3 Introduction to Round Pipe Data

Experiments were performed in the round pipe rig described in Section 2.3. The detailed conditions are given in Table 3.1. Pulsation velocity amplitudes (compared to the approximate U_v in %) ranged from 2 to 25% for the $\beta = 0.5$ plate. One experiment was done on the $\beta = 0.65$ plate at a level of 35%. The velocity was varied to check the Strouhal number scaling proposed, to give greater variation in pulsation amplitude, and to test the importance of Reynolds number. Several dozen rolls of film were exposed and over 1 gigabyte of measurement data was recorded. Twenty-five of these photographs have been printed here at a scale of 4:5 (rotated 90 degrees counterclockwise to fit the page better). A dozen are used to elucidate the concepts as discussed in this chapter. The rest are included in Appendix D as a sample of the data, along with a summary sheet of data for each photograph and a table with the pertinent parameters for the whole run.

Table 3.1: Experiment Settings

Date	Pulsation Level	Approx. U_{pipe}	Re	Comments
970609	25%	1 m/s	9000	SW DS, no data without photo's
970611	13%	1 m/s	9000	SW DS, no NoX data without photo's
970616	2%	5 m/s	47000	
970618	9%	2 m/s	20000	
970620	4.5%	2 m/s	20000	
970624	25%	1 m/s	9000	Repeat of 970609 and bad HWT
970626	25%	1 m/s	9000	No Orifice Plate
970630	9%	1 m/s	9000	Photographs include upstream flow
970703	35%	1 m/s	9000	$\beta = 0.65$

("SW DS" indicates smoke wire (SW) is downstream (DS) of the orifice plate. Otherwise it is upstream.)

3.4 A Proposed Mechanism for Pulsation Induced Meter Error

We present here the details of the proposed mechanism for pulsation induced meter error introduced in Section 3.1. It is primarily based on observations from photographs such as Figures 3.4, 3.5 and 3.6. The first concept concerns modification of the vortices by the pulsation, causing larger vortices to occur closer to the orifice plate than they normally would. The vortex modification is accompanied by a narrowing of the vena contracta, a decrease in the reattachment length, and an increase in the pressure drop across the orifice plate, while the flow rate remains constant. A larger pressure drop across the orifice plate for the same flow rate means that the discharge coefficient has decreased. Experimental evidence for each aspect is provided and discussed below.

Figure 3.4: Photograph: No Pulsation, $U_{pipe} = 0.96$m/s, $U_v = 5.9$m/s, $\Delta P_{OP} = 24.4$Pa

Figure 3.5: Photograph: High Frequency Pulsation. $St_{sh} = 1.5$, $St_j = 2.1$, $U_{pipe} = 0.96\text{m/s}$, $U_v = 5.7\text{m/s}$, $\Delta P_{OP} = 23.4\text{Pa}$

Figure 3.6: Photograph: Low Frequency Pulsation, $St_{sh} = 0.33$, $St_j = 0.42$, $U_{pipe} = 0.96$m/s, $U_v = 6.3$m/s, $\Delta P_{OP} = 32.3$Pa

3.4.1 Vortex Modification

The explanation of vortex modification given here is intended to be just enough to help explain the proposed mechanism. For a more complete explanation of these concepts refer to (Sigurdson, 1995).

As mentioned in Section 1.2, vortices are being shed at the edge of the orifice plate, are convecting downstream, and are pairing up as the shear layer grows. These vortices, and how they are affected by pulsation, can be seen in the photographs. Figure 3.4 is with no pulsation, Figure 3.5 is with a high frequency of pulsation and Figure 3.6 is with a frequency of pulsation near where the largest effect occurred. The expected wavelength of the structures seen could be estimated. This estimation was done using $\lambda_p = \frac{U_c}{f_p}$ as was done with the wind tunnel results. U_c, the convection velocity of the vortices, was estimated as $\frac{U_v}{2}$. U_v was estimated using the measurement from the HWT which was in the center of the flow, 25 mm (1") downstream of the orifice plate (OP). Figure 3.5 shows the expected wavelength of 14 mm for a pulsation frequency of 198.5 Hz. As in the wind tunnel analysis, many wavelengths of structures are apparent. The first vortex shed with wavelength of 14 mm is at 198.5 Hz, and then pairs to get the 28 mm at 99 Hz, and again to get 56 mm at 48 Hz. Some of these are also visible in Figure 3.4. The frequency of pulsation for this photograph is above the shedding and jet instability range and at a pulsation level of 10%. The 56 mm wavelength vortex is within the range for these instabilities and Figure 3.6 shows what can happen when a high enough pulsation level is used in the frequency range

of the instabilities. This figure shows a 68 mm vortex which corresponds to the pulsation frequency which is slightly lower than one quarter of the frequency in the previous figure. The vortex previously occurring further downstream has moved right up to the orifice plate and the ΔC_D for this photograph is -13%. This is an example of the type of vortex modification which can cause a reduction of the vena contracta and meter error. For these photographs the smoke wire was just downstream of the orifice plate which resulted in a lot of smoke getting into the shear layer. These are examples of the observations used in developing the proposed mechanism explained here.

Figures 3.7 and 3.8 were taken with the smoke wire 76 mm upstream of the orifice plate which gets more smoke into the potential core region. Figure 3.7 is with no pulsation and shows the streak lines clearly in the jet portion of the flow with some wavy edges on the top and bottom. These wavy edges are what is visible of the vortices in the shear layer. They are there, but are not able to draw the smoke from the jet flow into the shear layer to make them visible. These vortices have a frequency associated with them as discussed earlier. If that frequency is forced, these vortices are likely to move closer to the orifice plate and also appear to entrain more smoke. This was clearly seen in Figure 3.6 where the 68 mm vortex moved right up to the orifice plate. It entrained a tremendous amount of smoke giving a ΔC_D of -13% with a pulsation level of 13%.

Figure 3.7: Photograph: No Pulsation, Re=20.000

Figure 3.8: Photograph: Low Frequency Pulsation, $St_{sh} = 0.16$, $St_j = 0.32$, Re=20,000, $\frac{u'}{U_e} = 8.6\%$, $\Delta C_D = -6.4\%$

3.4.2 Narrowing of Vena Contracta and Reattachment Length

Apparent in the pulsated photograph is that the vena contracta has been reduced, at least for the instant of the photograph, due to the large vortex reaching into the core of the jet coming through the orifice plate. This reduction in vena contracta causes an increase in the velocity U_v, since the velocity is inversely proportional to vena contracta diameter squared. A faster U_v through Bernoulli's principle translates to a reduction in the pressure downstream of the orifice plate. If it is assumed that the pressure upstream is unchanging, this is an explanation of why the pressure drop across the orifice plate is increasing. The vena contracta is the minimum diameter between the two reversed flow regions shown in Figure 1.3b. To accurately measure it, the actual dividing streamlines (stream surface) of the separation bubble must be calculated from velocity measurements of the entire flow field. Therefore here we only surmise what it is doing by looking at the streaklines. Also seen in this figure is the reattachment "point" (which is actually a circular reattachment "line"). The distance from the orifice plate to the reattachment point is called the reattachment length. The measurement of the vena contracta and the reattachment length both come from averages over time since things are changing many times a second due to pulsation and turbulence. The average of these is what needs to be used. We can see in the photographs that instantaneously, values of the vena contracta appear to range significantly from what can be seen in the unpulsated and pulsated photographs. Even though we could not accurately ascertain the average

vena contracta from the photographs, it was possible to estimate the vena contracta diameter (D_v) using the measured Q and the HWT velocity near the vena contracta. This gives a better estimate than the approximation that $D_v = d$. The HWT was 25 mm downstream of the orifice plate, and the position of the vena contracta for this β has been estimated at 1D (Jungowski et al., 1990), or in this case, 146 mm. An example of this estimation of D_v is given in Figure 3.4 which includes the photograph and some necessary data. For this case it was 0.8d. The vena contracta was estimated to be 0.8d by using the assumption of constant volume flow rate and a uniform velocity profile in the vena contracta (the former a good assumption, the latter less so):

$$D_v = D\sqrt{\frac{U_{pipe}}{U_v}} \tag{3.5}$$

Figures 3.4, 3.5 and 3.6 use this estimate of the vena contracta to calculate the Strouhal numbers but all other data still uses the simpler approximation that $D_v = d$.

Through these HWT measurements, it was confirmed that generally the vena contracta is narrower with pulsation than without. However it was usually only a reduction of a few percent. Due to the location of the hot-wire and other inaccuracies in our D_v calculation technique it is expected to be greater than this.

We also have information concerning the reduction of the reattachement

length. From the tufts mentioned in Section 2.3.3.5, the reattachement length could be seen to get shorter during pulsation. This was a subjective measurement, as the tufts needed to be watched carefully to determine their mean position, and which direction they spent most of their time in. The ones that spent most of the time pointing upstream were in the recirculation region, while those spending most of their time pointing downstream were where the flow had already reattached. There were always a few tufts inbetween these two that spent essentially equal amounts of time pointing upstream and downstream. These tufts, often only one, identified where the reattachement point was.

An intriguing aspect of Figure 3.5 is that the estimated vena contracta is actually a little larger compared to the no pulsation case (2.5% more) and the pressure drop is a little smaller (4.2% less). The ΔC_D is +2.2% which is smaller than our uncertainty (of 5%) in ΔC_D at this velocity, although the ΔC_D for the $\beta = 0.65$ run at $St_{sh} = 1.7$ is +8% which is greater than the uncertainty. This increase in C_D happened in only a few of the cases tested, always at higher frequencies, and only the one had a ΔC_D greater than the uncertainty. It is likely that this higher frequency of pulsation is keeping the larger vortices farther away from the orifice plate where they have less of an effect. In a sense it is, for a portion of its streamwise extent, since the pulsation slows down the growth of the shear layer by supressing pairing and therefore giving a wider vena contracta. This is known to happen in free shear layers (Oster and Wygnanski, 1982).

3.4.3 Increased Pressure Drop

The link between the narrower vena contracta and the higher pressure drop is expected to be through the flow speeding up due to the smaller effective area it has to go through. Bernoulli's principal for steady flow along a streamline would suggest that this increase in velocity in the vena contracta will result in a reduction of pressure there. Although this flow is unsteady, a similar response is expected here. This sets the pressure in the separated region downstream of the orifice plate, effectively reducing it as well. This pressure was not measured, only the difference in pressure between the two flange taps used in orifice plate flow meters. This reduction in downstream pressure is expected to cause the increase in pressure drop as we assume the upstream pressure remains roughly the same.

In a few cases, the vortex modification resulted in a widening of the vena contracta. This occurred when the non-dimensional frequency was three times that of the regime where the jet and shedding instabilities occurred. Through similar, but opposite, logic to that explained above, this coincided with a reduction in the measured pressure drop.

This completes the logical chain of concepts we propose to explain (at least partially) how the pulsation can affect the discharge coefficient resulting in meter error. In the next section, we will have a short discussion of some unusual pressure drop results that can take place with no net flow in the pipe. These results have a slight influence on the interpretation of the detailed pressure drop measurements which are discussed in Section 3.5.1.

3.4.3.1 No Flow

To conclusively determine whether the effect on the C_D was primarily caused by the vortex manipulation described in previous sections, and not some other effect, it was necessary to do some tests without any net air flow ($Q = 0$). This was to measure the magnitude of an observed effect the pulsation has on the pressure drop across the orifice plate *even with no flow.* Although this phenomena is not understood, we wanted to determine that even if a similar thing *was* happening *with flow* (we do not know that it does or does not), it could not be responsible for the pressure drop increases we were recording. These tests were also used in part to calibrate the pulsator to the desired pulsation levels as measured by the NNP.

Figure 3.9 shows the amount of ΔC_D versus St_{sh} at a pulsation level of 25%. Also plotted are two pressure measurements. One of the two pressure measurements plotted is the difference (in Pascals) between the pressure drop with pulsation and the pressure drop with no pulsation when flow is present for both. The other pressure measurement plotted is the pressure drop measured across the orifice plate with pulsation but no flow. The first thing to note is that at many frequencies there is a measureable pressure drop across the orifice plate with pulsation *even when there is no flow.* This is generally much smaller than the difference measured between pulsation and no pulsation when there is flow. It is clear from this graph that, for these conditions, the major cause of the ΔC_D is from the vortex modification (which rises to as much as 23 Pa) and not this slight pressure drop at no

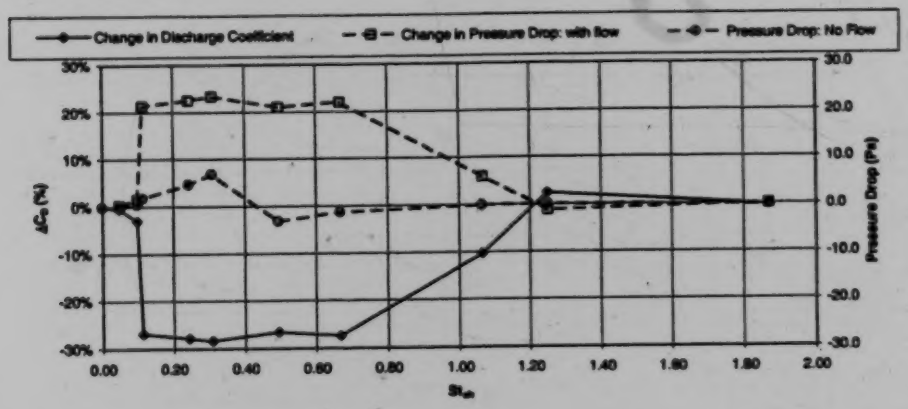

Figure 3.9: Graph Comparing Pressure Drop With and Without Flow ($U_{pipe} \approx 1$ m/s, $\frac{u'}{U_o} = 25\%$)

flow (which is never more than 7 Pa). It can be seen that the effect on C_D correlates closely with the change in pressure drop measured with flow. This pressure drop measured without flow does not correlate with ΔC_D. These conditions of lowest U_{pipe} and highest amplitude were those where the effect on ΔC_D would be strongest. Other runs that are at higher U_{pipe} and lower pulsation amplitude would be less influenced by this effect. Note that the effect can also cause a slight pressure *rise* at some frequencies.

The cause of this pressure drop with no flow is not understood, although one possible explanation is that it may be a result of acoustic streaming. This is a phenomenon whereby acoustic excitation produces a localized recirculating flow between the nodes and antinodes of a standing wave in a pipe. Acoustic streaming has also been investigated in connection with orifices (Lebedeva, 1980) but no investigation was found of how this phenomenon

affects the combination of an orifice plate and a pipe, and thus orifice plate flow metering error.

This phenomenon whereby there is a pressure drop across the orifice plate with no net flow is interesting. However, it has not been further investigated here as it was outside the scope of the present project and would need to be part of another project. When there is flow, this phenomenon is another potential cause of pulsation induced metering error but causes less of an error than vortex modification under the conditions tested. This is not necessarily always the case. It comes into play when pulsation amplitudes are high and flow rates are low. When there actually is no flow, this phenomenon can of course be giving tremendous error, by indicating a flow when there is none.

3.5 Reduction of the Discharge Coefficient (C_D)

3.5.1 Pulsation Levels

The end result of the pulsation on the flow is that, in most cases, the C_D is significantly reduced. A number of tests were done at different levels of pulsation, and the results are summarized in Figure 3.10. (It should be noted that for both Figure 3.10 and 3.12, the secondary x-axis of St_j is not valid for the 0.65 β run. For the 0.5 β ratio runs, St_j is double St_{sh}, since D_v is double H_v. This is only the case when the β ratio is 0.5 and so does not apply to the 0.65 β run. The St_{sh} is still valid.) This graph gives the ΔC_D versus the non-dimensional frequency of pulsation (St_j or St_{sh}). As can be

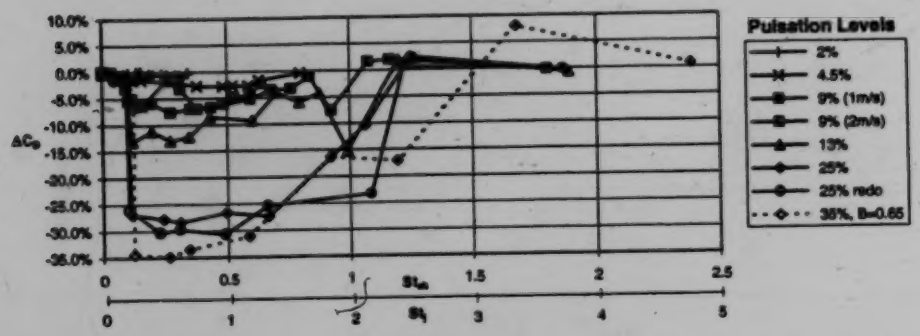

Figure 3.10: Complete Set of ΔC_D vs Non-dimensional Pulsation Frequency (St_j or St_{sh}) at Different Pulsation Levels

seen from this graph, there is significant effect in roughly the same range of St for all levels of pulsation tested. The maximum effect is roughly linear with pulsation level as can be seen in Figure 3.11 where the maximum from each pulsation level was plotted versus its pulsation level. The least squares best fit line of

$$\Delta C_{D_{max}}\% = 2\% - 1.15\left(\frac{u'}{U_o}\%\right) \tag{3.6}$$

is plotted with these points.

The maximum effect measured was a reduction in C_D of 34%. At a similar normalized pressure pulsation level, Jungowski et al. (1990), who were in a much lower range of St ($St_j = 0.014$), recorded their maximum effect as a reduction in C_D of 11%.

Outside of this range of maximum effect, the amount of effect on the C_D drops off rapidly. It should be noted that some of the frequencies at either end for each run were not at the stated pulsation level since the pulsator was

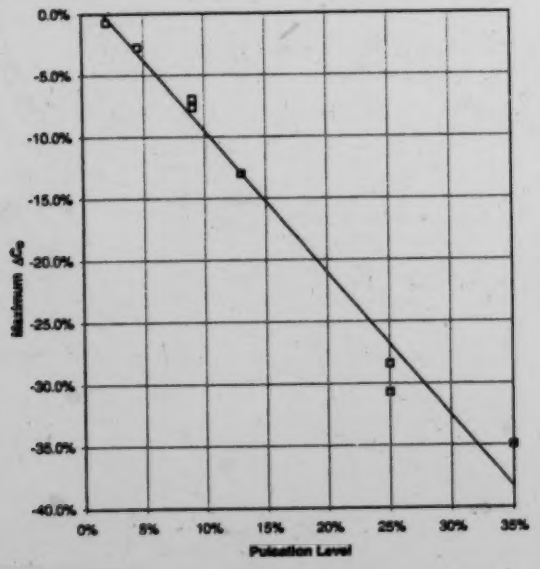

Figure 3.11: Maximum Effect on C_D vs Pulsation Level

not strong enough. Figure 3.12 is similar to Figure 3.10 but has all points with less than the stated pulsation level removed. Also removed are a few points with erroneous pressure measurements due to resonance in the hoses to one of the transducers. Most of these still have enough points to show that the effect is dropping off at either end of this maximum range of St.

We need to look at one more plot to adequately explain the effect of pulsation level. Figure 3.13 shows the effect on C_D for only one run. It can be seen that the point at a St_{sh} of 1.1 has a pulsation level lowered by 6% (from 26% to 20%) but the $|\Delta C_D|$ has dropped by 17% (from 27% to 10%) from St_{sh} of 0.7. This is far from the linear relationship with slope of -1.15 seen at the range of maximum effect and further reinforces that this large

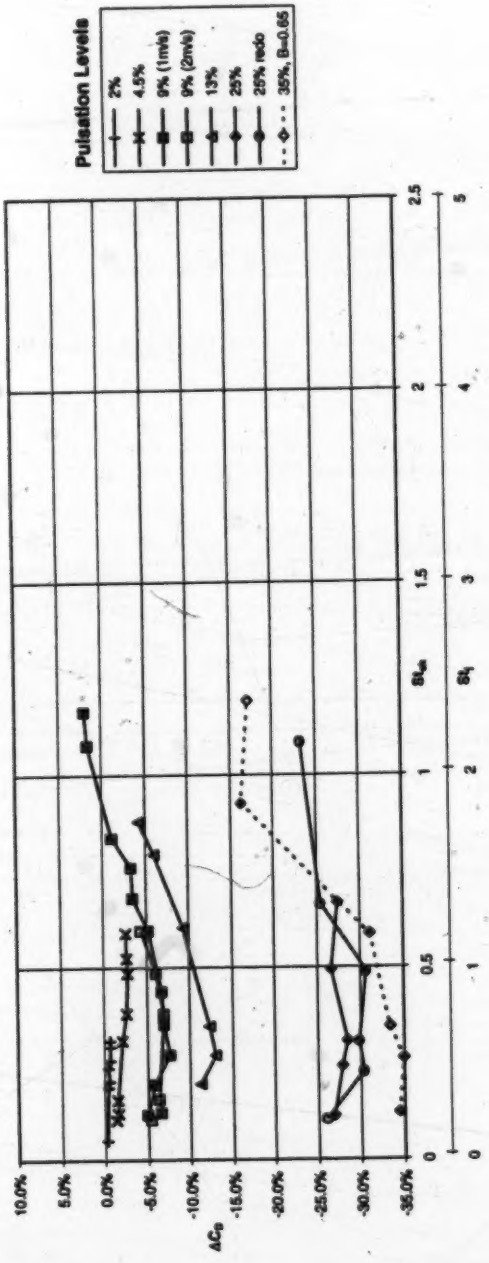

Figure 3.12: Partial Set of ΔC_D vs Non-dimensional Pulsation Frequency (St_j or St_{sh}) at Different Pulsation Levels

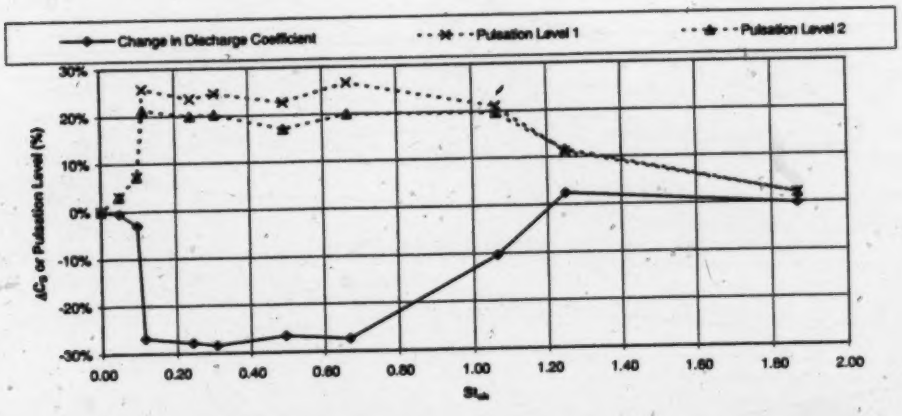

Figure 3.13: Graph Showing Effect on C_D Along With Two Measures of the Pulsation Level: Pulsation Level 1 is the amplitude of velocity pulsation at the OP measured by the NNP divided by $6U_{pipe}$; Pulsation level 2 is the same amplitude of velocity pulsation divided by the velocity measured by the HWT. ($U_{pipe} \approx 1$ m/s, $\frac{u'}{U_\infty} = 25\%$)

effect on C_D drops off outside the range of St_{sh} of roughly 0.2 to 0.5.

Another noteworthy point is the reproduceability in the repeat of the 25% pulsation run and in the two runs at 9% but at two different speeds. These are reasonably close to each other which demonstrates a reasonable repeatability in the tests, that the St scaling is correct, and that the Re is *not* important to the effect since it has doubled.

Figure 3.13 shows the amount of ΔC_D versus St_{sh} along with two different normalizations of pulsation. The pulsation levels stated in the text and in figures were calculated as the velocity amplitude from the NNP divided by six times the mean upstream velocity. This number would be expected to be four rather than six since the area of the orifice is one quarter of the

pipe area. However, the flow narrows to less than the diameter of the orifice which results in a faster velocity. This was measured using the HWT to be better estimated by six times the mean upstream velocity. (The estimate for the 0.65 β run was measured to be about four times the mean upstream velocity). These are not exact but quick estimates to simplify the experimental procedure.

The other pulsation level used was the velocity amplitude from the NNP divided by the mean velocity in the center of the pipe, just downstream of the orifice plate as measured by HWT.

3.5.2 Different Instabilities

One of the major objectives of this project was to show that pulsation induced meter error caused by vortex modification is frequency dependent. As explained in Section 1.2, each of the turbulent instabilities present in the flow respond to a specific range of frequencies. Some of these instabilities had an obvious effect, while others had no noticeable effect at the frequencies tested.

Each of the instabilities identified in the flow are discussed in relation to Figure 3.12 and what role each instability has in affecting the C_D. The tests were designed around the two instabilities that were expected to have the greatest effect, the jet and shedding instabilities.

3.5.2.1 Jet and Shedding Instabilities

The largest effect on the C_D is in this region which is from roughly 0.2 to 0.5 in St_{sh} and 0.3 to 1 in St_j. In other flows, the shedding instability generally occurs around St_{sh} of 0.08, but the pulsation frequency that it responds to is often 2 to 4 times that, so up to a St_{sh} of about 0.3 (Sigurdson, 1995). The jet instability generally occurs around 0.3 to 0.5. From Figure 3.10 it can be seen that this largest effect is occurring at the range of St that corresponds to both the jet and shedding instabilities. They overlap when $\beta = 0.5$.

The size of the vortex in Figure 3.14 corresponds to the pulsation frequency ($f_p = 46.5$ Hz) which is at $St_{sh} = 0.23$ and $St_j = 0.46$. The pulsation level is 25% and the ΔC_D is -30%. Therefore both the shedding and jet instabilities are important, as this frequency is seen to amplify into a big vortex. The actual vortex corresponding to the shedding instability is expected to occur after about two more pairings and so is likely a little bit further downstream. It is evident that for $\beta = 0.5$ and 0.65, the area of concern is at $St_{sh} = 0.2 - 0.5$ and that this frequency regime should be avoided. The range widens with increasing pulsation level.

Another way to see when the pulsation is being amplified is by looking at the turbulence intensity measured by HWT. Some preliminary analysis of the velocity traces has been done. Figure 3.15 provides the total RMS turbulence intensity (entire signal, not just at the pulsation f) from the HWT velocity data for each frequency of pulsation tested in the 970630 run. It shows how the flow amplifies the pulsation when forcing at frequencies near the shedding

Figure 3.14: Large Effect Around Expected Jet and Shedding Frequency Re=9,000, $St_{sh} = 0.23$, $St_j = 0.46$, $\frac{u'}{U_v} = 25\%$, $\Delta C_D = -30\%$

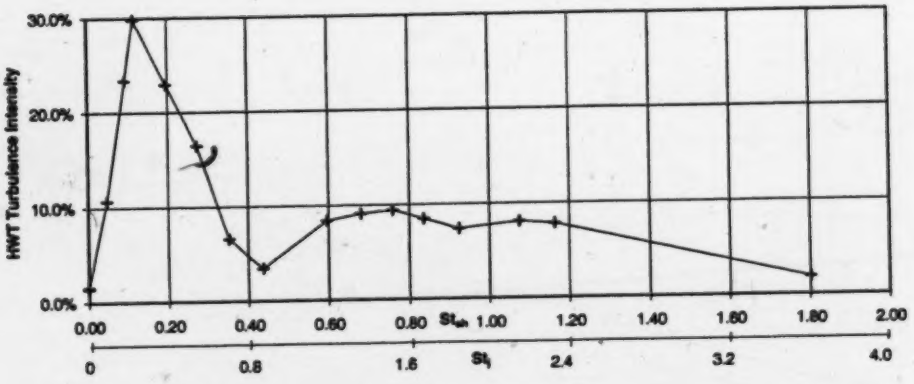

Figure 3.15: HWT Turbulence Intensity Versus St_{sh} and St_j for $\frac{u'}{U_\infty} = 9\%$

and jet instabilities. The turbulence intensity rises to 30% from its otherwise typical value of less than 10% at other frequencies. The pulsation amplitude is 9% for this data.

A significant discovery occurred for at least one of the frequencies tested in this range. The pulsation level was high enough to momentarily reverse the flow. This can be seen in Figure 3.16 where the smoke is seen upstream of the OP, and the smoke wire is just downstream of the OP. This was close to the largest pressure drop and largest ΔC_D. This reversing of flow may also have happened at other frequencies but was not clearly visible. This occurred with a pulsation level of 25% and at a St_{sh} of 0.11. The centre of the flow is going downstream, but near this instant in time, the flow at the edge of the orifice is going upstream.

Figure 3.16: Reversed Flow, Re=9,000, $St_{sh} = 0.11$, $St_j = 0.22$, $\frac{u'}{U_o} = 25\%$, $\Delta C_D = -26\%$

3.5.2.2 Kelvin-Helmholtz Instability

The Kelvin-Helmholtz Instability covers a large range of frequencies, starting at the initial KH frequency and working down lower and lower as the vortices pair up and double in size. Once large enough, they include the jet and shedding instability. Each of these vortices along the way between KH_i and the jet and shedding instabilities, has the potential to also be modified and affect the pressure drop across the orifice plate in the same manner, but with less effect than jet and shedding since these vortices are smaller. Figure 3.17 shows a photo with the frequency in this range between KH_i and the jet and shedding instabilities.

The vena contracta appears to be somewhat narrower, but not as much as with the jet and shedding instabilities. These vortices are smaller, but still affect the C_D. The ΔC_D for this case was -23%, less than the -31% at the jet and shedding frequency with the same pulsation level.

The highest frequency in this range is at the initial Kelvin-Helmholtz instability which is $St_{KH} = \frac{f_{KH_i}\theta}{U_c} = 0.032$. Since we don't know the momentum thickness (θ), we can estimate f_{KH_i} from Figure 3.18. This photograph is with pulsation at St_{sh} of 1.2 and $\frac{u'}{U_o}$ of 15%. These vortices seen just downstream of the orifice plate are the smallest seen in any of the photographs, and so are considered to be roughly the size of the initial KH vortex. The wavelength of this vortex is measured at roughly 8 mm, and $U_c = 3\ m/s$, therefore $f_{KH_i} = \frac{U_c}{\lambda_{KH_i}}$ is approximately 375 Hz. This is for the 1m/s flow, and for this speed, is roughly eight times higher than the jet instability and

Figure 3.17: Intermediate Frequency Effect Re=9,000, $St_{sh} = 1.1$, $St_j = 2.2$, $\frac{u'}{U_v} = 25\%$, $\Delta C_D = -23\%$

two times higher than we could pulsate with a reasonable amplitude. At the higher flow rates, this frequency is also higher.

We also have some HW measurements with the HWT on the edge of the shear layer, 25 mm (1") downstream of the OP with no pulsation. The frequency was measured to be between 180 and 230 Hz, and this is expected to be about one half of the actual f_{KH_i} since the probe was not close enough to the orifice plate. It was actually measuring the frequency of the second vortex which is twice the size of KH_i and hence half the frequency. Therefore $f_{KH_i} \sim$ 400 Hz which was too high for us to pulsate with substantial amplitude with the current test rig.

3.5.2.3 Corner Separation Bubble

The corner separation bubble, not normally discussed in orifice plate literature has been shown to exist. Figure 3.19 shows a typical corner separation bubble. This separation bubble is also expected to have a range of frequencies at which it can be modified, possibly affecting the C_D. If the frequencies of this and the jet and shedding instabilities coincide, an even larger effect on the C_D could result. No noticeable effect on the corner separation bubble was observed in the tests done. Therefore no conclusions about the effect of forcing instabilities in this bubble have been made. The effect would probably be at higher frequencies than we studied, if it exists at all.

Figure 3.18: Initial Kelvin-Helmholtz Vortex
Re=9,000, $St_{sh} \doteq 1.2$, $St_j = 2.4$, $\frac{u'}{U_e} = 15\%$, $\Delta C_D = +0.7\%$

Figure 3.19: Typical Corner Separation Bubble:
Re=9,000, $St_{sh} = 0.27$, $St_j = 0.54$, $\frac{u'}{U_e} = 8.9\%$, $\Delta C_D = -7.6\%$

3.5.2.4 Pipe Turbulence

There are instabilities in the pipe turbulence as well, but having an effect on these was not achieved in the tests done since the main focus was the jet and shedding instabilities. Some photographs were taken without the orifice plate and one is given in Figure 3.20. The orifice plate was replaced with a ring that helps hold the two halves of the test section together with an o-ring to help it seal, just like the orifice plate assembly. From the photograph it can be seen that there is more turbulence near the pipe wall, and more mixing behind the vertical support to the hot-wire. This photograph was taken with no pulsation. No visible change occurred with pulsation.

There is no clear amplification of any of the vortices in the pipe at this frequency. If there is going to be any effect it will likely be at frequencies lower than we could produce with sufficient pulsation levels.

3.5.3 Reynolds Number

One of the important aspects of these instabilities is that they are Re independant (except for the initial KH instability). This suggests that the results taken at these lower Re are relevant to the flows experienced in the field at higher Re. To verify that this is the case in this particular flow, tests were done at three different Re, roughly 9,000, 20,000, and 33,000. Two tests in particular were taken at the same pulsation level, at Re of 9,000 and 20,000. The curves for these are almost identical as seen in Figure 3.12 indicated by the squares. This is evidence supporting the proposition that pulsation

Figure 3.20: Pipe Turbulence: Re=9,000, No Pulsation

induced meter error due to vortex modification is Re independent. Full scale tests need to be done to verify this.

3.5.4 Flow Rate(Q) and Velocity Profiles

As discussed in Section 2.3.5, the test rig was designed with a large extra pressure drop in the pipe in front of the blower. The plan was that this overwhelming pressure drop would dominate the smaller pressure drop across the orifice plate as far as the total pipe pressure loss was concerned. This would hopefully keep the expected change in pressure drop across the orifice plate from affecting the flow rate. Otherwise, adding pulsation to the flow could actually change the flow rate in the pipe. The design worked as planned. This is shown by three different measurements.

The first measurement shows that Q does not change by more than 3% whether the orifice plate is in or not. This was found in one test where at first, with the orifice plate, the average velocity was 0.890 m/s. The orifice plate was removed, and the average velocity was then measure to be 0.887 m/s, a reduction of 0.3%. At least ten minutes later, the orifice plate was replaced and the average velocity slowed to 0.864 m/s. This is a reduction of 3% from the initial measurement with the orifice plate and is more likely due to an increase in temperature in the lab influencing the HWQ. Therefore the actual change in Q could be as bad as 3% but is more likely as low as 0.3%. The largest measured change in pressure drop across the orifice plate under the influence of pulsation with β =0.5 was an increase of 115%. If the absence

of the orifice plate (which might be thought of as an effective decrease in the pressure drop of 100%) only caused a 3% increase in Q, then the largest expected change in Q due to an increase of 115% would be a decrease of approximately 3%. Even though the flow rate measurements are not accurate to within 1% (as discussed in Section 2.3.7), the repeatability of successive Q measurements is. It was found from four successive Q measurements at around 1 m/s that each one varied from its neighbour by less than 1%.

The second measurement shows that the five two-second averages of the HWQ, at 58 mm from the wall, for each frequency remain within 1% of those with no pulsation with only a few exceptions. These exceptions are most likely due to rectification of the velocity signal by the hot-wire.

The third measurement involves some of the tests done to investigate the effect of hot-wire rectification, and is discussed toward the end of this section.

The overall conclusion is therefore that the flow rate is essentially constant for any particular run, except for a small slow variation measured through the course of a run, which was not a function of pulsation. This slow variation was usually about 1%, as little as 0.1%,and in the worst case was 4%. It is speculated that it may result from temperature variations in the lab influencing the hot-wire calibration, and therefore not be a true representation of drift in actual Q.

Originally it was planned to have a measurement of Q for every single value of pulsation frequency and amplitude. The appropriate Q traverse of the hot-wire was recorded, but belatedly, an error was found in the computer

code for calculating the flow rate. As a result, this data has not been used in calculating the ΔC_D. The error did not affect the Q measurement for non-pulsated flow so the value of Q used to calculate the C_D was averaged from the Q's taken with no pulsation. In general there were three: beginning, middle, and end. In calculating the ΔC_D, the Q drops out if it is assumed to be constant.

Figure 3.21 shows what the velocity profile looks like from the output of the flow rate measurement subroutine. The average velocity divided by the maximum is 0.73, which is slightly lower than the 0.791 that Hermann Schlicting predicted (Schlicting, 1979). This is possibly due to a smoother pipe in our tests. The non-symmetry in the profile is thought to be from a slight (less than a mm) missalignment between the section of the pipe upstream of the Q section and the Q section pipe itself. This was calculated to have less than 0.5% of an effect on the Q as explained in Section 2.3.2. A symmetric profile is given in Figure 3.22.

There is a problem measuring the shape of the velocity profile under the influence of high velocity amplitudes of pulsation at the Q section. At some points in the pipe, particularly in the slow moving gas near the pipe wall, the sum of the pulsation and pipe flow could cause the instantaneous velocity to dip below zero. The flow would reverse. The hot-wire anemometer can not detect the sign of the velocity, and the signal is rectified. Only a positive value of velocity is registered. This results in a higher measured value than actual. This rectification is greater near the wall than at the middle of

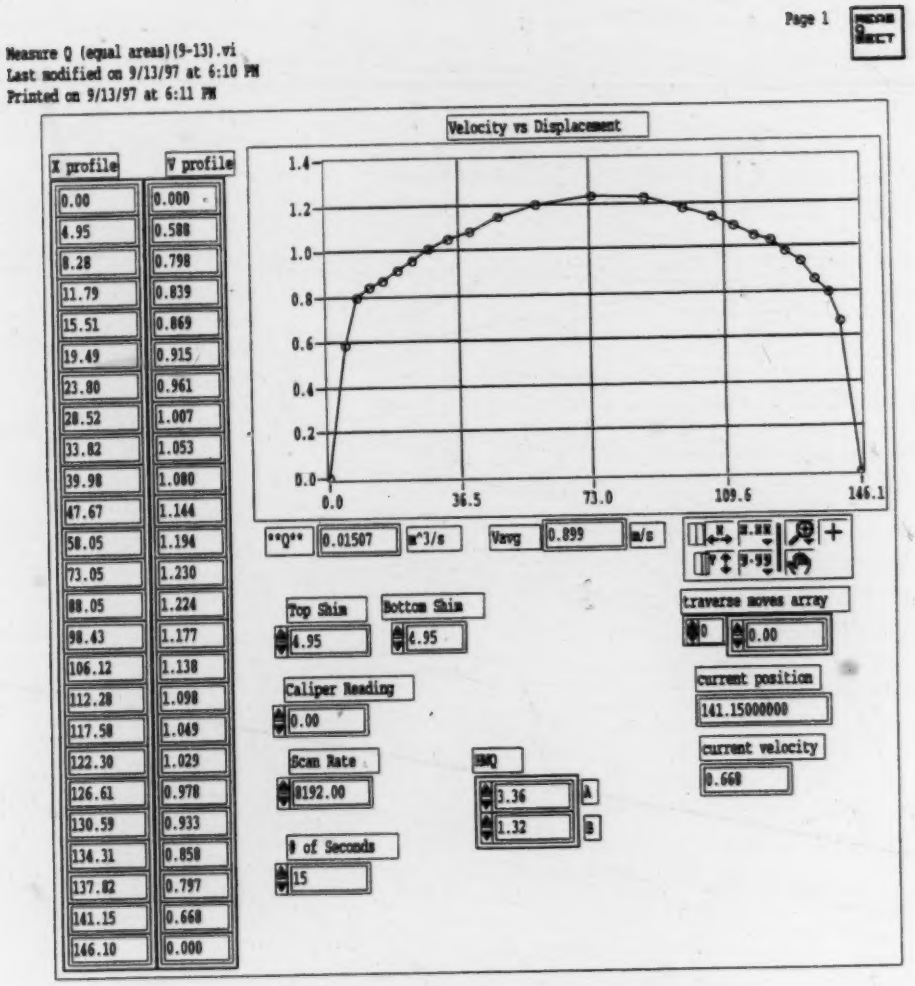

Figure 3.21: Typical Velocity Profile

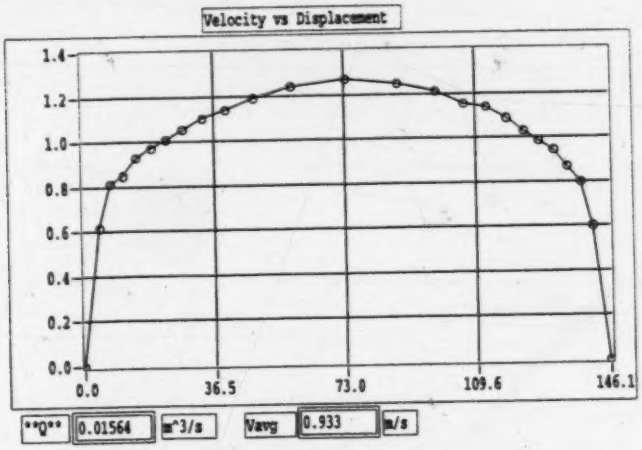

Figure 3.22: Symmetric Velocity Profile

the pipe and tends to make the profile fuller thereby further increasing the overall average velocity. Instances where this rectification occurred showed a significant increase in flow rate where less than a 4% increase in flow had occurred, as explained above. Some measurements were taken after the error in the computer code was corrected. They showed an increase in Q of 22% at a frequency with a lot of rectification in the HWQ signal, but an increase in Q of only 0.2% at a frequency that had no rectification. The two cases had the same increase in pressure drop across the orifice plate, approximately double. This measurement is the third measurement mentioned earlier that supports the assumption that Q is constant.

3.5.5 Effect of Acoustic Node Position

The tests were done using the velocity level of pulsation as a constant for each run. For some frequencies, a velocity antinode ended up at the orifice plate giving the maximum velocity pulsation and minimum pressure pulsation there. The case at 60Hz is an example of this, while the case at 46.5 Hz does not have the velocity antinode at the orifice plate. Table 3.2 provides the levels of pulsation (measured by the NNP) for both cases along with the resulting ΔC_D. These two cases have velocity pulsation levels and ΔC_D that are equal, but their pressure pulsation levels differ by a factor of six. If the pressure pulsation level was having an effect, the ΔC_D would be expected to vary between the two. This supports the idea that it is the velocity pulsation that is the relevant parameter, but does not prove it. As the frequencies are not identical, it may be having an effect that clouds the issue. A better test must be done to determine this conclusively.

Table 3.2: Pulsation Level Comparison

f_p	pressure pulsation level	velocity pulsation level	ΔC_D
46.5 Hz	~100 Pa	1.4 m/s	-30%
60 Hz	~600 Pa	1.4 m/s	-30%

Re = 9,000, $\frac{u'}{U_o}$ =25%, for more data on these two cases, look at 24R2N03 and 24R2N08 in Appendix D

3.5.6 Comparison With $\beta = 0.65$

The 0.5 β orifice plate was replaced by a 0.65 β orifice plate. Tests were repeated at the same absolute pulsation level as the 1m/s 25% pulsation runs, which resulted in a pulsation level of 35% since the increase in velocity through the vena contracta is less. The effect on C_D is roughly the same as seen in Figure 3.12.

Figure 3.23 shows a photograph with this OP at a St_{sh} of 0.27, a St_j of 0.54. The expected wavelength is 67 mm. The ΔC_D scales well with the other tests, and no significant difference was seen at this beta ratio. At higher beta ratios, the shedding instability would be expected to dominate, and the jet instability may not even be present.

Here ends the discussion on the results from visualization studies on effects of pulsation on an orifice plate flow meter. The conclusions of the results given in this chapter plus a discussion of potential future work are discussed in Chapter 4.

Figure 3.23: Photograph With $\beta = 0.65$:
Re=9,000, $St_{sh} = 0.12$, $St_j = 0.45$, $\frac{u'}{U_v} = 37\%$, $\Delta C_D = -34\%$

Chapter 4

Conclusions and Future Work

4.1 Conclusions

A complex apparatus was designed and built that is capable of measuring the effect of pulsation on the discharge coefficient of an orifice plate flow meter. Preliminary tests in a wind tunnel were used to test and refine experimental techniques. These were then applied to the design of the test rig that was built exclusively to study the role that large scale vortex structures have in pulsation induced orifice plate flow metering error. The rig used a computer to control the automatic flow rate measurement, taking of photographs, and acquisition of: acoustic data, the pressure drop across the orifice plate, and other velocity and pressure data. It is the first instrument to combine these measurements with flow visualization. An unusual aspect of the design was that control of the amplitude of pulsation independent of flow rate was possible. This allowed pulsation with zero flow rate. Experiments were performed which led to the conclusions that follow.

Three turbulent instabilities which have been identified in other flows, are present in orifice plate flow meters. These are the:

- Kelvin-Helmholtz instability,
- jet instability, and
- shedding instability.

Both the jet and shedding instabilities have been linked to a significant reduction in the discharge coefficient, while forcing at the higher frequencies amplified by the Kelvin-Helmholtz instability has much less of an effect.

Two other instabilities which are not as well understood may also play a weaker role in pulsation induced metering error. These are expected to be associated with the:

- pipe turbulence, and the
- corner separation bubble.

There are no photographs that show a visible effect on these, but the present visualization technique may not show the pipe instability. The corner separation bubble is expected to respond in some manner if forced at frequencies outside the range tested.

Pulsation at the frequency regimes corresponding to the first three instabilities can influence the flow resulting in significant metering error, to varying degrees depending on which instability is being forced. The maximum measured change in the discharge coefficient with pulsation was -30% for the 0.5 beta ratio orifice plate (-35% for the 0.65 beta ratio) at pulsation velocity amplitudes of 25% and 35% respectively. Put another way, the *indi-*

cated flow rate would be 40% greater than the actual flow rate. This occurred for non-dimensional frequencies of pulsation of 0.2 to 0.5. The error occurred in a broad band of frequencies reaching to higher values, the range broadening as pulsation amplitude increased. This is very similar to the range found in forcing the separation bubble on a blunt-faced cylinder aligned coaxially with the free-stream (Sigurdson, 1995). Within this range, the effect on the discharge coefficient was linear with pulsation velocity amplitude, and on initial inspection, apparently independent of pressure amplitude. Forcing at non-dimensional frequencies three times higher than those causing maximum meter error were seen to cause a small *increase* in discharge coefficient, 2.5% to 8% at very high amplitudes of forcing. This would *underpredict* the actual flow rate. The frequency range where this happens seemed to be quite narrow and needs further study to define more clearly.

This frequency dependence is a new concept as Jungowski et al. (1990) concluded that it did not matter. Only the pulsation pressure amplitude was thought to matter. We suggest that this was because previously the frequencies studied were so low relative to the naturally occurring frequencies in the turbulence that there was no effective coupling with it. Other previous research was unable to correlate pulsation effects to the frequency nor understand why some frequencies of pulsation had a greater effect on the discharge coefficient than others.

A mechanism for pulsation induced flow meter error has been proposed that is based on a change in behaviour of the flow due to a modification

of the vortices in the flow when forced at the right frequency. Pulsation within the frequency regime associated with the flow instabilities results in larger vortices occurring closer to the orifice plate, a consequent narrowing of the vena contracta, and an increase in the pressure drop for the same flow rate. This causes a reduction in the effective discharge co-efficient from its calibrated value. The result is meter error. An explanation of how to avoid this frequency regime has been developed and is included in Appendix C. The goal of this appendix is to facilitate applying the results of the thesis without necessarily spending the time to understand all the details. Section C.2 proposes a correction methodology that may be used to predict roughly the amount of error to expect at a given pulsation level within the dangerous frequency regime.

These results are in agreement with qualitative wind tunnel experiments where the three main instabilities were also seen to exist and be influenced by pulsation.

In general, the change in the discharge coefficient was negative, but in at least one case at higher frequencies, the change in the discharge coefficient was positive. This appears to be from a suppressing of pairing in the shear layer for a portion of its streamwise extent, slowing the growth of the shear layer, and actually widening the vena contracta.

At one frequency with the largest pulsation level, reversed flow was observed around the edges of the orifice plate. This "burping" and "re-swallowing" of the turbulent flow appears to be associated with the largest recorded error

in the discharge coefficient.

The 9% pulsation level data at two different velocities indicates that, in the frequency regime of maximum pulsation effect, the Re is not important. Also, this matching of the 9% pulsation level data along with all the rest of the data taken at three different velocities indicates that the Strouhal number scaling idea is correct.

The upstream pipe turbulence does not destroy the shear layer instability appearance, comparing it to the case where there is a uniform, steady upstream flow in the wind tunnel.

There is little curvature in the separated shear layer of the vena contracta as compared to the curvature in the separation bubble on a blunt-faced cylinder aligned coaxially with the free-stream (Sigurdson, 1995). This could be due to the enclosed nature of the flow or the presence of the upstream corner separation bubble which smooths out the flow.

Within the frequency range close to the jet and shedding instabilities, the effect on the discharge coefficient is linear with pulsation level.

These instabilities were observed at Reynolds numbers from ~10,000 to ~50,000. The effect on the discharge coefficient occurred throughout this range of Re and is expected to exist no matter how high the Re gets. This relative insensitivity to Re is due to the fixed location of the separation at the orifice lip.

There is sometimes a noticeable pressure drop across the orifice plate even when no flow is present. This could cause considerable error in the flowrate

when high levels of pulsation occur with a low flow rate. This may be caused by acoustic streaming.

4.2 Future Work

To build on the work done in this project, the following analysis and experiments could be done:

- Analyze the current data more completely, for example, the turbulence intensity results.
- Widen the frequency range to verify that the effect drops off at high frequencies, and refine the knowledge of the frequency regime where it can possibly change sign.
- Run tests at carefully selected frequencies to confirm the relative importance of pulsation velocity amplitude over pressure amplitude (frequencies close to each other that have contrasting values).
- Experimentation in full scale facilities to confirm that the same type of meter error occurs there.
- Study the effect we think is caused by acoustic streaming.
- Make some sense out of the pipe acoustic resonances found.
- Investigate the effect of the presence or the absence of the orifice plate on the acoustics.
- Analyse the pipe pulsation profiles both with/without orifice plates to determine if the profile changes.
- Design and perform some experiments to characterize the pipe insta-

bility.

- Place the smoke wire in the close to orifice upstream position to study the size of the corner separation bubble, and locate the frequency at which it is affected.
- Take a photograph of a grid in the test section to check for visual distortion due to curvature of test section and imperfections in it.
- Make further measurements to substantiate whether the pressure upstream of the orifice plate remains constant with or without pulsation.
- Take hot wire profiles and locate the vena contracta both with and without pulsation. This would provide more information on the variation in the vena contracta. Particle Image Velocimetry (PIV) would be useful for this.

BIBLIOGRAPHY

Botros, K., Jungowski, W., Studzinski, W., and Szabo, J. (1986). Pressure pulsations at orifice plates and general pipeline flow - acoustic simulator. *1986 International Gas Research Conference*, pages 243–256.

Brown, G. and Roshko, A. (1974). On density effects and large structure in turbulent mixing layers. *Journal of Fluid Mechanics*, 64:775–816.

Corke, T., Koga, D., Drubka, R., and Nagib, H. (1977). A new technique for introducing controlled sheets of smoke streaklines in wind tunnels. *ICIASF '77 Record, IEEE Publication*, pages 74–80.

Crow, S. and Champagne, F. (1971). Orderly structure in jet turbulence. *Journal of Fluid Mechanics*, 48:151–159.

E.H. Jones Jr, R. B. (1991). A numerical analysis of pulsating laminar flow through a pipe orifice. *Transactions of the ASME; Journal of Fluids Engineering*, 113:199–205.

Fox, R. W. and McDonald, A. T. (1992). *Introduction to Fluid Mechanics*. John Wiley & Sons Inc., New York, 4th edition.

Freitas, C. (1995). Advanced computational simulation of flow phenomena associated with orifice meters. *Fluid Flow Measurement 3rd International Symposium.*

Gajan, P., Millan, P., Hebrard, P., and Trichet, P. (1989). Investigation of the flow patterns through an orifice plate flowmeter. *5th International IMEKO-Conference on Flow Measurement Flomeko*, pages 279–286.

Gajan, P., Mottram, R., Hebrard, P., Andriamihafy, H., and Platet, B. (1992). The influence of pulsating flows on orifice plate flowmeters. *Flow Measurement and Instrumentation*, 3(3):118–129.

Grimson, J. and Hay, N. (1971). Errors due to pulsation in orifice meters. *The Aeronautical Journal of the Royal Aeronautical Society*, 75:284–287.

Hebrard, P., Biscos, Y., Gajan, P., and Platet, B. (1985). An investigation of the behaviour of orifice meter in pulsating flow conditions. *International Conference on Flow Measurement - IMEKO*, pages 223–230.

Hebrard, P., Malard, L., and Strzelecki, A. (1992). Experimental study of a vortex flowmeter in pulsatile flow conditions. *Flow Measurement and Instrumentation*, 3(3):173–186.

Jungowski, W., Studzinski, W., and Szabo, J. (1990). Orifice meter performance under pulsating flow conditions. *Internal Report for NRTC (NOVA Research and Technology Corporation).*

Karnik, U., Jungowski, W., and Botros, K. (1994). Effect of turbulence on orifice meter performance. *Transactions of the ASME: Journal of Offshore Mechanics and Arctic Engineering*, 116:77–85.

Kathuriya, M. and Munjal, M. (1979). Experimental evaluation of the aeroacoustic characteristics of a source of pulsating gas flow. *J. Acoust. Soc. Am.*, 65(1):240–248.

Lebedeva, I. (1980). Experimental study of acoustic streaming in the vicinity of orifices. *Sov. Phys. Acoust.*, 26(4):331–333.

Michalke, A. (1964). The influence of the vorticity distribution on the inviscid instability of a free shear layer. *Fluid Dynamics Transactions*, 4:751–760.

Mottram, R. (1974). The measurement of pulsating flow using orifice plate meters. *Flow; Its Measurement and Control in Science and Industry*, 1:197–208.

Mottram, R. (1981). Measuring pulsating flow with a differential pressure meter. *Flow; Its Measurement and Control in Science and Industry*, 2:347–361.

Mottram, R. (1992). An overview of pulsating flow measurement. *Flow Measurement and Instrumentation*, 3(3):114–117.

Oster, D. and Wygnanski, I. (1982). The forced mixing layer between parallel streams. *Journal of Fluid Mechanics*, 123:91–130.

Roshko, A. (1976). Structure of turbulent shear flows: A new look. *AIAA Journal*, 10(14):124–131.

Schlicting, H. (1979). *Boundary Layer Theory*. McGraw Hill, 7th edition.

Shi, Z., Lee, T., and Winoto, S. (1994). A numerical study of pulsatile laminar flows in a pipe with a ring-type constriction. *International Journal for Numerical Methods in Fluids*, 20:289–305.

Sigurdson, L. (1987). The three-dimensional vortex structure of the starting vortex ring. *Bull. Am. Phys. Soc.*, 32(10):2095.

Sigurdson, L. (1991). Gallery of fluid motion: Atom bomb/water drop. *Physics of Fluids A*, 3(9):2034.

Sigurdson, L. (1995). The structure and control of a turbulent reattaching flow. *J. Fluid Mech.*, 298:139–165.

Sigurdson, L. (1997). Flow visualization in turbulent large-scale structure research. *Atlas of Visualization*, 3. edited by the Visualization Society of Japan, CRC Press.

White, F. (1986). *Fluid Mechanics*. McGraw-Hill Inc., New York, 2nd edition.

Winant, C. and Browand, F. (1974). Vortex pairing: the mechanism of turbulent mixing-layer growth at moderate reynolds numbers. *Journal of Fluid Mechanics*, 63:237–255.

Appendix A

Smoke Wire Development

Smoke-Wire Flow Visualization Device

by
Mr. Ashok Mohanty, 3rd year undergraduate student,
Mechanical Engineering Department, U of A

I was involved in this project for the NOVA Corporation as an undergraduate recipient of a Dean's Research Award. My work entailed designing a vertical smoke-wire that would be used in a simulation of a gas pipeline. The purpose of a smoke-wire is to introduce a controlled sheet of smoke into a wind tunnel. This is achieved by dropping oil down a thin wire which runs vertically across the center of the wind tunnel. The oil is burned off to create discrete streaklines by resistively heating the wire by passing a current through it. Streaklines provide a valuable means of visualizing the flow inside a wind tunnel.

The device was designed to ensure good electrical pathways, along with ease of use and versatility as our other directives. The device used in our application rests on top of a 6 in. diameter pipe (the wind tunnel in our application) and consists of two parts: the oil reservoir, and its stand-off. The function of the stand-off is to support the oil reservoir on top of the pipe. It is made from a cylindrical acrylic rod with a partial bored-out section to seat the reservoir, and a hole for the needle to be passed through it into the pipe. A radius of 3 in. has been machined into the bottom of the rod so that the stand-off can "saddle" the pipe. The dimensions of the stand-off were chosen so that the tip of the needle would intrude no more than 1/8 in. into the inner surface of the pipe.

The more intricate component is the oil reservoir. Its function is to hold oil, retain pressurized air, as well as provide electrical contact from the power source to the wire. The oil reservoir consists of a bored plastic cylinder of 2 in. diameter, as shown in the attached drawing, as well as a matching threaded cap which is removable for maintenance. In order to retain pressure within the reservoir, a rubber o-ring has been added to the cap. The pressurized air, created by a simple hand bulb, will enter the reservoir through a steel tube that passes through the cap. It is this additional pressure that forces the oil out of the needle. On the bottom end of

the reservoir is a press-fit brass bushing . This bushing houses the needle, a stainless steel tube characterized by an i.d. twice as large as the o.d. of the wire. This ratio produces minute droplets that adhere to the wire for speeds of up to 6 m/s. Also, these dimensions require a minimal pressure for forcing the oil out of the end, which can be easily achieved using a hand-type bulb.

Power is supplied to the smoke-wire by an external power source. The power is transferred by another wire which extends from the brass bushing to the outside of the reservoir. Thus the brass bushing conducts power through to the needle and on to the smoke-wire. The top entrance of the bushing has been rounded for several reasons: to provide more length of smoke-wire to be in contact with the electrically charged bushing, and to eliminate any possible kinks in the smoke-wire. The ground of the power source will be joined to the other end of the smoke-wire at the bottom of the pipe.

Alterations to the pipe include drilling two small holes at the top and bottom of the pipe. The end of the needle enters the top hole and the wire is fed through the reservoir, the needle, the pipe and finally exits through the hole at the bottom. The wire is secured at both ends and is hose-clamped on its upper end as it bends over the top of the cap's pipe (refer to attached diagram). A weight is attached to the other end of the wire at the bottom of the pipe. The weight provides the necessary tension in the wire, maintaining its stability in the flow.

Work Cited

T. Corke, D.Koga et al. A New Technique for Introducing Controlled Sheets of Smoke Streaklines in Wind Tunnels 1977: 74-80

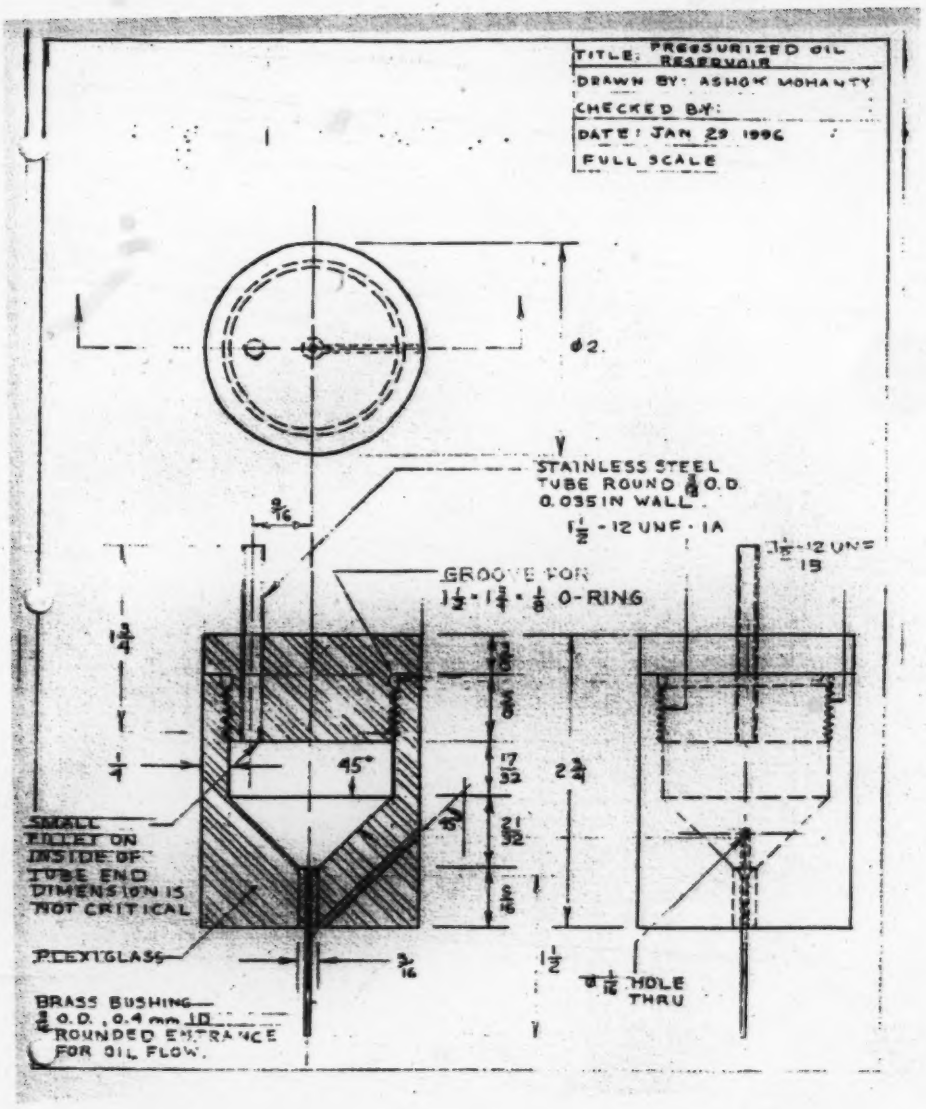
TITLE: PRESSURIZED OIL RESERVOIR
DRAWN BY: ASHOK MOHANTY
CHECKED BY:
DATE: JAN 29 1996
FULL SCALE
STAINLESS STEEL TUBE ROUND 3/8 O.D 0.035 IN WALL
1 1/2 - 12 UNF - 1A
GROOVE FOR 1 1/2 - 1 3/4 - 1/8 O-RING
45°
SMALL FILLET ON INSIDE OF TUBE END DIMENSION IS NOT CRITICAL
PLEXIGLASS
BRASS BUSHING 3/8 O.D., 0.4 mm ID ROUNDED ENTRANCE FOR OIL FLOW.
HOLE THRU

Figure A.1: Smoke Wire Reservoir Drawing: Reduced to Fit Page

APPENDIX B

LABVIEW® PROGRAMS

A short description of some of the most important programs ("vi" stands for virtual instrument) used in running the experiments and processing the data has been included here. They are *main6-1.vi, Data to spreadsheet.vi, nnp prep.vi, nnp2.vi, pipematrix.vi, Measure Q (equal areas)(9-13).vi, Concentric Cylinder Q.vi, traverse return to home.vi, and traverse control with no encoder.vi.* The information printed for each program includes the program description and the front panel appearance.

B.1 Description of *main6-1.vi*

This is the Main Program used to run experiments on pulsation induced orifice plate flow metering error. This program reads data from 11 transducers, can record this data, display useful information from the data as well as the raw data itself. This program also controls the traverse and calculates the flow rate, and sends the start signal to the timer for photographs.

Basic operation: Start program, then change any necessary information in the configuration page. Then, unless the bypass calibrate button is up, the computer will self-calibrate the data-acquisition board. Then opportunity to adjust HWQ position, and calbrate HWQ and HWT is given. Then enter the filename for data to be stored in (even if you are not planning on saving any data, just enter something like c:/data/scratch.dat)

Then the computer will start calculating and displaying data using the # of scans set in the top left corner of the screen. This information is diplayed in the data graph as voltage values unless the convert data switch is up, then it will be in m/s and decapascals. A spectrum and an average of each of the channels is available at the bottom right of the screen. Select the appropriate transducer by name in the top of the 7 ring controls seen there. The other ring controls set things for the spectrum (some don't work. best to use current settings) There is a toggle switch to turn the spectrum on and off. The average is always displayed. Also available is a graph of the NNP output when switch is up. The velocity value at the orifice plate is given

to the right, and the desired value to achieve a certain portion of the HWT velocity is displayed. Enter the appropriate portion in the puls. level control.

When a Q (flow rate measurement), photo, or data record is desired, choose any or all of these that you want, and then press the Do a RUN button. This will then do one acquisition of the data along with what you requested, and then go back to normal data display as before. After the first data record is taken the computer will ask for the configuration file name for this data set. The Spectrum, NNP, and Convert Data switches work all the time. The Q, take photo, and record data switches will only do anything when the Do a RUN button is pressed.

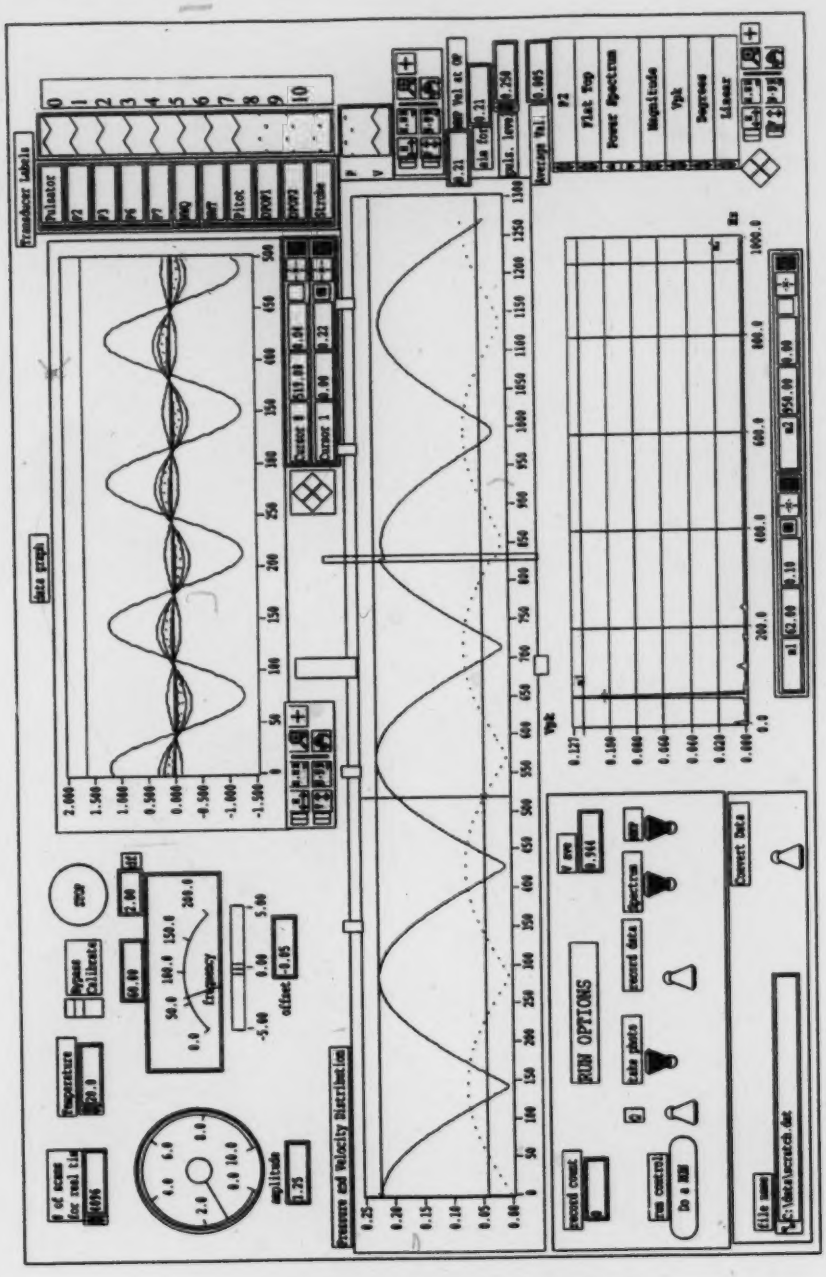

Figure B.1: Front Panel of *main6-1.vi*

B.2 Description of *Data to spreadsheet.vi*

This is the vi that is used to retrieve the data taken by main6. The data is displayed in a similar manner to how it was shown while being recorded. In addition, a summary screen is provided which can be printed out, and summary information is also sent to a spreadsheet file so all pertinent data can be processed for the whole run.

Before running the vi, be sure to fill in the negative number for the photograph taken that corresponds to each record numbers. Record number zero is left at zero, then enter the appropriate negative number for the photograph taken with each record number. If no photo was taken for a particular record, enter 99. Make sure the toggle switch for printing is down unless you do want to print out the summary sheet for each record. The program will go through each record sequentially until it gets to the largest record number that you've entered a negative number for. If you leave any record numbers blank before that, they will still be retrieved and assigned a negative number of zero.

Then run the vi, and when prompted, enter the appropriate data file and configuration file names and the spreadsheet file name for the summary data to be written to. Then be patient. It takes at least 20 seconds for LabVIEW® to extract the data from each record and display it. When done viewing that record, hit the next record button and wait for the next record. You can adjust the limits on the graphs if you want to look at a certain area more closely before moving onto the next record.

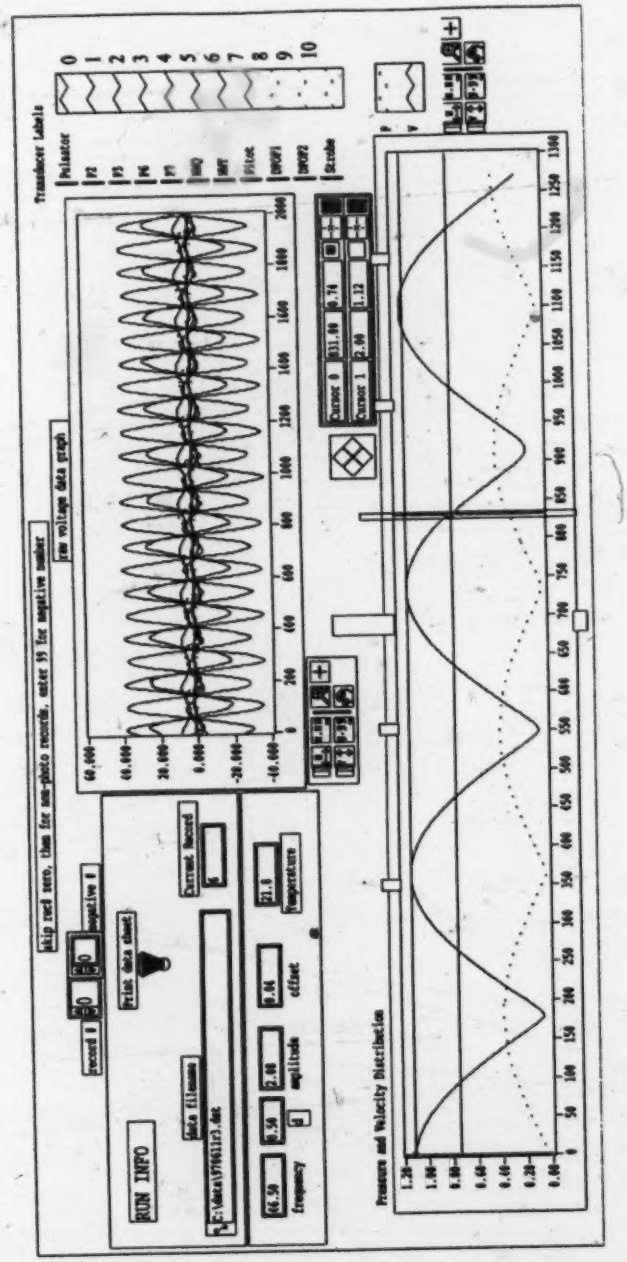

Figure B.2: Front Panel of *Data to spreadsheet.vi*

B.3 Description of *nnp prep.vi*

This vi takes the raw signals from the pressure transducers and calculates the appropriate phases and amplitudes and passes these to the NNP calculation vi along with some other necessary info. The calculated amplitude and phase arrays are then given back to the main program.

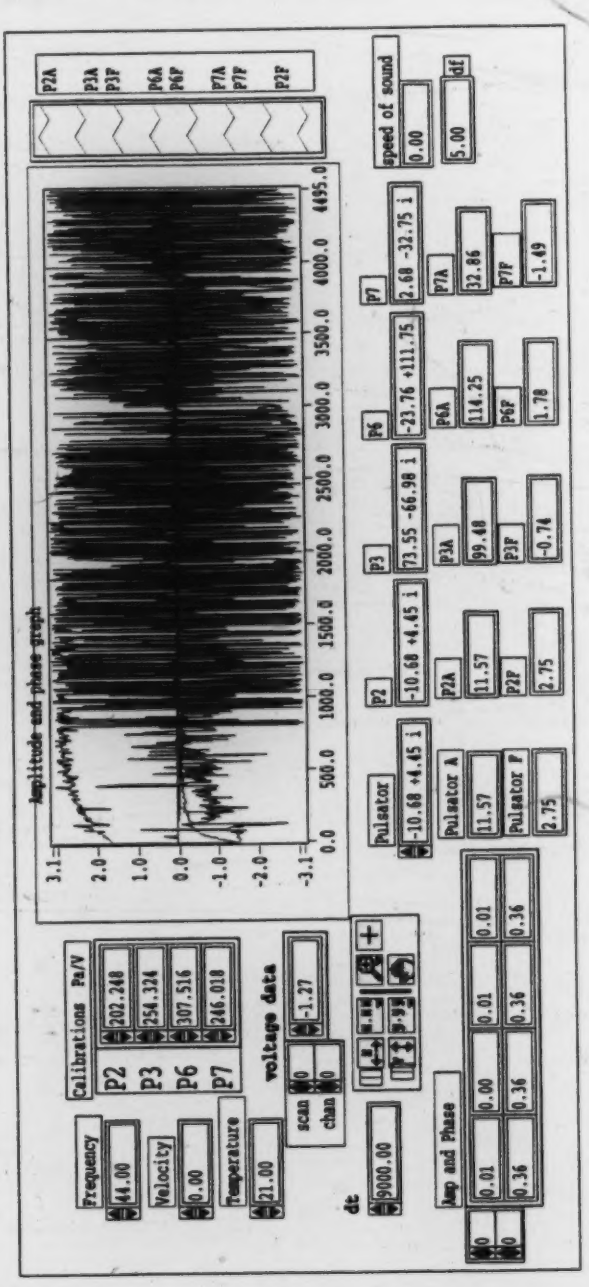

Figure B.3: Front Panel of *nnp prep.vi*

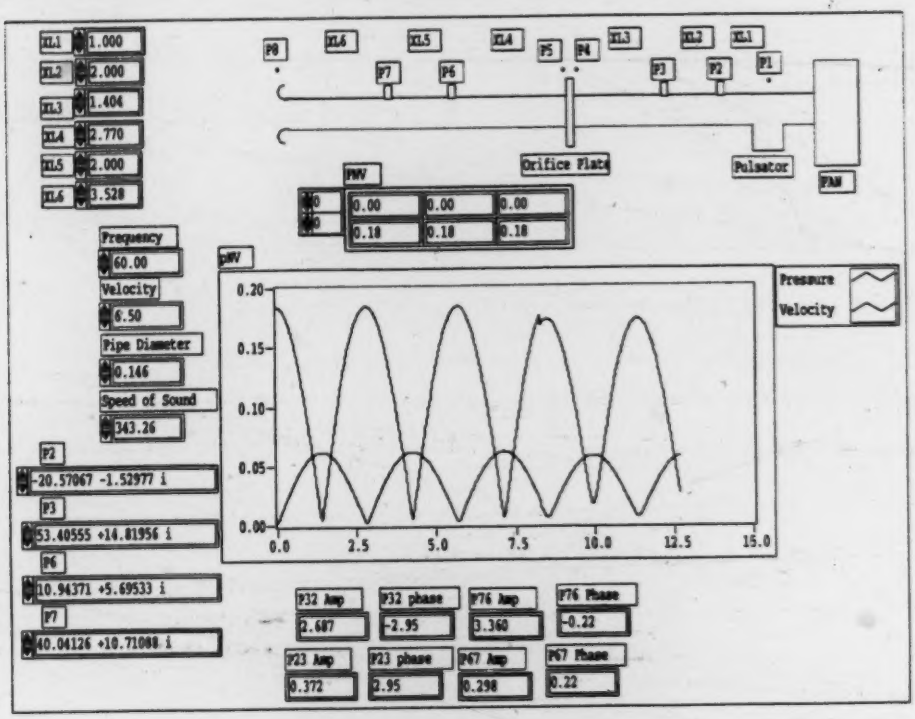

Figure B.4: Front Panel of *nnp2.vi*

B.4 Description of *nnp2.vi*

This vi takes the phase and amplitude info and calculates the pressure and velocity distribution in the pipe. Pressure is in decapascals, and velocity in m/s. This was modified slightly from the NOVA Node Program received in FORTRAN.

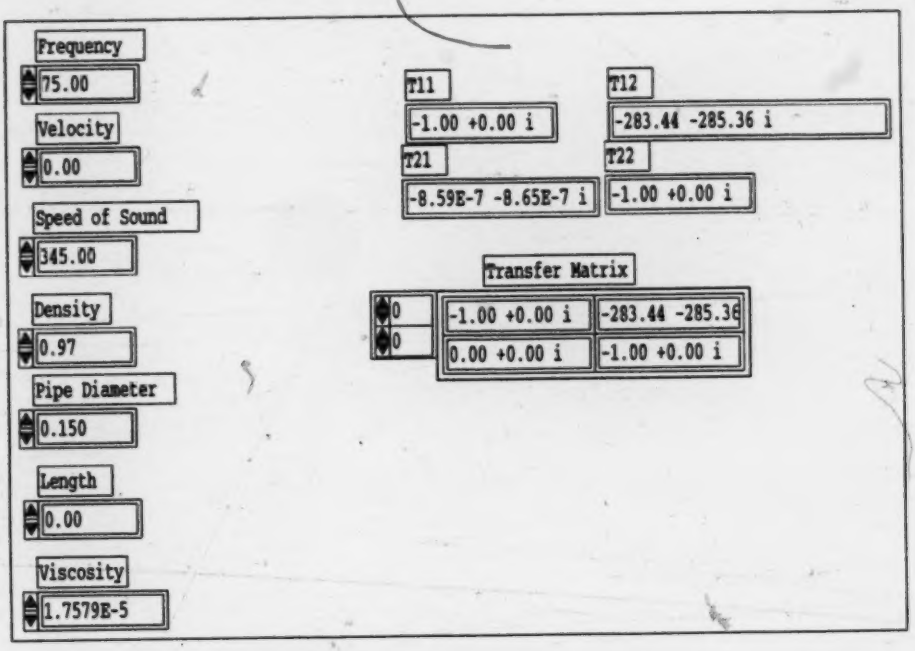

Figure B.5: Front Panel of *pipematrix.vi*

B.5 Description of *pipematrix.vi*

This is the subroutine used by the NNP program used in calculating the pressure and velocity amplitude distribution in the pipe.

B.6 Description of *Measure Q (equal areas)(9-13).vi*

Measure Q (4-03) is a subVI that measures the volume flow rate in the Q section of the apparatus. This VI controls both the hotwire traverse as well as the hotwire. Upon being launched, the VI returns the hot wire to the "home" or registered start position and then executes a series of steps and measurements. This series of steps generates a velocity profile across the diameter of the test section as well as a displacement array. The profile and array are then used to calculate a Q flow rate as well as an average velocity. Next, the VI returns the traverse to the middle of the pipe to monitor velocity there.

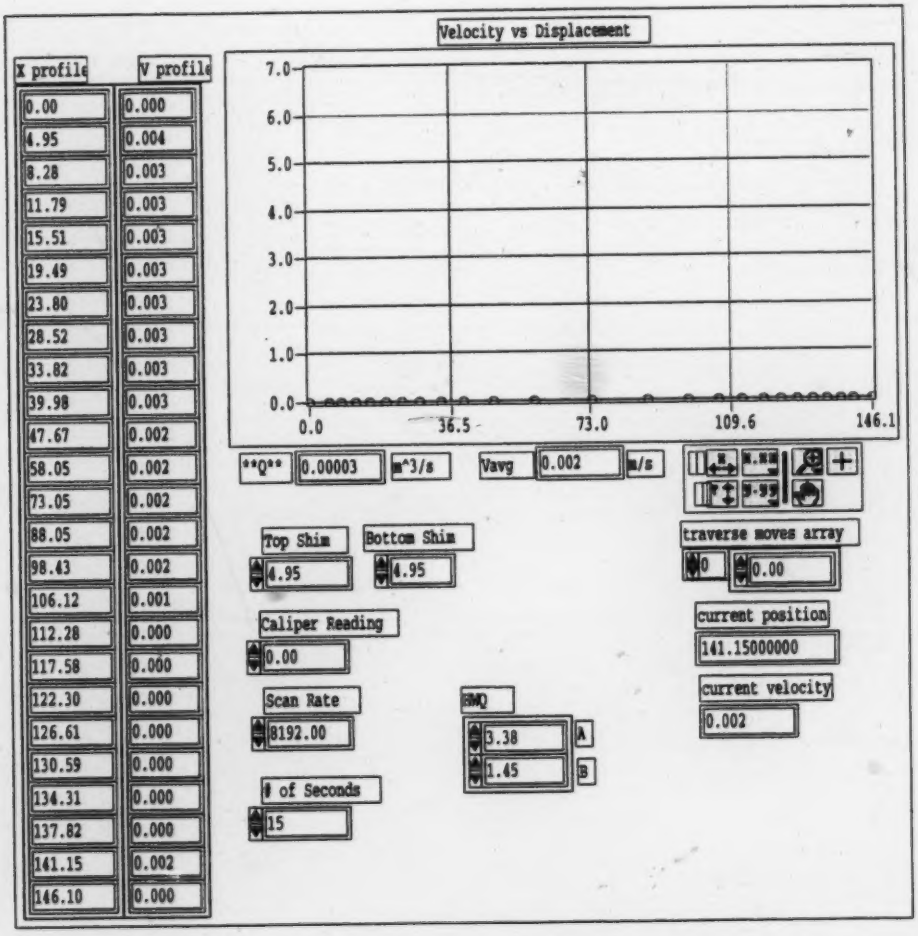

Figure B.6: Front Panel of *Measure Q (equal areas)(9-13).vi*

B.7 Description of *Concentric Cylinder Q.vi*

Concentric Cylinder Q is a subVI that uses a method of volume of concentric cylinders to translate a velocity profile into a volume flow rate. The inputs include the velocity profile as well as the displacements between each reading. The output is the calculated Q value.

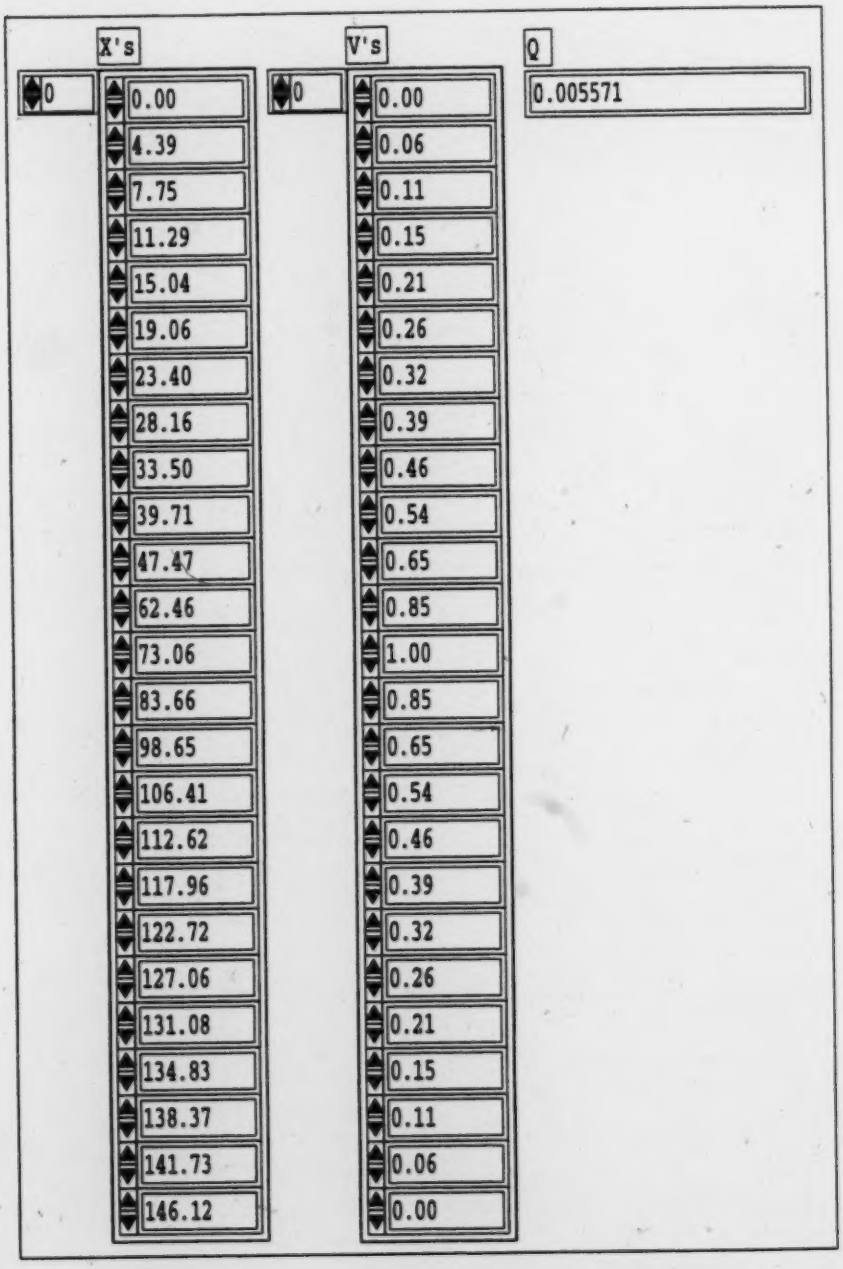

Figure B.7: Front Panel of *Concentric Cylinder Q.vi*

B.8 Description of *traverse return to home.vi*

Traverse return to home is a subVI that returns the traverse to the zero position. The traverse is moved upward towards the top of the Q section pipe until the zeroing switch makes contact. Then the traverse is moved slightly further upward, past the zero position. The traverse then switches direction and slowly moves back down taking slow, small steps until the zeroing switch stops making contact. This back and forth motion is to remove any backlash that may occur with use of the traverse. The point at which the traverse stops making contact with the zero switch is considered as the zero or reference point.

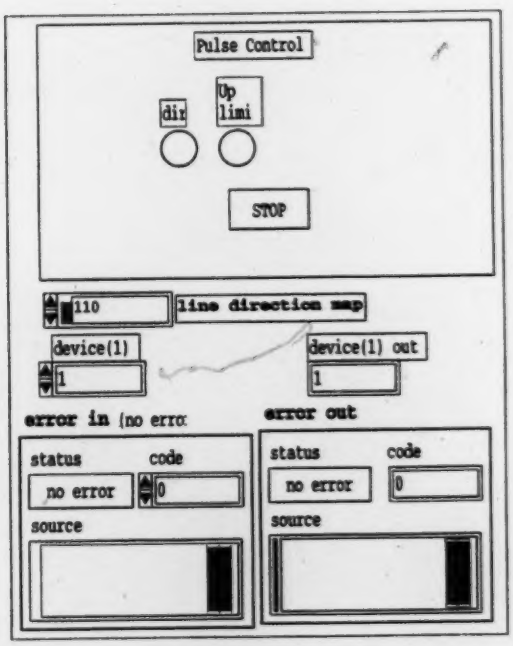

Figure B.8: Front Panel of *traverse return to home.vi*

B.9 Description of *traverse control with no encoder.vi*

Traverse control with no encoder is a subVI that is used to move the HWQ traverse. When running, the VI watches to make sure that neither of the limit switches installed on the traverse are met. The limit switches stop the traverse from running the anemometer into the wall of the test section. The inputs include the direction to move and the distance to move.

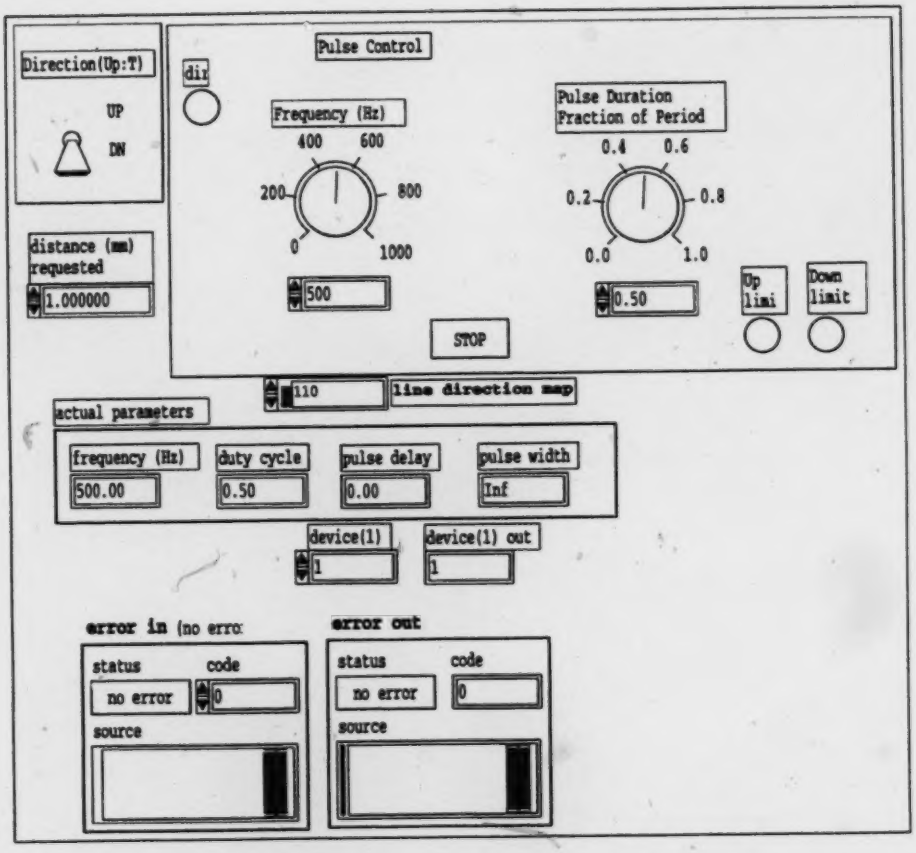

Figure B.9: Front Panel of *traverse control with no encoder.vi*

Appendix C

Relevance of these Results to Orifice Plate Installation Design

The important aspect of these results is that meter error is dependent on the pulsation frequency. This appendix explains how to find the dangerous frequency ranges and includes possible ways to avoid that frequency. It also includes a possible correction methodology. The goal is to be able to refer to this appendix and be able to apply the results of this thesis without necessarily spending the time to understand all the details.

C.1 Determining Dangerous Frequency Regimes

It was found that large metering error can result if the pulsation frequency is within a frequency range at which certain turbulent instabilities are afffected. Two instabilities that have the greatest effect are the jet instability and the shedding instability. In this experiment with $\beta = 0.5$ we could not easily divide their respective effects and therefore we can only be certain of the

following dangerous frequency ranges specific to this beta ratio. We expect these will also be dangerous for other ratios; the jet instability becoming more important as β's become much less than 0.5, and the shedding instability becoming more important as β becomes much greater than 0.5.

For definitions of terms needed to better understand this appendix, refer to Section 1.2.

The jet instability occurs generally at $St_j = 0.3$. Therefore, from the equations $St_j = \frac{f_p D_v}{U_v}$, and $Q = U_v(\frac{\pi D_v^2}{4})$, it can be shown that:

$$f_{p_j} = \frac{0.38Q}{D_v^3} \tag{C.1}$$

Then if we make the approximation that $D_v = d$, and knowing that $\beta = \frac{d}{D}$, then

$$f_{p_j} = \frac{0.38Q}{D^3\beta^3} \tag{C.2}$$

For the shedding instability, $St_{sh} = 0.08$, but it responds best when forced at two to four times this frequency, or $St_{sh} = 0.24$ if we use the middle of this range. (This was found previously (Sigurdson, 1995) and is in approximate agreement with the results found here.) Therefore, from the equations $St_{sh} = \frac{f_p H_v}{U_v}$, $Q = U_v(\frac{\pi D_v^2}{4})$, and $H_v = \frac{D-D_v}{2}$, it can be shown that:

$$f_{p_{sh}} = \frac{0.61Q}{(D - D_v)D_v^2} \tag{C.3}$$

Again, if the approximation that $D_v = d$ is made, and knowing that $\beta = \frac{d}{D}$, then

$$f_{push} = \frac{0.61Q}{\beta^2(1-\beta)D^3} \tag{C.4}$$

The pulsation frequency should not be near either of these frequencies, or significant metering error could result if velocity pulsation amplitudes are significant near the orifice plate. (See Section C.2 for a quick way to estimate whether the amplitudes can give significant error. The "rule of thumb" is the same percentage reduction in C_D as the percentage of pulsation amplitude.) This could be avoided by adjusting the pulsation frequency. This may not always be possible, but there are three other variables that can be adjusted to move the dangerous flow response frequency farther away from the imposed pulsation frequency. The flow rate can be changed and will have a linear effect on the frequency. The beta ratio and pipe diameter could also be changed with a stronger influence. Altering any of these three variables will move the frequency at which the jet and shedding instabilities occurs. Avoiding these pulsation frequencies will avoid significant error due to vortex modification at that frequency. There can still be error due to acoustic reasons as previously studied (Jungowski et al., 1990).

If pulsation level is very large then an effect that we think may be connected to acoustic streaming may cause some error at many different frequencies. The error due to this is worse at low pipe velocities. At this point, we can only provide a caution about this phenomenon as it was outside the scope of our work. It has not been investigated to determine a more complete

understanding of it.

C.2 Speculation on Regimes for Other Beta Ratios and a Possible Correction Methodology

At the two beta ratios tested, the shedding and jet instabilities occurred at roughly the same frequency. With smaller beta ratios, these would move apart as the step height increases and the orifice diameter decreases. The jet instability would dominate and the shedding instability would be expected to become insignificant. Similarly, as beta ratio increases, the jet instability would lose strength as the shedding instability begins to dominate. Further experiments need to be done with two extreme beta ratios, large and small, to confirm these hypotheses.

Concerning a possible correction methodology for turbulence produced meter error, it is useful to consider the following as an equation for C_D:

$$C_D\Big(\overbrace{Re,\beta,\ldots,}^{\text{usual parameters with no pulsation plus others}}\ \overbrace{\frac{u'}{U_v},\frac{fH_v}{U_v},\frac{fD_v}{U_v}}^{\text{pulsation parameters explored here}}\Big) = \underbrace{C_{D_o}(Re,\beta,\ldots)}_{\substack{\text{usual } C_{D_o}\\ \text{obtained in}\\ \text{the usual way}}}\Big[1+\underbrace{\frac{\Delta C_D}{C_{D_o}}\Big(\beta,\frac{u'}{U_v},\frac{fH_v}{U_v},\frac{fD_v}{U_v}\Big)}_{\text{correction factor}}\Big] \tag{C.5}$$

This is really just:

$$C_D = C_{D_o}[1+\frac{\Delta C_D}{C_{D_o}}], \tag{C.6}$$

but with the independent parameters that things are a function of indicated in parentheses. C_{D_o} is the usual C_D found in the usual way, and $\frac{\Delta C_D}{C_{D_o}}$ is the correction factor that needs to be found through a combination of experiments and theory. (Note: In this section, ΔC_D refers to $\left(C_{D_{\text{with pulsation}}} - C_{D_o}\right)$ which is different from the definition of ΔC_D in the Nomenclature. Of course, U_v could be approximated by knowing U_{pipe} and β by continuity: $U_v = \frac{U_{pipe}}{\beta^2}$.)

On the simplest level, a set of look-up tables (manually or by computer) could be generate experimentally to determine the correction factor. The data might also be simplified to an analytical expression derived by curve fitting the data. On a deeper level, a theory based on the mechanism of error presented here may be able to generate the equations for the correction factor. This would connect the growth rates of the various vortex structures to the narrowing of the vena contracta. Computer simulations using discrete vortices could also contribute to calculating the correction factor. Two-dimensional simulations of forcing a jet have already qualitatively shown similar behaviour to our experiments.

In any case, at the present time for $\beta = 0.5$, we can provide an equation to estimate the *worst case* correction factor. This would not take into account the Strouhal number dependence but any meter error would be less than this. This type of calculation could be used to very quickly estimate whether pulsation induced error could even *be* a problem. If not, it could be disregarded. If it is a *possibility* then a closer look would be necessary. The

estimate would be done as follows. We know from Figure 3.11 that

$$\left(\frac{\Delta C_D}{C_{D_o}} \times 100\%\right)_{\text{worst case}} = 2\% - 1.15\left(\frac{u'}{U_v}\%\right) \text{for} \frac{u'}{U_v} > 2\%. \qquad \text{(C.7)}$$

(Where the left hand side is just the percentage change in C_D and $\frac{u'}{U_v}\%$ means that the percentage value of $\frac{u'}{U_v}$ is used. For example, when $\frac{u'}{U_v}$ is 30%, substitute in 30.) Therefore:

$$C_{D\text{worst case}} = C_{D_o}\left[1.02 - 1.15\left(\frac{u'}{U_v}\% \div 100\right)\right] \text{for} \frac{u'}{U_v} > 2\%. \qquad \text{(C.8)}$$

As stated before, u' refers to the velocity amplitude at the orifice plate (better) or the maximum in the pipe, whichever is known. The "rule of thumb" is the same percentage reduction in C_D as the percentage of pulsation amplitude.

APPENDIX D

DATA SAMPLE

This appendix provides a table of important calculated values for four different runs:

- 970611
- 970620
- 970624*
- 970703

For the 970620 run, in addition to the table, one photograph and a summary sheet is given for each frequency tested. The heat from the smoke wire had some effect on the HWT readings that were taken with a photograph. Therefore a data record was taken without a photo (no heat from smoke wire) at the same frequency, and the HWT value from this is given in the table (in m/s) for each run.

* Note: There was a malfunction in the HWT during this run and so no HWT values are included for it.

D.1 970611

Table D.1: 970611 Run

Photo #	f_p (Hz)	St_{sh}	St_j	C_D	ΔC_D	$\frac{u'}{6U_{pipe}}$	$\frac{u'}{HWT}$	$HWT_{nophoto}$
11R1N14	8	0.05	0.10	0.53	-1.1%	3.0%	2.9%	6.0
11R1N17	307	1.89	3.78	0.54	-0.8%	2.3%	2.2%	5.9
11R1N24	198.5	1.27	2.53	0.55	2.2%	10.1%	10.0%	5.7
11R1N25	183.5	1.20	2.40	0.55	1.9%	11.2%	11.4%	5.6
11R1N34	157.5	0.99	1.98	0.46*	-15.2%*	13.3%	13.0%	5.8
11R2N02	142.5	0.88	1.76	0.52	-4.2%	14.1%	13.4%	5.9
11R2N10	129.5	0.79	1.59	0.51	-6.0%	13.1%	12.4%	6.0
11R2N14	NoX	0.00	0.00	0.54	0.2%	0.0%	0.0%	5.9
11R2N18	116	0.70	1.41	0.52	-4.1%	11.1%	10.5%	6.0
11R2N22	101.5	0.60	1.21	0.49	-9.3%	13.2%	12.2%	6.1
11R2N31	74.5	0.43	0.86	0.49	-8.5%	10.6%	9.6%	6.3
11R2N35	60	0.35	0.69	0.47	-12.3%	13.4%	12.0%	6.3
11R3N04	46.5	0.27	0.54	0.47	-13.0%	13.1%	11.8%	6.3
11R3N10	33.5	0.20	0.39	0.48	-11.2%	13.0%	11.9%	6.2
11R3N13	20	0.12	0.24	0.47	-13.2%	15.3%	14.1%	6.1
11R3N20	16	0.09	0.19	0.52	-3.0%	7.0%	6.4%	6.2
11R3N24	NoX	0.00	0.00	0.54	0.0%	0.0%	0.0%	6.2

Re = 9,000 U_{pipe} = 0.96 m/s D = 146.1 mm $\beta = 0.5$

*note: DPOP1 differed from DPOP2 by over 60% thus giving an erroneous result. This was caused by f_p being at a resonance of one of the transducer's pressure lines.

D.2 970620

Table D.2: 970620 Run

Photo #	f_p (Hz)	St_{sh}	St_j	C_D	ΔC_D	$\frac{\overline{u'}}{6U_{pipe}}$	$\frac{\overline{u'}}{HWT}$	$HWT_{nophoto}$
20R1N07	13.5	0.04	0.07	0.54	0.0%	1.4%	1.3%	14.0
20R1N15	27	0.07	0.14	0.54	-0.4%	2.8%	2.4%	14.0
20R1N21	39.5	0.10	0.21	0.54	-1.3%	4.4%	3.9%	13.9
20R1N22	46	0.12	0.24	0.54	-1.6%	4.5%	3.9%	13.9
20R1N27	59	0.16	0.31	0.54	-1.5%	4.3%	3.8%	13.9
20R1N32	74.5	0.20	0.39	0.53	-2.2%	4.6%	4.0%	13.8
20R2N04	117	0.31	0.62	0.53	-2.1%	4.5%	3.9%	13.8
20R2N08	144	0.38	0.76	0.53	-2.6%	4.4%	3.9%	13.8
20R2N16	184	0.48	0.97	0.53	-2.8%	4.5%	3.9%	13.9
20R2N19	200	0.52	1.05	0.53	-2.6%	4.5%	3.9%	14.0
20R2N25	225	0.59	1.18	0.53	-2.6%	4.5%	3.9%	14.0
20R2N27	240	0.63	1.26	0.53	-1.6%	4.1%	3.6%	13.9
20R2N35	NoX	0.00	0.00	0.54	0.1%	0.0%	0.0%	14.0

Re = 20,000 U_{pipe} = 2.1 m/s D = 146.1 mm $\beta = 0.5$

Figure D.1: 20R1N07

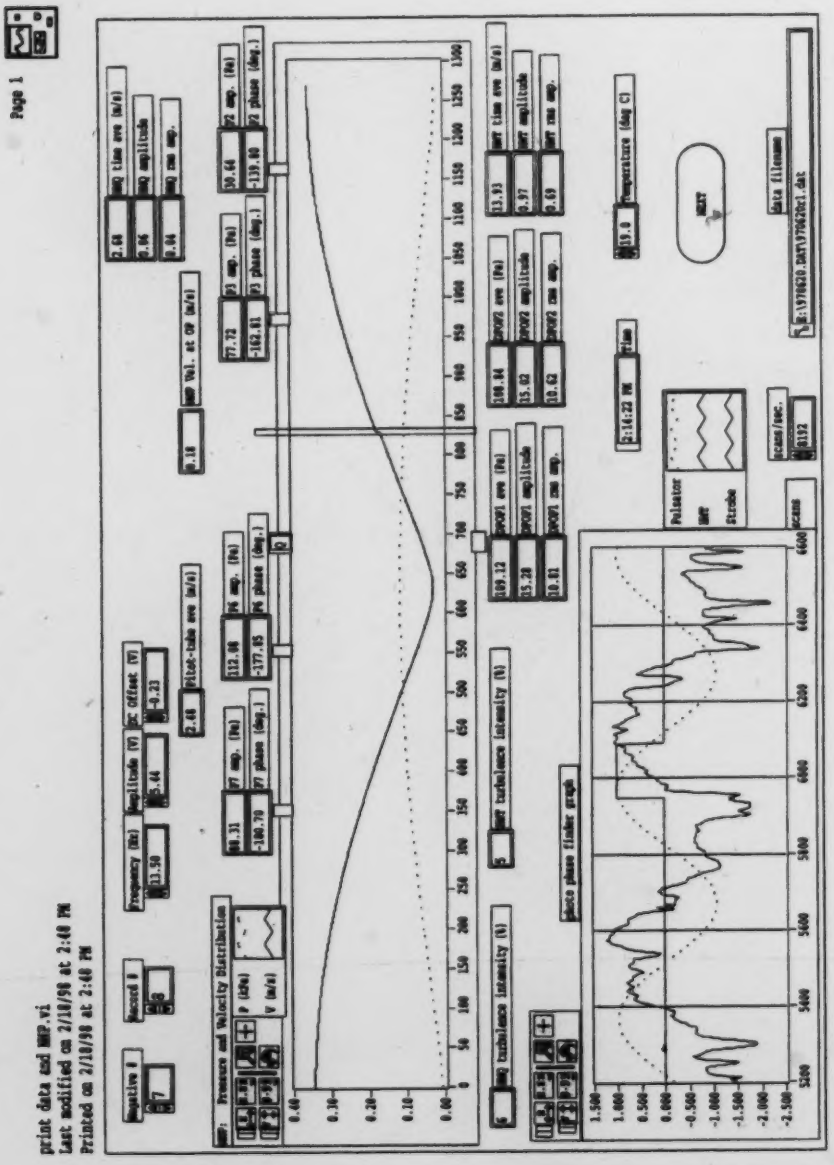
print data and MHP.vi
Last modified on 2/18/98 at 2:40 PM
Printed on 2/18/98 at 2:40 PM
Page 1
MHP: Pressure and Velocity Distribution
Frequency (Hz)
Amplitude (V)
DC Offset (V)
Pitot-tube ave (m/s)
Pitot-tube amp. (m/s)
Pitot-tube phase (deg.)
Port ave (Pa)
Port amplitude
Port rms amp.
Port time ave (m/s)
Temperature (deg C)
Data filename
Pulsator
Strobe
MHT
Port turbulence intensity (%)
Pitot phase finder graph

Figure D.2: 20R1N15

Page 1
print data and MMP.vi
Last modified on 2/18/98 at 3:04 PM
Printed on 2/18/98 at 3:05 PM
Sequence #
15
Record #
17
Frequency (Hz)
997.80
Amplitude (V)
4.50
DC Offset (V)
4.20
Pitot-tube ave (m/s)
2.50
MMP Vel. at CP (m/s)
0.34
MMP Pressure and Velocity Distribution
P (kPa)
V (m/s)
P7 amp. (Pa)
287.26
P7 phase (deg.)
-33.96
P6 amp. (Pa)
88.87
P6 phase (deg.)
-23.76
P5 amp. (Pa)
P5 phase (deg.)
MMP turbulence intensity (%)
MMP turbulence intensity (%)
photo phase fitches graph
P3 amp. (Pa)
211.43
P3 phase (deg.)
-217.52
P2 amp. (Pa)
56.15
P2 phase (deg.)
-159.91
MMP1 ave (Pa)
109.38
MMP1 amplitude
13.47
MMP1 rms amp.
21.67
MMP2 ave (Pa)
109.45
MMP2 amplitude
14.40
MMP2 rms amp.
24.33
MMP time ave (m/s)
13.53
MMP amplitude
1.95
MMP rms amp.
2.38
2:38:31 PM
Time
Temperature (deg C)
Polarizer
MMP
Strobe
MEET
Data filename
D:\971020.DAT\971623b1.dat
Scans/sec.
Scans

Figure D.3: 20R1N21

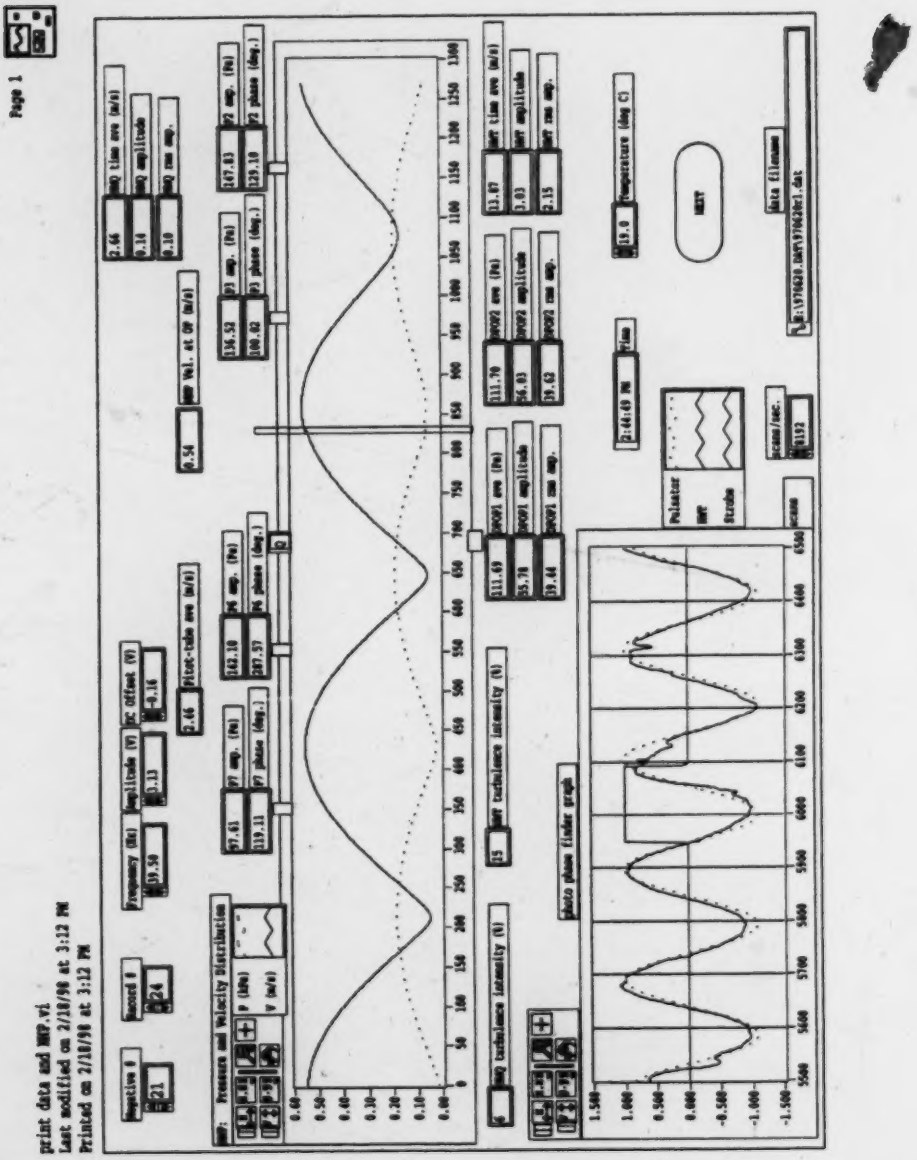
Page 1
print data and MHP.vi
Last modified on 2/18/98 at 3:12 PM
Printed on 2/18/98 at 3:12 PM
MHP: Pressure and Velocity Distribution
Frequency (Hz)
Amplitude (V)
DC offset (V)
Pitot-tube ave (m/s)
MHP Vel. at CP (m/s)
MHP turbulence intensity (%)
Photo phase tickler graph
Polaster
Strobe
MET
Temperature (deg C)
Data filename

Figure D.4: 20R1N22

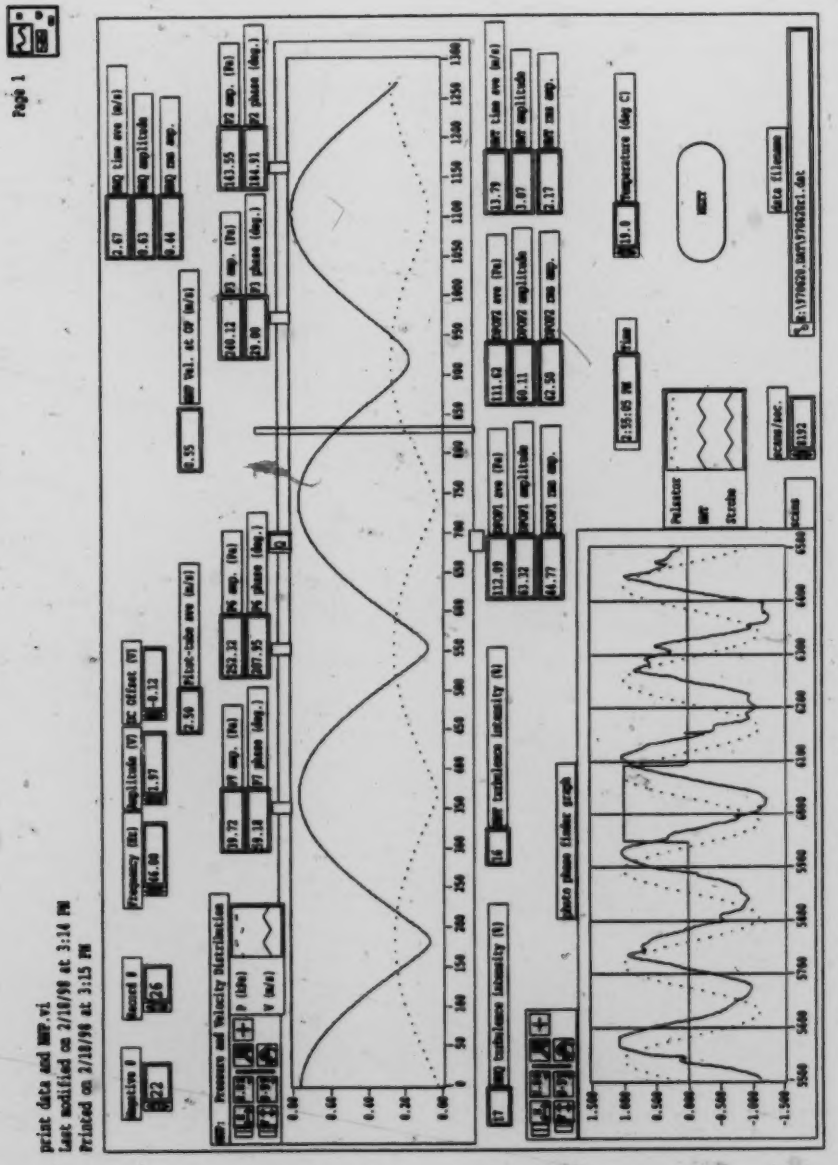
print data and HWP.vi
Last modified on 2/10/98 at 3:14 PM
Printed on 2/10/98 at 3:15 PM
Page 1
Pressure and Velocity Distribution
Frequency (Hz)
Amplitude (V)
DC offset (V)
Phase-time ave (m/s)
Power turbulence intensity (%)
Temperature (deg C)
Data filename

Figure D.5: 20R1N27

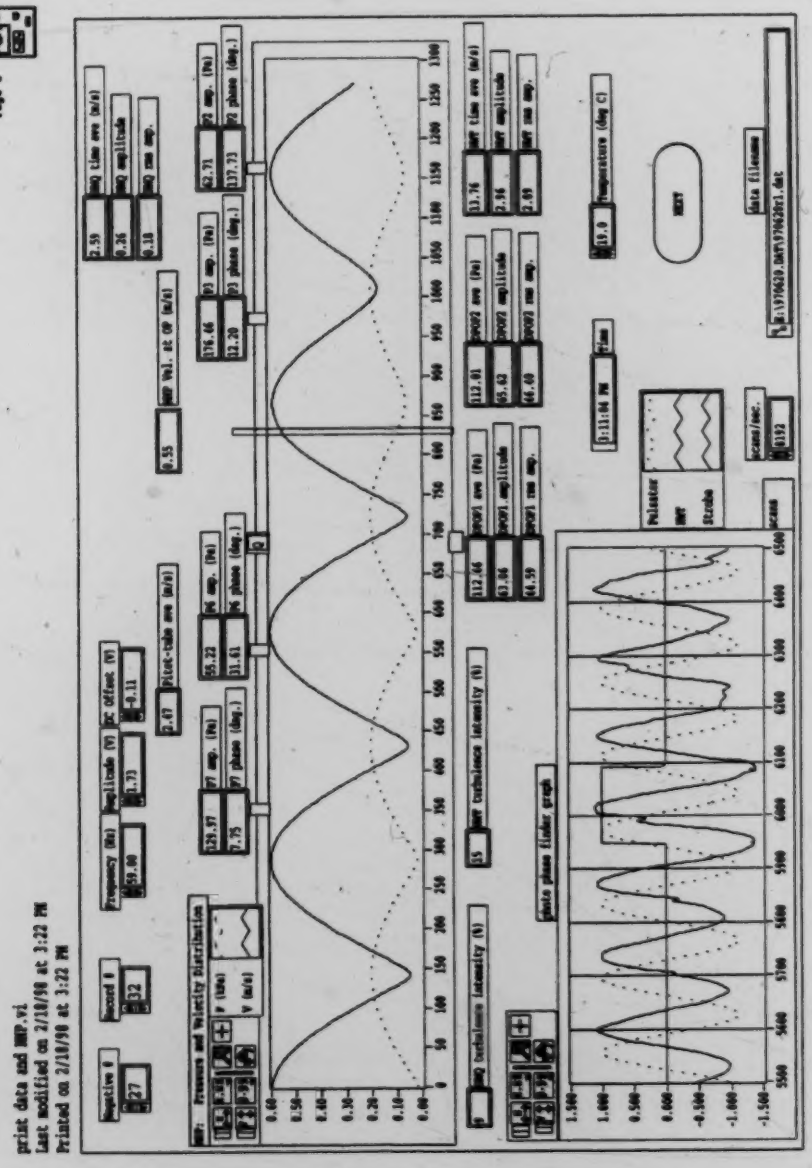
Page 1
print data and MMP.vi
Last modified on 2/10/90 at 3:22 PM
Printed on 2/10/90 at 3:22 PM
MMP: Pressure and Velocity Distribution
Frequency (Hz)
Amplitude (V)
DC Offset (V)
Pitot-tube ave (m/s)
MMP Vel. at CP (m/s)
MMP turbulence intensity (%)
Temperature (deg C)
Polaroid
MMP
Strobe
Data filename

Figure D.6: 20R1N32

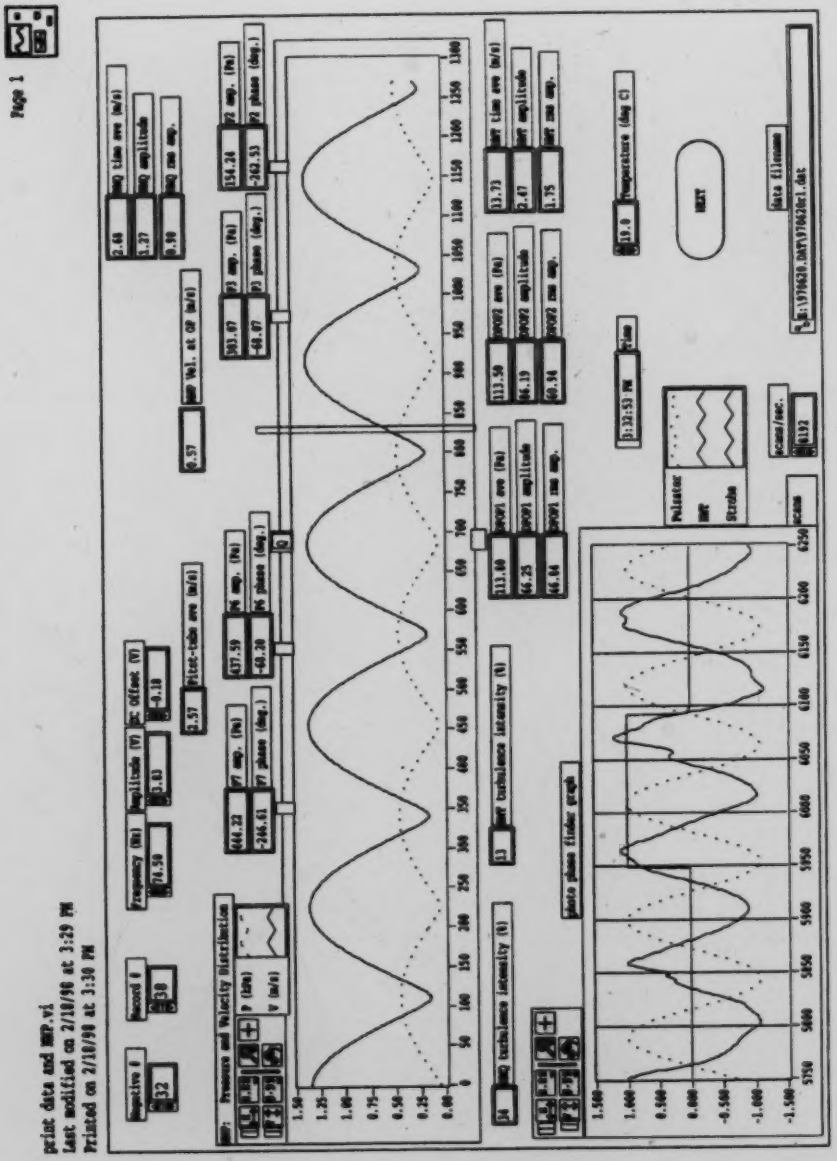
Page 1
print data and HRP.vi
Last modified on 2/10/98 at 3:29 PM
Printed on 2/10/98 at 3:30 PM
Pressure and Velocity Distribution
Frequency (Hz)
Amplitude (V)
DC Offset (V)
Pitot-tube ave (m/s)
P1 amp. (Pa)
P1 phase (deg.)
P2 amp. (Pa)
P2 phase (deg.)
Jet turbulence intensity (%)
Jet Vel. at OP (m/s)
Jet time ave (m/s)
Jet amplitude
Jet rms amp.
Jet turbulence intensity (%)
plate phase finder graph
Pulsator
Jet
Strobe
HEAT
Temperature (deg C)
data filename
C:\DATA\970620.DAT\970620e1.dat

Figure D.7: 20R2N04

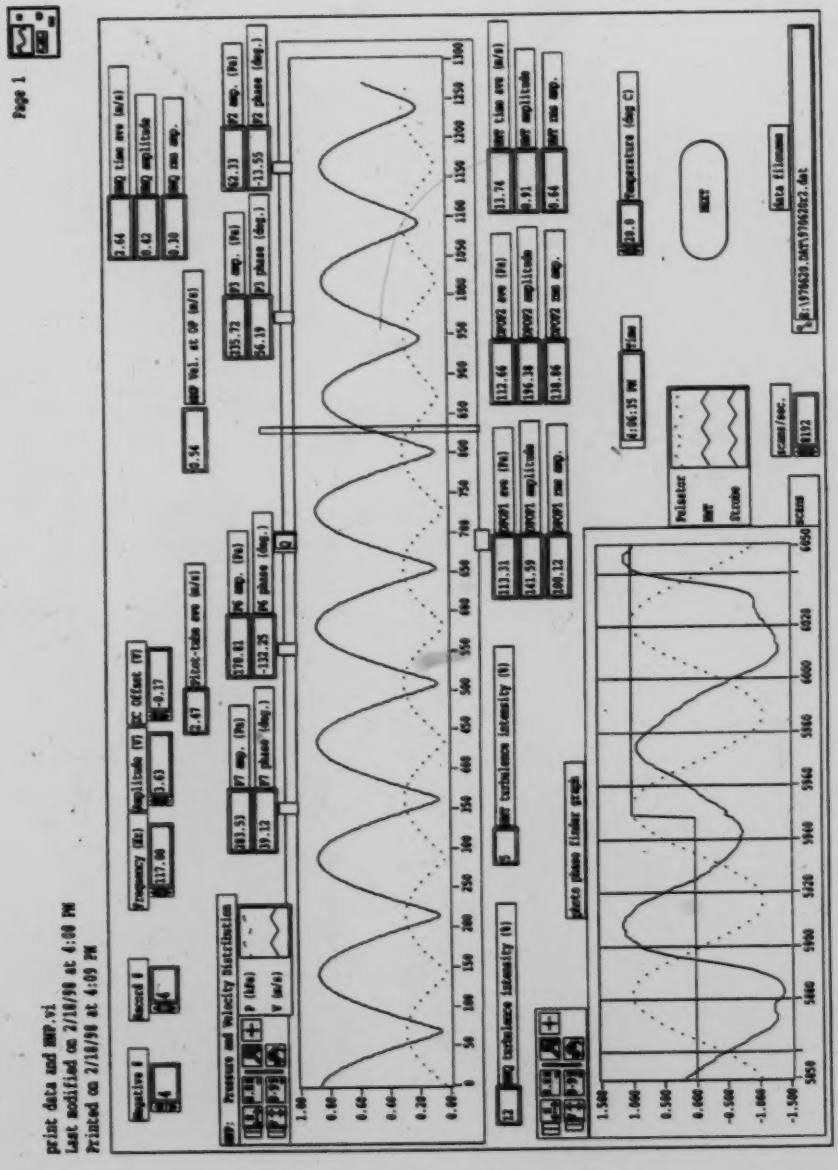
Page 1
print data and HWP.vi
Last modified on 2/10/98 at 4:00 PM
Printed on 2/10/98 at 4:09 PM

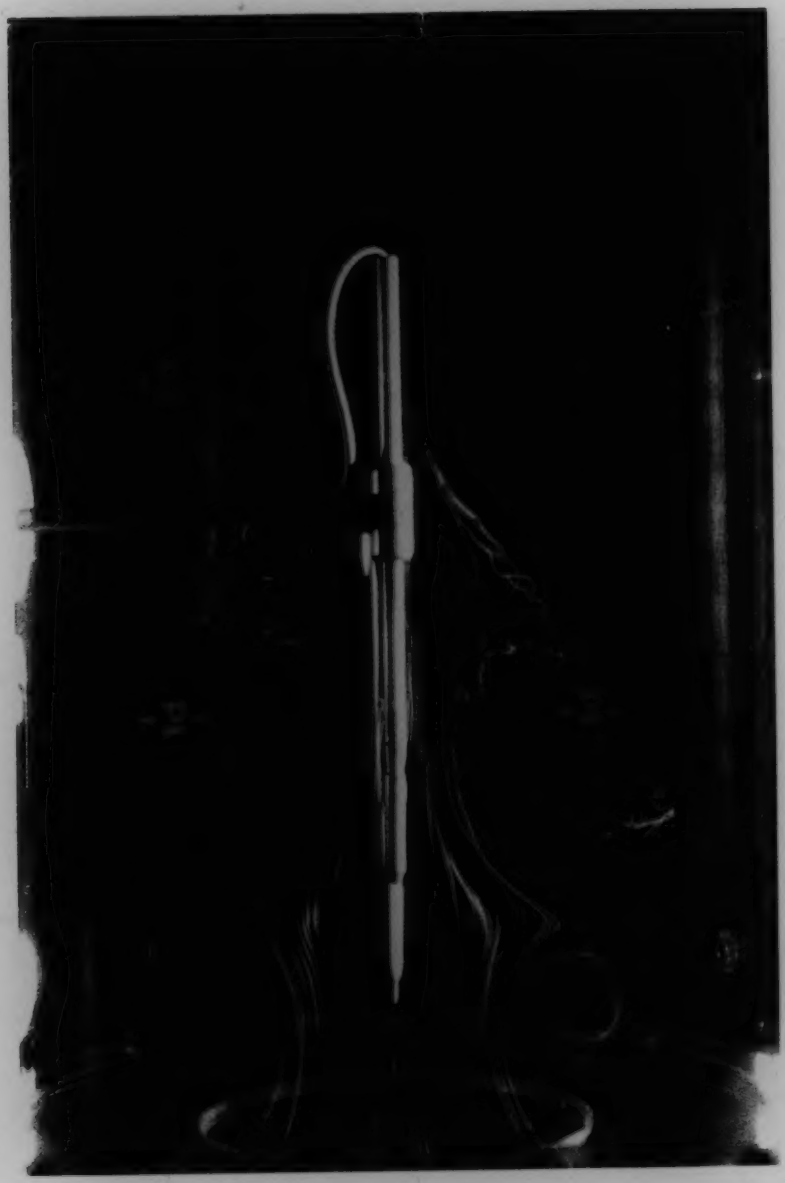

Figure D.8: 20R2N08

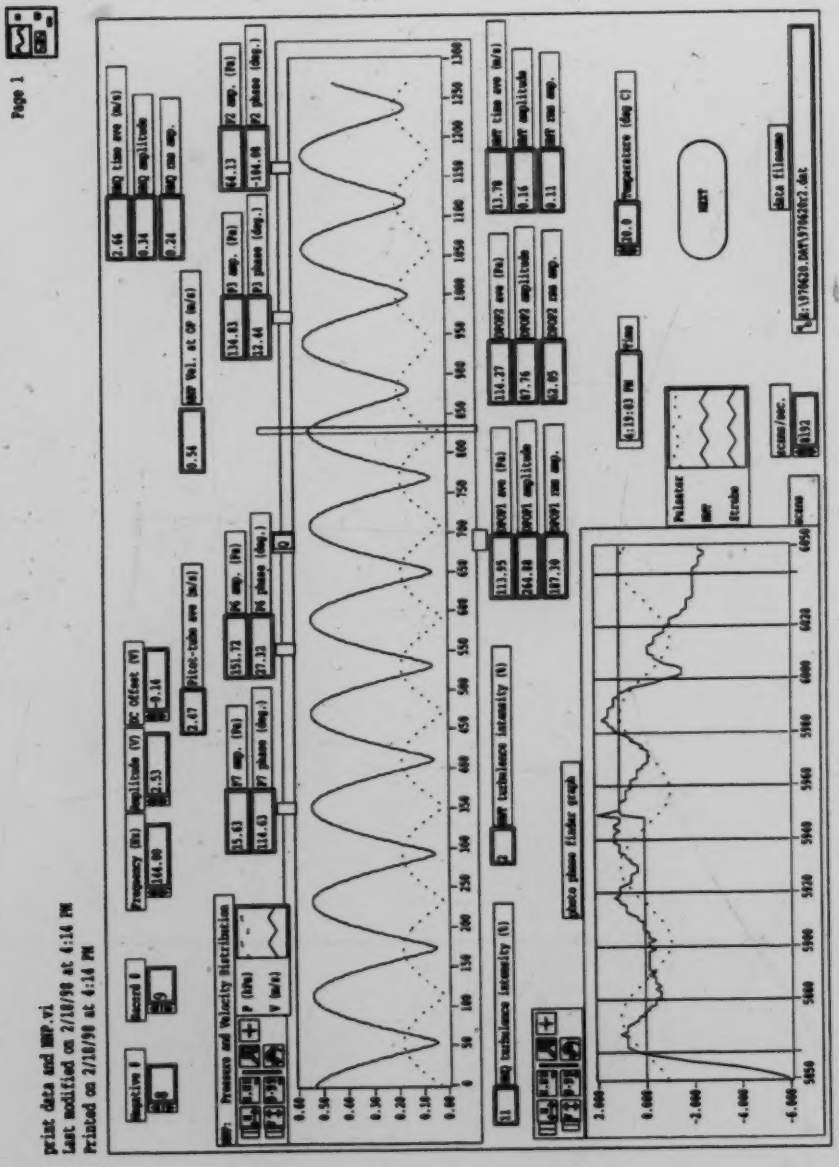
Page 1
print data and MMP.vi
Last modified on 2/10/98 at 4:14 PM
Printed on 2/10/98 at 4:14 PM
Positive #
Record #
Frequency (Hz)
Amplitude (V)
DC offset (V)
Pressure and Velocity Distribution
P (Pa)
V (m/s)
P7 amp. (Pa)
P7 phase (deg.)
Pitot-tube ave (m/s)
P4 amp. (Pa)
P4 phase (deg.)
mean turbulence intensity (%)
photo phase finder graph
mean Vel. at CP (m/s)
P2 amp. (Pa)
P2 phase (deg.)
P3 amp. (Pa)
P3 phase (deg.)
mag time ave (m/s)
mag amplitude
mag rms amp.
power time ave (m/s)
power amplitude
power rms amp.
power2 ave (Pa)
power2 amplitude
power2 rms amp.
4:19:03 PM
Plots
Temperature (deg C)
Palmtop
MMP
Strobe
scans/sec.
scans
data filename
STOP

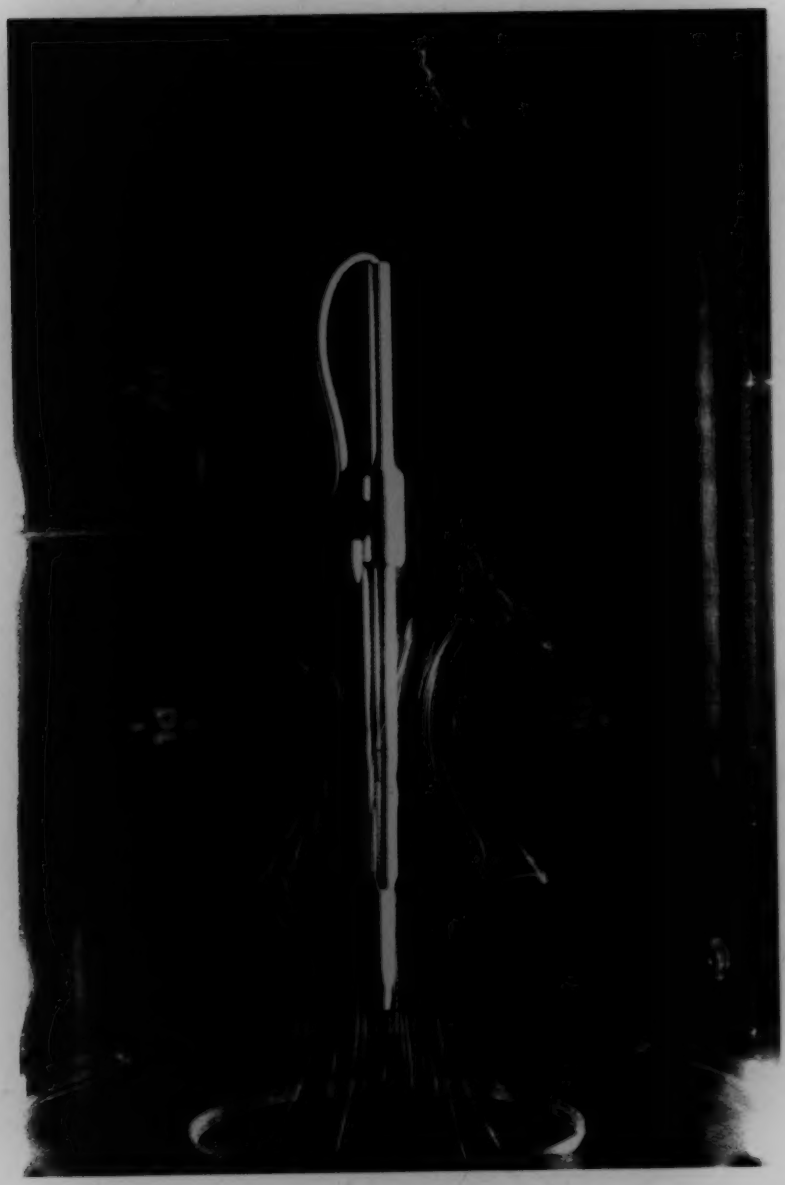

Figure D.9: 20R2N16

print data and MMP.vi
Last modified on 2/18/98 at 4:30 PM
Printed on 2/18/98 at 4:30 PM

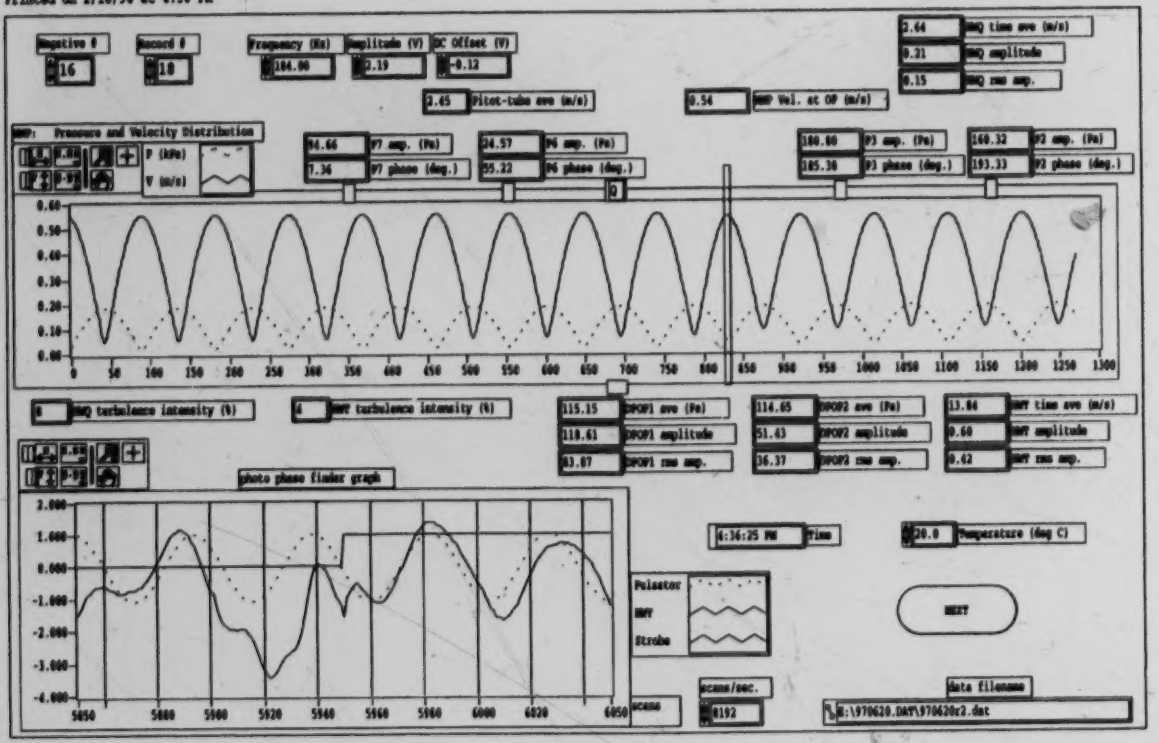

Figure D.10: 20R2N19

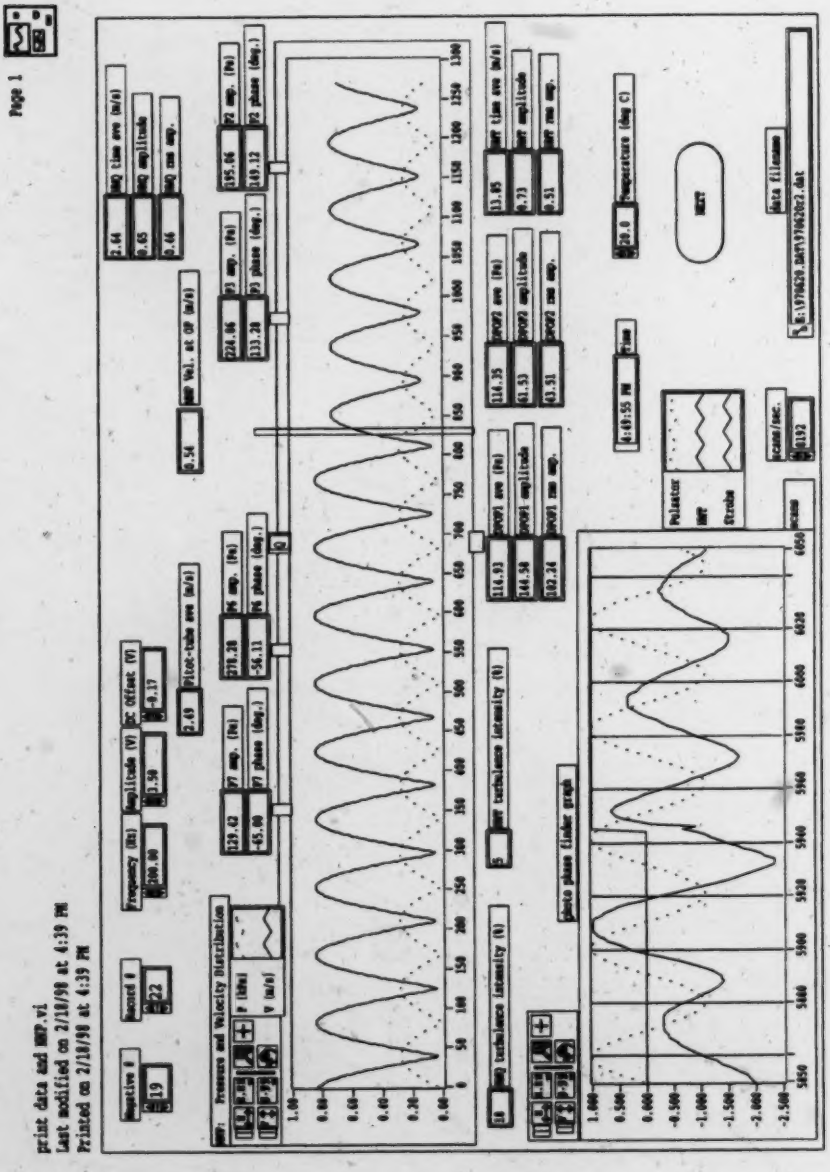
Page 1
print data and MRP.vi
Last modified on 2/10/98 at 4:39 PM
Printed on 2/10/98 at 4:39 PM
Pressure and Velocity Distribution
Frequency (Hz)
Amplitude (V)
DC Offset (V)
Pitot-tube ave (m/s)
Temperature (deg C)
Polaroid
MRP
Strobe
Data filename

Figure D.11: 20R2N25

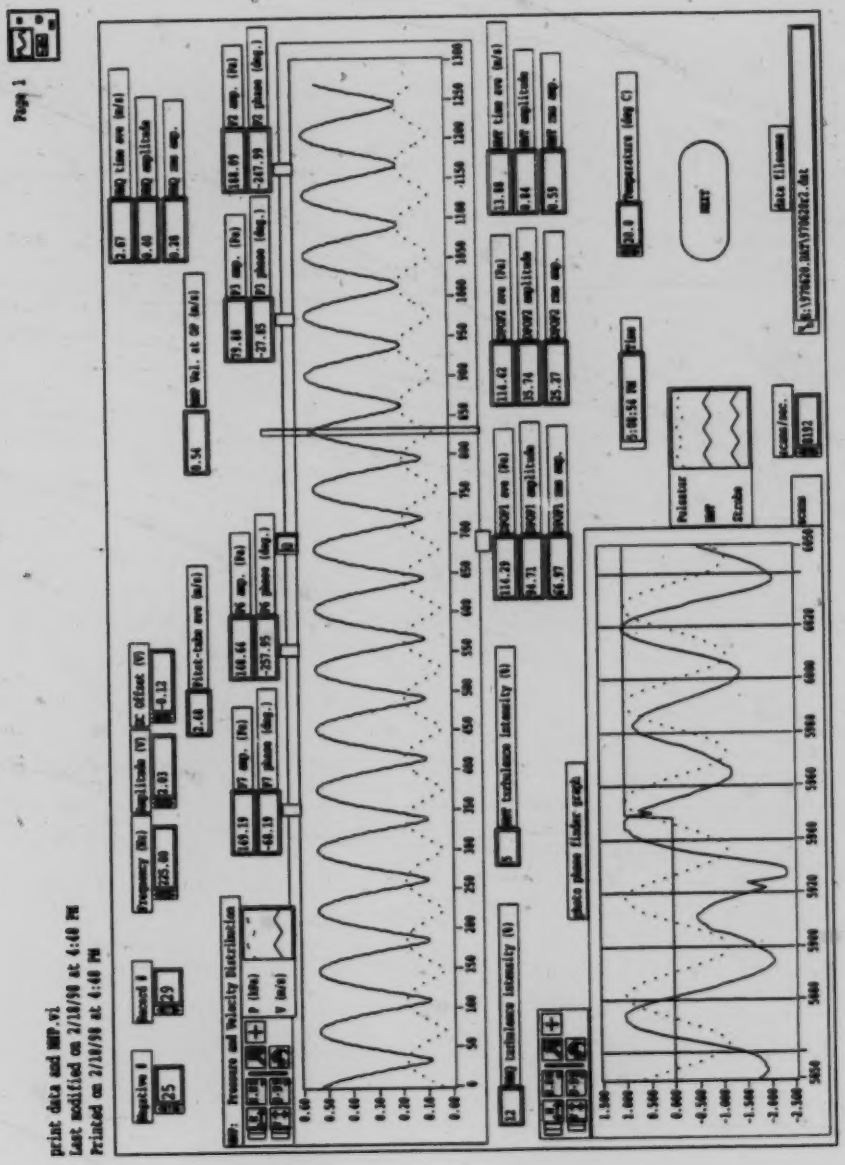
print data and HWP.vi
Last modified on 2/10/98 at 4:40 PM
Printed on 2/10/98 at 4:40 PM
Page 1
Pressure and Velocity Distribution
Power turbulence intensity (%)
Phase plane fisher graph
Temperature (deg C)
Data filename

Figure D.12: 20R2N27

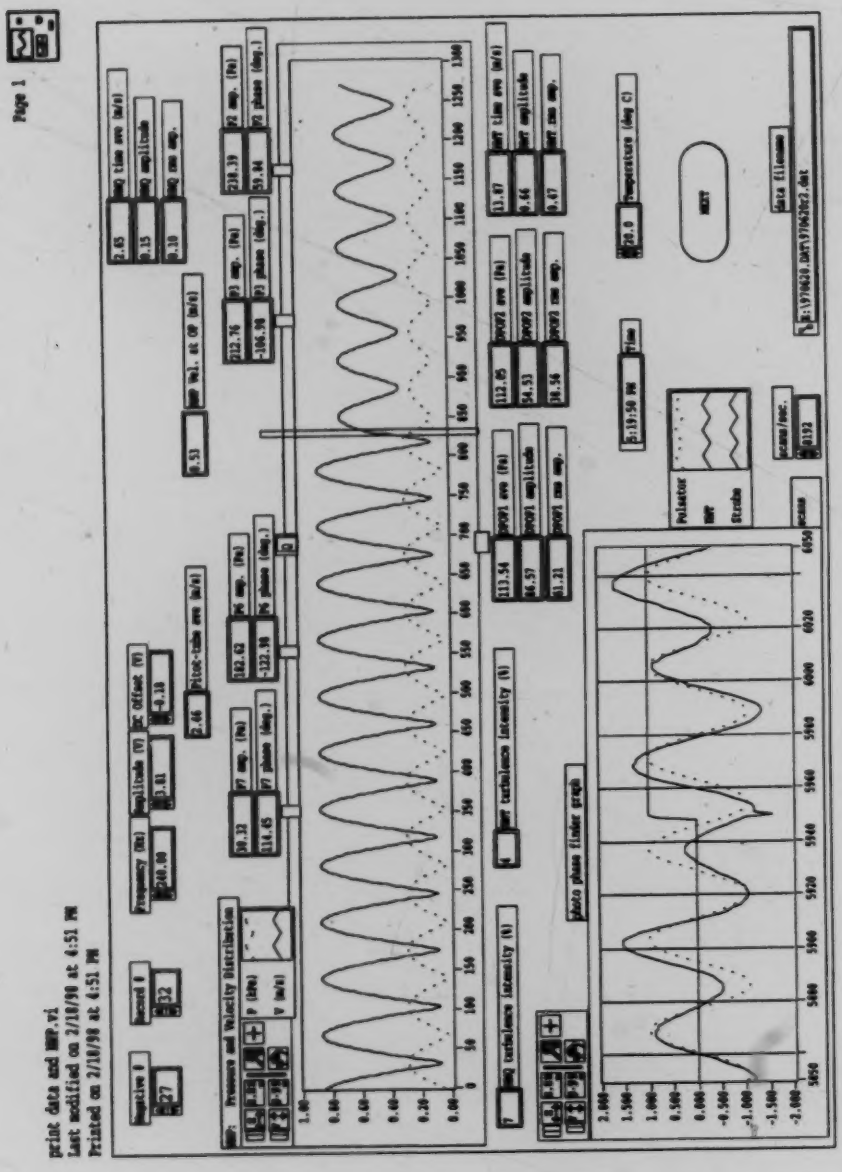
Page 1
print data and MMP.vi
Last modified on 2/10/98 at 4:51 PM
Printed on 2/10/98 at 4:51 PM
MMP: Pressure and Velocity Distribution
Temperature (deg C)
Data filename

Figure D.13: 20R2N35

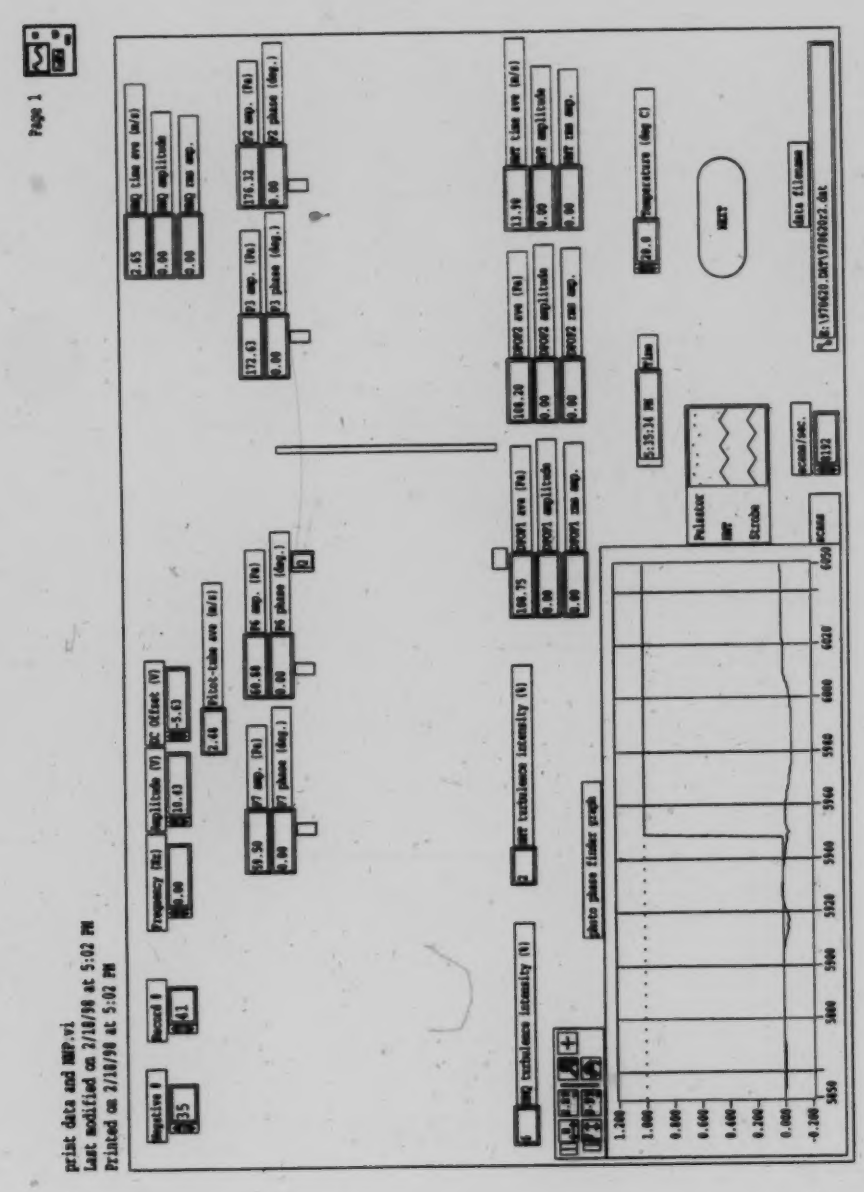
Page 1
print data and MMP.vi
Last modified on 2/18/98 at 5:02 PM
Printed on 2/18/98 at 5:02 PM
Negative #
35
Record #
41
Frequency (Hz)
Amplitude (V)
DC offset (V)
Pitot-tube ave (m/s)
Beam turbulence intensity (%)
Photo phase finder graph
Polarator
Ekrohn
Temperature (deg C)
Data filename

D.3 970624

Table D.3: 970624 Run

Photo #	f_p (Hz)	St_{sh}	St_j	C_D	ΔC_D	$\frac{u'}{6U_{pipe}}$
24R1N04	NoX	0.00	0.00	0.53	0.0%	0.0%
24R1N09	307	1.87	3.73	0.53	-0.2%	1.3%
24R1N14	198.5	1.22	2.44	0.54	0.7%	14.7%
24R1N18	183.5	1.09	2.17	0.41	-23.3%	24.8%
24R1N25	142.5	0.66	1.33	0.40	-25.4%	25.2%
24R1N28	101.5	0.49	0.98	0.37	-30.7%	25.7%
24R2N03	60	0.31	0.61	0.38	-29.8%	25.0%
24R2N08	46.5	0.23	0.46	0.37	-30.3%	24.9%
24R2N11	20	0.11	0.21	0.40	-26.0%	25.0%
24R2N18	16	0.10	0.19	0.52	-2.7%	6.4%
24R2N24	8	0.05	0.10	0.53	-1.7%	3.6%

Re = 9,000 U_{pipe} = 0.94 m/s D = 146.1 mm $\beta = 0.5$

D.4 970703

Table D.4: 970703 Run

Photo #	f_p (Hz)	St_{sh}	St_j	C_D	ΔC_D	$\frac{\overline{u'}}{4U_{pipe}}$	$\frac{\overline{u'}}{HWT}$	$HWT_{nophoto}$
03R1N06	NoX	0.00	0.00	0.58	0.1%	0.0%	0.0%	3.3
03R1N11	307	2.38	8.86	0.58	0.8%	3.3%	3.8%	3.3
03R1N16	198.5	1.68	6.23	0.62	8.0%	15.3%	19.2%	3.0
03R1N19	183.5	1.19	4.43	0.48	-17.2%	37.2%	35.9%	3.9
03R1N23	142.5	0.92	3.43	0.48	-16.3%	36.9%	35.5%	3.9
03R1N32	101.5	0.59	2.18	0.40	-31.2%	37.2%	31.9%	4.4
03R2N06	60	0.34	1.28	0.38	-33.5%	37.0%	31.5%	4.5
03R2N13	46.5	0.26	0.98	0.38	-34.9%	37.1%	31.2%	4.5
03R2N16	20	0.12	0.45	0.38	-34.4%	37.2%	33.7%	4.2
03R2N24	16	0.12	0.46	0.54	-5.5%	9.9%	11.4%	3.3
03R2N28	8	0.06	0.23	0.57	-1.1%	4.6%	5.2%	3.3

Re = 9,000 U_{pipe} = 0.94 m/s D =146.1 mm $\beta = 0.65$